# PROBING ELECTRONIC PROPERTIES OF CARBON NANOTUBES

Thesis by

Jinseong Heo

In Partial Fulfillment of the Requirements for the

degree of

Doctor of Philosophy


CALIFORNIA INSTITUTE OF TECHNOLOGY

Pasadena, California

2008

(Defended MAY 27, 2008)

# ACKNOWLEDGEMENTS

"Doing science is very interesting because we are not always going to get what we are looking for." I remember my advisor, Professor Marc Bockrath saying this uncertainty in scientific experiments when I was an early year graduate student. Since his statement captured my mind, interestingly, I have been always ended up with unexpected phenomena in my experiments. Those excitements led me to the achievement. Also as a great mentor, Marc has been always my role model showing how to approach a scientific problem and tackle it while enjoying the process. For his endless support and encouragement, I would like to thank Marc from my heart.

It would not be possible to finish my thesis work without support from my lab mates, Hsin-Ying Chiu, Vikram Deshpande, Hareem Tariq and Brian Standley. I especially thank for fruitful discussion about fabricating a good sample and for all the encouragement they showed over the years. It is priceless.

I would like to thank Professor Gil Refael for collaboration in our nanotube loop project. His idea of Sagnac type interference due to the velocity mismatch was brilliant and made my work more valuable. I also would like to thank Young Shik Shin and Jihun Kim for helping me fabricating multi-walled nanotube devices with close side gates.

Having good friendship with Caltech Korean graduate students and Sungsam Korean Catholic Church Young Adult Group members was nourishment in my life here. I have been so comfortable and relaxed with them having parties or playing various sports. I am truly grateful for being surrounded by those warmhearted friends who made me

unforgettable memories in retreats, snowboarding trips, fishing trips, and so on. I would like to give many thanks to all of them being so nice to me and I am going to miss you all.

Lastly, I would like to thank my grandmother and mother in heaven who had dedicated their lives to show me what the true love is. I would not be here without their sacrifices. Furthermore, I am so indebted to the rest of my family for what I accomplished. I am really thankful to my father for supporting me financially and mentally throughout the whole education and to my lovely sisters for taking care of me a lot.

# ABSTRACT

Carbon nanotubes are quasi-one-dimensional objects that have many remarkable electronic properties. In Chapter I, an electrostatic force microscopy technique to probe the local density of states of single-walled carbon nanotubes (SWCNTs) under ambient conditions is described. Coupling the atomic force microscope tip motion with the quantum capacitance of nanotubes enables the van Hove singularities in the one-dimensional density of states to be resolved. We utilized this technique to identify individual semiconducting and metallic tubes, and further to estimate the chiral angle of a nanotube. Moreover, in order to realize a SWCNT interferometer, nanotube loop devices where a self-crossing geometry yields two electron paths that is a possible analog of the optical Sagnac interferometer are fabricated and explored in Chapter II. Scanning gate microscopy reveals for semiconducting devices a 0–50% transmission probability into the loop segment at the junction, which can be controlled by applying back gate voltage, hence shifting the Fermi level of the nanotube. Metallic loop devices having low contact resistance showed a large-scale conductance peak with fast oscillations superposed on it. Possible theoretical explanations including Sagnac-type interference, which takes the velocity difference between left and right movers in to account, and Fabry-Perot-type interference are compared with the experimental observations. In Chapter III, in accordance with increasing demand for developing spin-electronic devices, cobalt-filled multi-walled carbon nanotubes (Co–filled MWCNTs) are first synthesized and imaged by transmission electron microscopy, and also characterized by various spectroscopy tools like X–ray diffraction and energy dispersive X–ray spectrometry. Further, a Co–filled MWCNT device having

reproducible switching in magnetoresistance was demonstrated. The last topic, in Chapter IV, covers the effects of a transverse electric field in MWCNT devices, where conductance fluctuations as a function of the transverse electric field were observed. The electric field spacing between the peaks of the fluctuations is in agreement with the theoretical predictions of band structure modulation by transverse electric fields. We also measured the magnetoconductance when a magnetic field is perpendicular to the tube axis, and observed conductance fluctuations. These fluctuations are well explained in terms of weak localization and universal conductance fluctuations. Future work following our experimental studies is proposed and discussed at the end of each chapter.

# TABLE OF CONTENTS

# LIST OF FIGURES

## Chapter I

**Chapter II**

**Chapter III**



**Chapter IV**

*C h a p t e r  I*

# LOCAL ELECTRONIC STRUCTURE OF SINGLE-WALLED CARBON NANOTUBES FROM ELECTROSTATIC FORCE MICROSCOPY[1]

## I.1 Abstract

We show that a simple yet powerful technique based on electrostatic force microscopy (EFM), which measures the electrostatic forces between a sharp tip and single-walled nanotube (SWNT), can probe the compressibility of the electron gas in nanotubes under ambient conditions at room temperature. Populating additional subbands corresponding to excited states of circumferential motion leads the abrupt increase of the tip-tube capacitance and enables the one dimensional (1D) van Hove singularities in the density of states to be resolved. This demonstrates the effects of quantum confinement on a nanotube's capacitance, which has implications for the high-frequency operation of nanotube devices. Additionally, we obtain spectroscopic information about the local density of states with nanometer-scale resolution. We have exploited this capability to measure the local band gap of an intratube quantum-well structure, created by the application of a non-uniform uniaxial strain. From the local band gap versus the local strain, we infer the nanotube chiral angle by comparison to theoretical models. The technique is applicable for investigating the properties of other nano-scaled systems.

## I-2 Introduction

In this introduction, I would like to derive the most commonly used electronic band structure of 1D carbon nanotubes using a tight binding calculation[2-4]. As a nanotube can be conceptualized as being rolled up from two dimensional (2D) graphene sheet, it is natural to derive the energy bands of 2D graphene first.

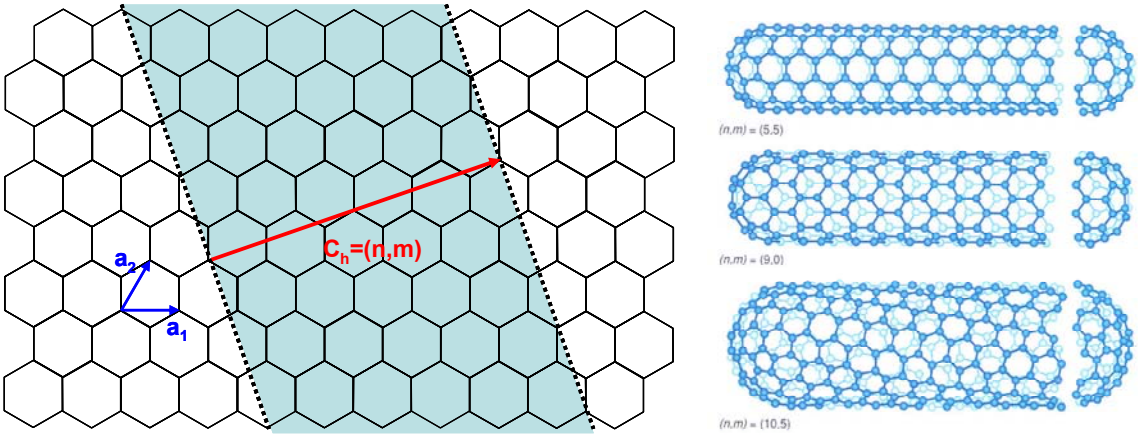


Figure I-1. Graphene and nanotubes. A graphene sheet is shown on the left with a hexagonal lattice of carbon. Nanotubes are essentially a graphene sheet rolled up. For example, the blue shaded region is cut out and rolled up such that dashed lines coincide. This specific choice gives a (4, 2) tube (an ($n$, $m$) tube is defined by a chiral vector, $\mathbf{C}_h = n\mathbf{a}_1 + m\mathbf{a}_2 \equiv (n, m)$, ($n$, $m$ are integers, $0 \le m \le n$)). Various types (so-called armchair, zigzag, and chiral from the top) of tubes are shown on the right.

### I-2-1 Tight-Binding Calculation

A tight binding calculation is valid when the overlap of atomic wave functions is large enough to require corrections to the picture of isolated atoms, but not so large as to render the atomic description completely irrelevant.

The Schroedinger equation for an isolated atom is given by

$$H_{atom}\psi_i = E_i\psi_i \qquad \text{(I.1)}$$

where $H_{atom}$ is the atomic Hamiltonian for each isolated atom, $E_i$ is the energy, and $\psi_i$ is the wave function. Note that $H_{atom}$ becomes substantially different from the full crystal Hamiltonian $H$ at a distance of the order of the lattice constant and also, $\psi_i$ is very small outside of the range. Then, the full crystal Schroedinger equation is

$$H\psi(\mathbf{r}) = (H_{atom} + \Delta U(\mathbf{r}))\psi(\mathbf{r}) = E\psi(\mathbf{r}) \qquad \text{(I.2)}$$

where $\Delta U$ is correction to the atomic potential and $\psi$ is the crystal wave function. Since we are considering a Bravais lattice, which has translational symmetry by any combination of lattice vectors, we can seek a solution satisfying Bloch's theorem,

$$\psi(\mathbf{r}) = \sum_{\mathbf{R}} e^{i\mathbf{k}\cdot\mathbf{R}}\phi(\mathbf{r}-\mathbf{R}) \qquad \text{(I.3)}$$

where $\Psi(\mathbf{r})$ is a linear combination of atomic wave functions,

$$\phi(\mathbf{r}) = \sum_n b_n\psi_n(\mathbf{r}). \qquad \text{(I.4)}$$

That is, if the product $\Delta U(\mathbf{r})\psi_n(\mathbf{r})$, though non-zero, is sufficiently small, $\Psi(\mathbf{r})$ is just the linear combination of sublattice atomic wave functions, $\psi_n(\mathbf{r})$.

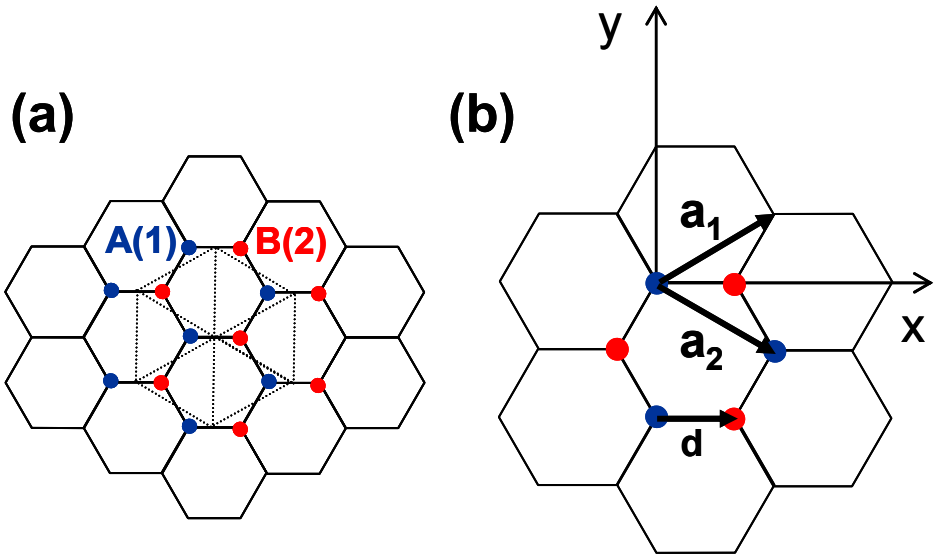


Figure I-2. Bravais lattice in graphene. (a) Two sublattices (A, B) on a graphene each make a hexagonal Bravais lattice (dotted lines). (b) Two primitive vectors $\mathbf{a}_1 = \left(\frac{\sqrt{3}}{2}a, \frac{a}{2}\right)$, $\mathbf{a}_2 = \left(\frac{\sqrt{3}}{2}a, -\frac{a}{2}\right)$, carbon-carbon distance **d**

### I-2-2 Energy Band Structure of Graphene from Tight-Binding Calculation

Each carbon atom has four valence electrons. In graphene, three of them are covalently bonded to the three nearest carbon atoms ($sp^2$ hybridization) and the other one in $2p_z$ participates in electron conduction. So, the problem discussed here is limited to one itinerant electron in each carbon atom site of hexagonal lattice. But, because of the considerable overlap of atomic wave functions originating from each site, the $2p_z$ electrons are delocalized over the whole sheet. The electronic band structure of graphene is then obtained below from a tight-binding calculation.

The Bravais lattice of graphene has two atoms per unit cell, yielding the two sublattices A and B (Figure I-2). The primitive vectors are expressed as

$$\mathbf{a}_1 = \left(\frac{\sqrt{3}}{2}\mathrm{a},\ \frac{\mathrm{a}}{2}\right),\ \mathbf{a}_2 = \left(\frac{\sqrt{3}}{2}\mathrm{a},\ -\frac{\mathrm{a}}{2}\right) \qquad \text{(I.5)}$$

where $\mathrm{a} = |\mathbf{a}_1| = |\mathbf{a}_2| = \mathrm{a_{c\text{-}c}} \times \sqrt{3} = 2.46$ Å. Then, Equation I.4 can be written as

$$\phi(\mathbf{r}) = b_1\psi_1(\mathbf{r}) + b_2\psi_2(\mathbf{r}-\mathbf{d}) \qquad \text{(I.6)}$$

where 1 and 2 correspond to A and B sites, respectively, and **d** is carbon-carbon distance, $\mathbf{d}=a_{\mathrm{c\text{-}c}}=1.42$ Å. Equation I.3 becomes

$$\psi(\mathbf{r}) = \sum_{\mathbf{R}} e^{i\mathbf{k}\cdot\mathbf{R}}\left(b_1\psi_1(\mathbf{r}-\mathbf{R}) + b_2\psi_2(\mathbf{r}-\mathbf{R}-\mathbf{d})\right). \qquad \text{(I.7)}$$

By multiplying $\psi_{1,2}(\mathbf{r})$ on both sides of Equation I.2 and integrating over **r**,

$$(E_{1,2}-E)\int \psi_{1,2}^{*}(\mathbf{r})\psi(\mathbf{r})\,d\mathbf{r} + \int \psi_{1,2}^{*}(\mathbf{r})\Delta U(\mathbf{r})\psi(\mathbf{r})\,d\mathbf{r} = 0. \qquad \text{(I.8)}$$

Choosing $E_{1,2}= 0$ and only considering the nearest neighbors (three B atoms around A and vice versa), we get by substituting Equation I.7 into I.8

$$\begin{aligned} -E(\mathbf{k})\,b_1 - E(\mathbf{k})\,b_2\sum_{\mathrm{i}}\xi_i s_i + b_2\sum_{\mathrm{i}}\xi_i t_i = 0, \\ -E(\mathbf{k})\,b_2 - E(\mathbf{k})\,b_1\sum_{\mathrm{i}}\xi_i s_i + b_1\sum_{\mathrm{i}}\xi_i t_i = 0 \end{aligned} \qquad \text{(I.9)}$$

where $\xi_i(\mathbf{k}) = e^{i\mathbf{k}\cdot\mathbf{R}_i}$ is the phase factor through the three nearest neighbors $\mathbf{R}_i$, i=1, 2, and 3, $s_i = \int \psi^*_{1,2}(\mathbf{r})\, \psi_{2,1}(\mathbf{r}-\mathbf{R}_i)\, \mathrm{d}\mathbf{r}$ is the overlap integral, and

$t_i = \int \psi^*_{1,2}(\mathbf{r})\, \Delta U(\mathbf{r}) \psi_{2,1}(\mathbf{r}-\mathbf{R}_i)\, \mathrm{d}\mathbf{r}$ is the transfer integral. In order to have non-zero solutions for $b_{1,2}$, the determinant has to be zero,

$$\begin{vmatrix} -E & -Es\xi + t\xi \\ -Es\xi + t\xi & -E \end{vmatrix} = 0 \qquad \text{(I.10)}$$

assuming $s = s_1 = s_2 = s_3$, $t = t_1 = t_2 = t_3$ (because of symmetry), and $\xi = \sum \xi_i(\mathbf{k})$.

Equation I.10 gives the energy dispersion relation,

$$E(\mathbf{k}) = \frac{\pm\, t\,\xi(\mathbf{k})}{1 \pm s\,\xi(\mathbf{k})}. \qquad \text{(I.11)}$$

Using the coordinates shown in Figure I-2, and parameters, $t = -3.033\,\mathrm{eV} \approx -3\,\mathrm{eV}$, $s = 0.129 << 1$,

$$E_{2D}(k_x, k_y) = \mp 3\left\{ 1 + 4\cos\left(\frac{\sqrt{3}k_x a}{2}\right)\cos\left(\frac{k_y a}{2}\right) + 4\cos^2\left(\frac{k_y a}{2}\right)\right\}^{\frac{1}{2}} (\mathrm{eV}). \qquad \text{(I.12)}$$

A plot of $E$ has a number of interesting features (Figure I-3). First, it has two distinct bands. The upper band, called anti-bonding $\pi^*$, has higher energy. Using $E(\mathbf{k}) = -t\,\xi(\mathbf{k})$ ($s \approx 0$) from Equation I.11 and Equation I.9, $b_1 \approx -b_2$. That is, two wavefunctions in the basis are out of phase, which gives rise to higher energy state. On the other hand, when

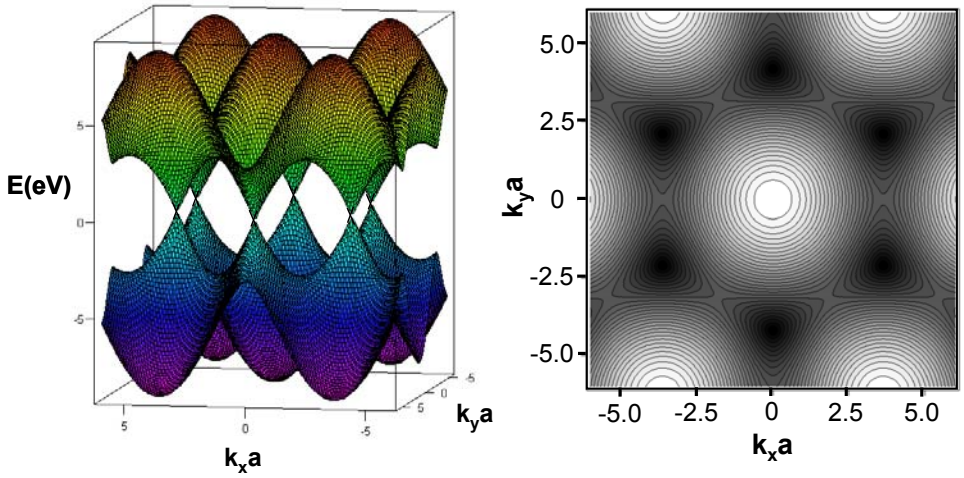


Figure I-3. Graphene band structure. Left image shows 3D plot of energy dispersion. There are six **K** points where upper band (anti-bonding $\pi^*$ band) and lower band (bonding $\pi$ band) meet. Contour plot of one band is shown on the right. **K** points appear dark.

$E(\mathbf{k}) = t\,\xi(\mathbf{k})$, $b_1 \approx b_2$. The wavefunctions are in phase, which gives lower bonding $\pi$ band. Second, there are six points (**K** points) where two bands meet within first Brillouin zone. The 2D graphene energy band is not discontinuous, but rather, the valence band (bonding) and the conduction band (anti-bonding) are connected at the points. That is why graphene is called a semi-metal or zero-bandgap semiconductor. Also those six **K** points occur at the six corners of the first Brillouin zone of the reciprocal lattice (Figure I-4). Reciprocal lattice vectors are given by

$$\mathbf{b}_1 = \left(\frac{2\pi}{\sqrt{3}a}, \frac{2\pi}{a}\right), \mathbf{b}_2 = \left(\frac{2\pi}{\sqrt{3}a}, -\frac{2\pi}{a}\right). \quad \text{(I.13)}$$

The direction of the unit vectors $\mathbf{b}_1$ and $\mathbf{b}_2$ of the reciprocal hexagonal lattice are rotated by 90º from the unit vectors $\mathbf{a}_1$ and $\mathbf{a}_2$ of the hexagonal lattice in real space. By convention, the three high symmetry points, **Γ**, **K,** and **M** as the center, the corner, and the center of the edge, respectively, are defined (Figure I-4).

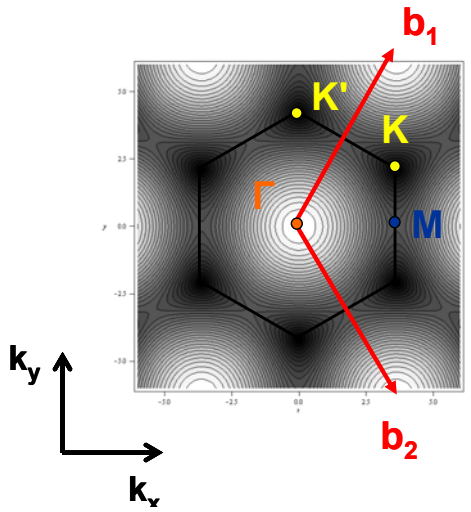


Figure I-4. First Brillouin zone of graphene with contours of energy band

Among six **K** points, there are only two inequivalent points (**K**, **K'** points in Figure I-4). The other four only differ by the addition of reciprocal vectors, $\mathbf{b}_1$ and $\mathbf{b}_2$, to **K** or **K'**. This is an expected result from having two atoms in a basis.

### I-2-3 Energy Band Structure of Carbon Nanotubes

At this point, before deriving the energy dispersion of nanotubes, it is necessary to examine the atomic structure of nanotubes. As shown in Figure I-5, any nanotube can be represented by a chiral vector,

$$\mathbf{C}_h = n\mathbf{a}_1 + m\mathbf{a}_2 \equiv (n,\, m)\,,\ (n,\, m \text{ are integers},\ 0 \le m \le n). \qquad \text{(I.14)}$$

$n$, $m$ indices with a given range in Equation I.14, uniquely define a nanotube. One can also use a different representation of a nanotube with its diameter, $d = |\mathbf{C}_h|$ and the angle $\theta$ specified in Figure I.4. After simple arithmetic,

$$\begin{aligned} d &= a\sqrt{n^2 + m^2 + nm}\,/\,\pi \\ \cos\theta &= \frac{2n+m}{2\sqrt{n^2+m^2+nm}},\ (0^\circ \le \theta \le 30^\circ). \end{aligned} \qquad \text{(I.15)}$$

The given range of $\theta$ is due to the 6-fold symmetry of graphene.

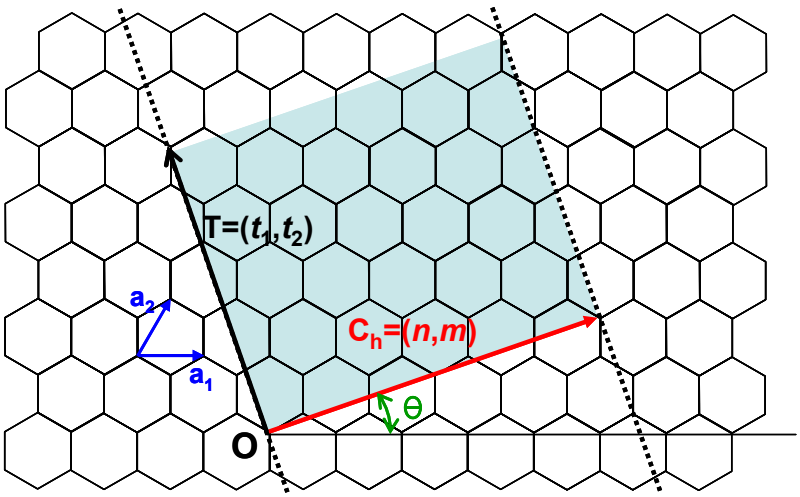


Figure I-5. Making a nanotube and its structure

When $\theta = 0^\circ$, armchair tubes are made, while $\theta = 30^\circ$ corresponds to zigzag tubes. To define the unit cell of a 1D carbon nanotube, it is necessary to get a translation vector, **T** shown in Figure I-5. The translation vector **T**, along the nanotube axis corresponds to the first lattice

point of the 2D graphene sheet from the origin **O** through the dashed line. By considering $\mathbf{C}_h \cdot \mathbf{T} = 0$ and using the inner product between $\mathbf{a}_1$ and $\mathbf{a}_2$,

$$\mathbf{a}_1 \cdot \mathbf{a}_1 = \mathbf{a}_2 \cdot \mathbf{a}_2 = a^2, \quad \mathbf{a}_1 \cdot \mathbf{a}_2 = \frac{a^2}{2}, \quad a = 2.49\ \text{Å} \qquad \text{(I.16)}$$

the expression for translation vector is thus obtained,

$$\begin{aligned} &\mathbf{T} = t_1 \mathbf{a}_1 + t_2 \mathbf{a}_2 \equiv (t_1, t_2), \quad (t_1, t_2 \text{ are integers}) \\ &t_1 = \frac{2m+n}{g}, \quad t_2 = -\frac{2n+m}{g} \end{aligned} \qquad \text{(I.17)}$$

where $g$ is the greatest common divisor of ($2m$+$n$) and ($2n$+$m$). From the specific vector shown in Figure I-5, $\mathbf{C}_h$ = (4, 2) and **T** = (4, -5). Now, the unit cell of a nanotube can be defined by two vectors, $\mathbf{C}_h$ and **T** (blue shaded area in Figure I-5). Then the number of hexagons in the nanotube unit cell, $N$ is just the division of nanotube unit cell area by graphenes,

$$N = \frac{\left|\mathbf{C}_h \times \mathbf{T}\right|}{\left|\mathbf{a}_1 \times \mathbf{a}_2\right|} = \frac{2\left(m^2 + n^2 + nm\right)}{g}. \qquad \text{(I.18)}$$

There are $2N$ numbers of carbon atoms in the nanotube unit cell. In turn, that gives $2N$- 1-D energy dispersion relations. Like $\mathbf{b}_1$ and $\mathbf{b}_2$ in graphene (Equation I-13), expressions for reciprocal vectors $\mathbf{B}_1$ and $\mathbf{B}_2$ in nanotubes, can be obtained. Using

$$\begin{aligned} &\mathbf{C}_h \cdot \mathbf{B_1} = 2\pi, \quad \mathbf{T} \cdot \mathbf{B_1} = 0, \\ &\mathbf{C}_h \cdot \mathbf{B_2} = 0, \quad \mathbf{T} \cdot \mathbf{B_2} = 2\pi, \end{aligned} \qquad \text{(I.19)}$$

we get

$$\mathbf{B}_1 = \frac{1}{N}\left(-t_2\,\mathbf{b}_1 + t_1\,\mathbf{b}_2\right), \quad \mathbf{B}_2 = \frac{1}{N}\left(m\,\mathbf{b}_1 - n\,\mathbf{b}_2\right). \quad \text{(I.20)}$$

Unlike an extended graphene sheet, a nanotube has a few nanometer diameter, and the wavevector associated with the circumferential direction is quantized (Figure I-6). In other words, the wavefunction has to be the same when **r** goes around the circumference.

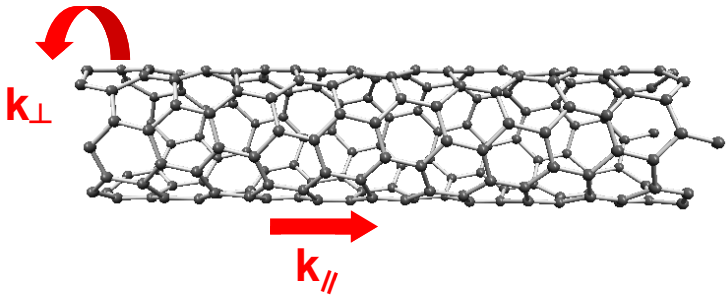


Figure I-6. Quantization of circumferential wavevectors, $\mathbf{k}_\perp$ of nanotubes

In that case, $e^{i\mathbf{k}\cdot\mathbf{C}_h} = e^{i\mathbf{k}\cdot\mathbf{0}} = 1$, which gives $\mathbf{k} \cdot \mathbf{C}_h = 2\pi l$ ($l$ is integer). Using Equation I.19 and I.20, we immediately know there are $N$ discrete $\mathbf{k}_\perp$ vectors, $l\mathbf{B}_1$ ($0 \le l \le N-1$). Because $t_1$ and $t_2$ do not have common divisor, any among the $N$ vectors is not a multiple of any others. Because of the relatively long nanotube length (~ a few μm), the wavevectors along nanotube axis, $\mathbf{k}_{//}$ are rather continuous (although they can be readily resolved in low-temperature transport measurements).

From Equation I.12, the energy dispersion for nanotubes with the restriction of quantized wavevectors is obtained as

$$E_l(k) = E_{2D}\left( k\frac{\mathbf{B}_2}{|\mathbf{B}_2|} + l\,\mathbf{B}_1 \right), \quad (l = 0,\ldots,N-1, \text{ and } -\frac{\pi}{T} \le k \le \frac{\pi}{T}). \qquad \text{(I.21)}$$

So, there are $2N$ subbands (including ±sign) for each nanotube, and the magnitude of wavevectors along the nanotube axis, $k$ is in the range of the first Brillouin zone. Another way of looking at it is cutting 2D energy dispersion (Figure I-3) by equally spaced (by $\mathbf{B}_1$) planes perpendicular to $\mathbf{B}_2$ vector. A cross-section view is shown in Figure I-7(a). Black parallel lines are allowed vectors, which are quantized along the other direction, $\mathbf{B}_1$ and equally spaced by $|\mathbf{B}_1|$. In Figure I-7(b), **Y** point is drawn by perpendicularly intersecting the $\mathbf{B}_2$ vector (running through **Γ** point) from **K** point. Then, $\overrightarrow{\mathbf{YK}}$ vector is given by

$$\overrightarrow{\mathbf{YK}} = \frac{\left(\overrightarrow{\mathbf{\Gamma K}} \cdot \mathbf{B}_1\right)}{|\mathbf{B}_1|^2}\mathbf{B}_1 \qquad \text{(I.22)}$$

where $\overrightarrow{\mathbf{\Gamma K}} = \overrightarrow{\mathbf{\Gamma M}} + \overrightarrow{\mathbf{MK}} = \frac{\mathbf{b}_1 + \mathbf{b}_2}{2} + \frac{\mathbf{b}_1 - \mathbf{b}_2}{6} = \frac{2}{3}\mathbf{b}_1 + \frac{1}{3}\mathbf{b}_2$. Calculating vector product and simplifying the expression, we get

$$\overrightarrow{\mathbf{YK}} = \frac{2n+m}{3}\mathbf{B}_1. \qquad \text{(I.23)}$$

Similarly,

$$\overrightarrow{\mathbf{Y'K''}} = -\frac{2n+m}{3}\mathbf{B}_1 \qquad \text{(I.24)}$$

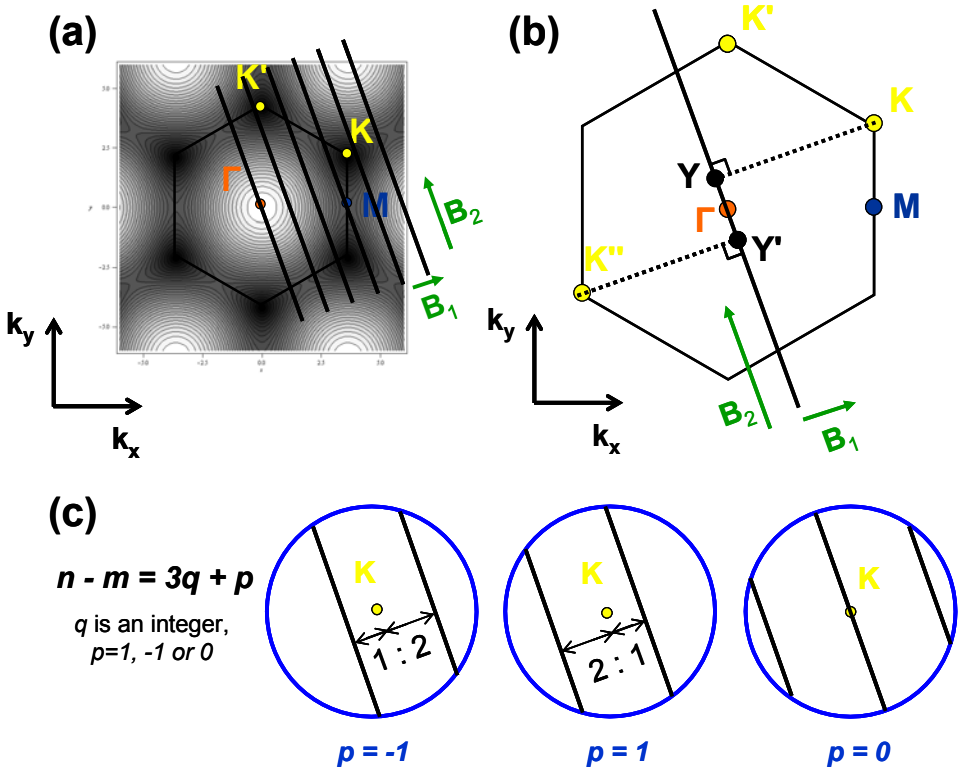


Figure I-7. Allowed wavevectors of a nanotube intersecting in the graphene Brillouin zone. (a) Allowed wavevectors (black parallel lines) intersecting graphene Brillouin zone. Those vectors are quantized along $\mathbf{B}_1$ direction and equally spaced by $|\mathbf{B}_1|$. (b) **Y**(**Y'**) point is drawn by perpendicularly intersecting the $\mathbf{B}_2$ vector (running through **Γ** point) from **K**(**K''**) point. (c) Zoomed-in image around **K** point shows all three cases where quantized vectors can dissect **K** point by 1:2 ratio or running through it. All nanotubes can be classified as one of three cases by p values 1, -1, or 0.

where **K''** is equivalent to **K'** or translated by a reciprocal vector of graphene, $-\mathbf{b}_1$ (Figure I-4).

Remembering that the **K** (**K'**) points are where the two bands are connected, if an allowed vector goes through those points, we get a metallic energy dispersion without a bandgap. On the other hand, if not, we get a semiconducting dispersion with a bandgap.

(Note that this "zone-folding" picture can be modified by, for example, the curvature of nanotubes which opens gaps in many otherwise metallic nanotubes, although these are typically much smaller than the gap predicted for semiconducting nanotubes in the "zone-folding" picture.) From Equation I.23 or I.24, the metallic condition is when $\overrightarrow{\mathbf{YK}}$ ($\overrightarrow{\mathbf{Y'K''}}$) is a integer multiple of $\mathbf{B}_1$, that is, the remainder of $2n+m$ when divided by 3 is 0 ($2n+m \equiv 0$ *mod*(3)). Since $2n+m \equiv n - m$, in general, $n - m \equiv 0$ *mod*(3) gives metallic tube and the other two cases, $n - m \equiv 1$or $2(-1)$ *mod*(3) give semiconducting ones. In semiconducting cases, it is obvious that two nearby allowed vectors around **K** point dissect the **K** point by ratio 1:2 or 2:1 depending on $p = -1$ or $p=1$, respectively (Figure I-7(c)). But, note that the situation is the opposite for **K'**, 1:2 ($p=1$) and 2:1($p = -1$) due to the symmetry.

### I-2-4 Energy Dispersions for Armchair and Zigzag Tubes

As an example, we will calculate the energy dispersion relations for armchair tubes (($n$, $n$)) and zigzag (($n$, 0)) tubes.

First, for ($n$, $n$) armchair tubes, from Equation I.17, I.18, and I.20,

$$\mathbf{B}_{1,arm} = \frac{\mathbf{b}_1 + \mathbf{b}_2}{2n} = \frac{2\pi}{\sqrt{3}an}\hat{\mathbf{k}}_x$$
$$\mathbf{B}_{2,arm} = \frac{\mathbf{b}_1 - \mathbf{b}_2}{2} = \frac{2\pi}{a}\hat{\mathbf{k}}_y \quad . \qquad \text{(I.25)}$$

Then, allowed vectors are $l\mathbf{B}_{1,arm}$, where $l$ is $0 \le l \le 2n$-1. Using Equation I.12, I.21, and I.25,

$$E_{1D,arm}(k) = \pm t\sqrt{1+4\cos\left(\frac{l\pi}{n}\right)\cos\left(\frac{ka}{2}\right)+4\cos^2\left(\frac{ka}{2}\right)} \qquad \text{(I.26)}$$

where $ka$ is $-\pi \le ka \le \pi$. Plots of Equation I.26 for (4, 4) and (20, 20) armchair tubes are shown in Figure I-8. For (4, 4) tube, there are 10 different subbands; half of the total belongs to conduction or valence bands. From the top, the quantum number, $l$ is specified. The colored bands are non-degenerate. Also, **K** and **K'** points are shown where the first conduction subband and the first valence band meet ($ka = \pm 2\pi/3$). In Figure I-8(b), the first a few subbands for (20, 20) tube (diameter, d ≈ 2.7 nm) are shown. In general, for ($n$, $n$) armchair tube, there are $2n$ conduction subbands and $2n$ valence ones. For each class, 2 subbands, which correspond to the top and the bottom at $ka = 0$, are non-degenerate and the other $n$-1 are doubly degenerate.

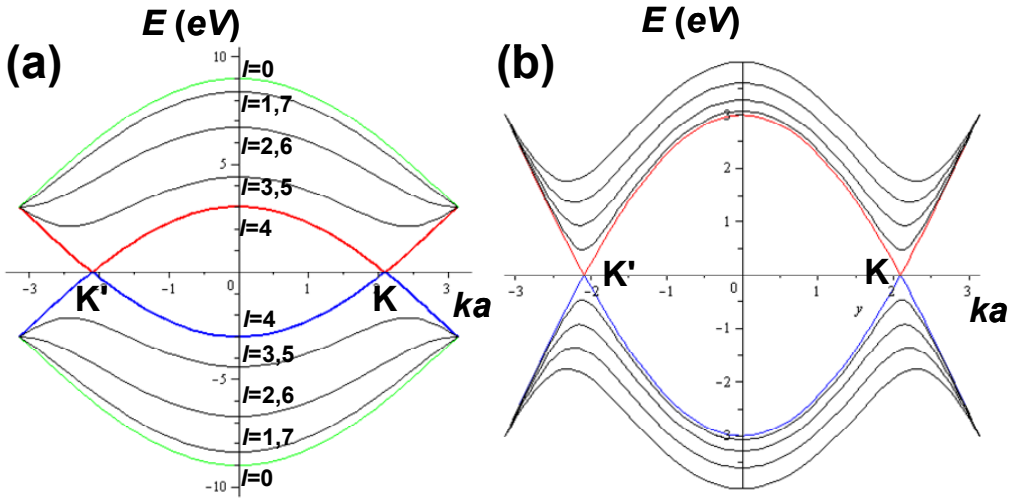


Figure I-8. Energy dispersion for armchair tubes. (a) For (4, 4) tube, there are 5 conduction subbands and another 5 valence ones. **K** and **K'** points are shown where the first conduction subband and the first valence band meet ($ka=\pm 2\pi/3$). Also the quantum numbers $l$ corresponding to each subband are specified. There are two non-degenerate subbands for each conduction and valence band (colored ones). (b) First few subbands for a (20, 20) tube

Second, for ($n$, 0) zigzag tubes,

$$\mathbf{B}_{1,zig} = \frac{2\mathbf{b}_1 + \mathbf{b}_2}{2n} = \frac{2\pi}{an}\left(\frac{\sqrt{3}}{2}, \frac{1}{2}\right). \quad \text{(I.27)}$$

To simplify the Equation I.12, we can rotate the vector by $-\pi/3$ (counterclockwise) using 6-fold symmetry. Then,

$$\mathbf{B}'_{1,zig} = \frac{2\pi}{an}\hat{\mathbf{k}}_y \quad \text{(I.28)}$$

The energy dispersions for ($n$, 0) zigzag tubes are

$$E_{1D,zig}(k) = \pm t\sqrt{1 + 4\cos\left(\frac{\sqrt{3}ka}{2}\right)\cos\left(\frac{l\pi}{n}\right) + 4\cos^2\left(\frac{l\pi}{n}\right)} \quad \text{(I.29)}$$
$$, \left(-\frac{\pi}{\sqrt{3}} < ka < \frac{\pi}{\sqrt{3}}\right), \quad (l = 0, ..., 2n-1).$$

Plots for (8, 0) and (34, 0) tubes are shown in Figure I-9. (8, 0) tube has energy bandgap, $E_g$ of 1.4eV, while for larger (34, 0) tube (diameter, $d$ = 2.7nm), $E_g$ = 0.32eV.

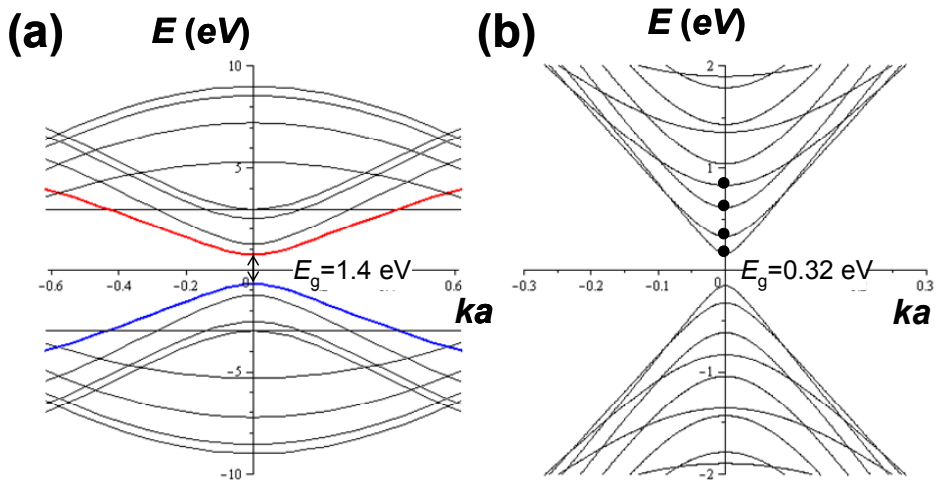


Figure I-9. Subbands for zigzag tubes. (a) All subbands for a (8, 0) tube are plotted. The energy gap, $E_g$ =1.4eV. (b) First a few subbands for a (34, 0) tube are shown. $E_g$ =0.32eV. Black dots correspond to the onset of subbands from $E$=0.

### I-2-5 Low-Energy Approximation

In the case where we consider only low-energy excitations, the energy dispersion relation for 2D graphene (Equation I.12) and 1D nanotube (Equation I.21) can be approximated by a simple form. For a wavevector, **k** staying near **K** point (Figure I-10(a)),

$$\mathbf{k} = \overrightarrow{\Gamma\mathbf{K}} + \mathbf{k}_1 + \mathbf{k}_2 \qquad \text{(I.30)}$$

where $\overrightarrow{\Gamma\mathbf{K}} = \left(\frac{2\pi}{\sqrt{3}a}, \frac{2\pi}{3a}\right)$. In components,

$$\mathbf{k}_x = \frac{2\pi}{\sqrt{3}a} + \mathbf{k}_1, \quad \mathbf{k}_y = \frac{2\pi}{3a} + \mathbf{k}_2. \qquad \text{(I.31)}$$

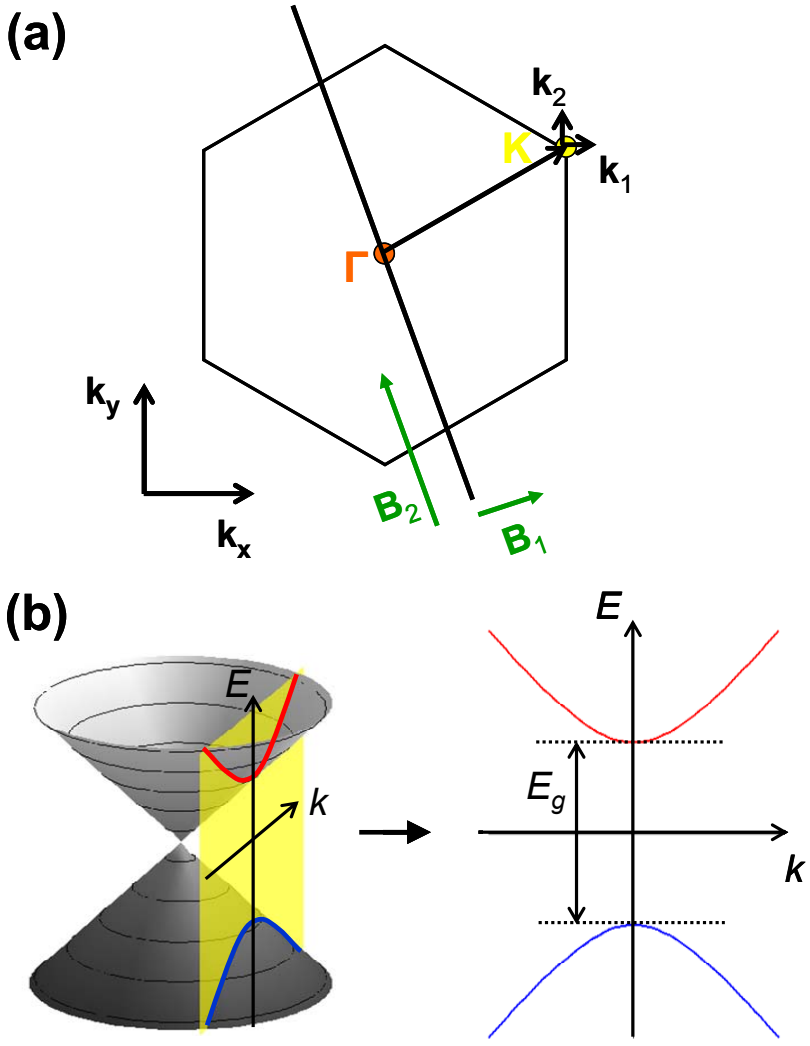


Figure I-10. Low-energy approximation

Plugging Equation I.31 into Equation I.12 and using Taylor expansion for small $\mathbf{k}_1$ and $\mathbf{k}_2$, 2D graphene energy dispersion becomes

$$E_{2D} = \mp \hbar v_F \sqrt{\mathbf{k}_1^2 + \mathbf{k}_2^2}\,, \qquad \text{where } v_F = \frac{\sqrt{3}}{2\hbar} ta\,. \quad \text{(I.32)}$$

Using known values for $t$ and $a$, $v_F \approx 8.7\times10^5$ m/s. Equation I.32 implies that for low-energy modes, energy dispersions for 2D graphene can be approximated by cones with **K** point as origin. For nanotubes, we need to take slices from the cones with planes according to allowed wavevectors (yellow plane in Figure I-10(b)). Then, in general, 1D nanotube low-energy dispersion can be written as

$$E_{1D} = \pm\sqrt{\left(\frac{E_g}{2}\right)^2 + \left(\hbar v_F k\right)^2} \qquad \text{(I.33)}$$

where $E_g$ is the energy gap obtained when cut from the closest allowed wavevector and shown in Figure I-10(b). From Figure I-7(c), the distance from K point to the closest wavevector for semiconducting tubes ($p \neq 0$) is $\frac{1}{3}|\mathbf{B}_1| = \frac{1}{3}\cdot\frac{2\pi}{\pi d} = \frac{2}{3d}$ (using Equation I.19). Then, from Equation I.32,

$$E_g = \frac{4\hbar v_F}{3d} = \frac{0.72\,\text{eV}}{d(\text{nm})}. \qquad \text{(I.34)}$$

The energy gap is inversely proportional to the tube diameter. Likewise, we can also get the energy required to reach following available subbands (Figure I-11(c) and (d)). For a metallic tube, $E_{11}$, $E_{12}$=$E_{11}$/2, $E_{13}$=$E_{11}$/2,… and for a semiconducting tube, $E_g$, $E_g$/2, $E_g$, $E_g$/2,… Note that for similar diameter tubes, $E_{11}$=3$E_g$. In other words, a metallic tube takes the full spacing of $|\mathbf{B}_1| = \frac{2}{d}$, whereas a semiconducting one does $\frac{1}{3}|\mathbf{B}_1| = \frac{2}{3d}$ (Figure I-11(a) and (b)).

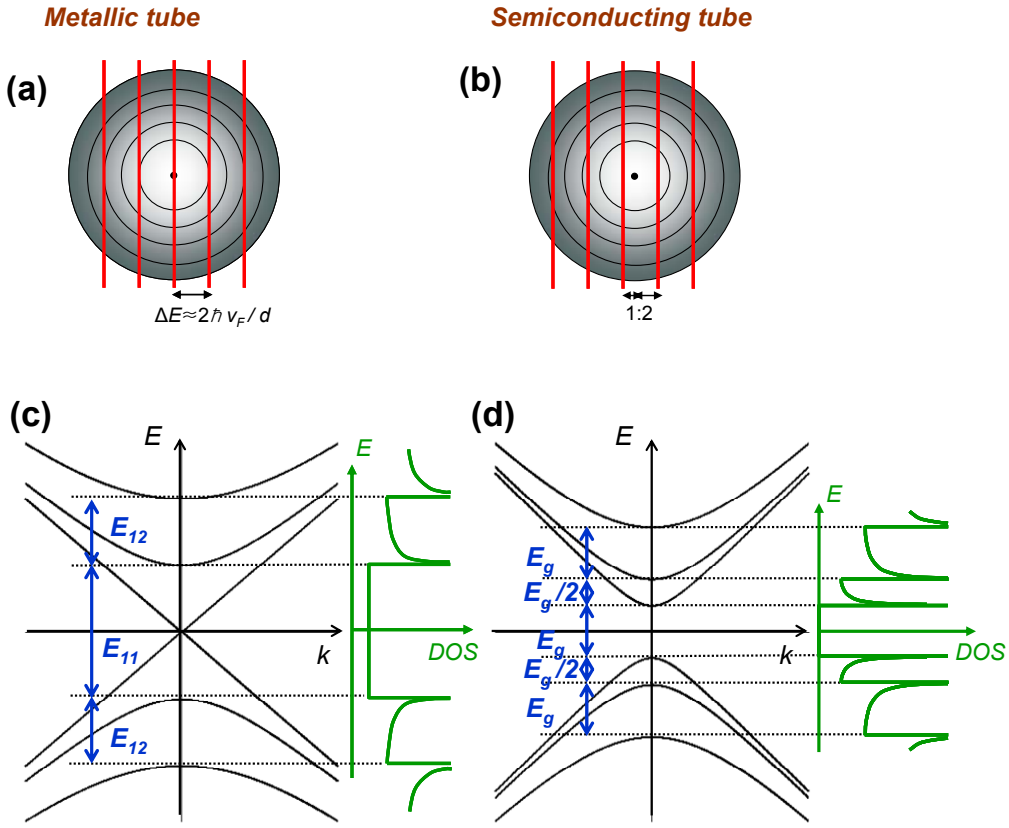


Figure I-11. Subbands for metallic and semiconducting tubes in low-energy approximation. (a), (b) When approximating energy dispersion of 2D graphene as a cone around **K** point, contour plots of constant energy surfaces are concentric circles. Allowed wavevectors (red lines) are passing through **K** point in metallic case (a) or miss by 1:2 ratio in semiconducting case (b). (c), (d) Subbands for metallic (c) and semiconducting tubes (d) and energy spacing between subbands. Also the density of states is shown (green curves) to the right of the main panels of (c) and (d), respectively.

The energy dispersion and following subband locations for low energy (Figure I-11) are valid in Figure I-8(b) and Figure I-9(b) for moderate diameter tubes ($d \approx 2.7$ nm), but not for small diameter tubes (see Figure I-8(a) and Figure I-9(a)). Later on in this chapter, we found for most of our synthesized tubes, $d \geq 2$ nm, so this approximation can be applied.

1D density of states (DOS) of metallic and semiconducting nanotubes are also shown as green curves in Figure I-11(c) and (d), respectively. As expected, on the onset of subbands, DOS increases rapidly (van Hove singularity). For a semiconducting tube, there are no available states within the energy gap. But for a metallic tube, DOS has a constant value due to linear dispersion subbands. This value can be determined as follows. The density of $k$ points in 1D reciprocal space, $n$ is $4k/\pi$ (considering factor 2 for spin and another 2 for twofold subband degeneracy in nanotubes). Also for linear dispersion relations, $dk/dE = 1 / (\hbar v_F)$. Then, constant density of states is given by

$$\frac{dn}{dE} = \frac{dn}{dk} \cdot \frac{dk}{dE} = \frac{8}{hv_F}. \quad \text{(I.35)}$$

### I-2-6 Modified Band Structure by Uniaxial Strain Induced in Nantubes[5-7]

#### K points shifts due to strain in graphene band structure

When uniaxial strain is applied to a graphene sheet, the band degeneracy points move within the Brillouin zone. Thus to begin, it is necessary to determine the new positions of **K** points. In Figure I-12, the coordinates of the three nearest neighbors around a blue carbon atom are given in units of lattice vector, $a$, when unstrained and strained along $x$-axis. Strain $\sigma$ is given by the change of the length to the original length, $\Delta l/l$ and the length change perpendicular to the strain axis is given by $-\sigma\upsilon$, where $\upsilon$ is the Poisson ratio of the material. When we calculated the energy of 2-D graphene, we assumed that the transfer integral, $t_i$, is the same for the three nearest neighbors in Equation I.9. But, instead,

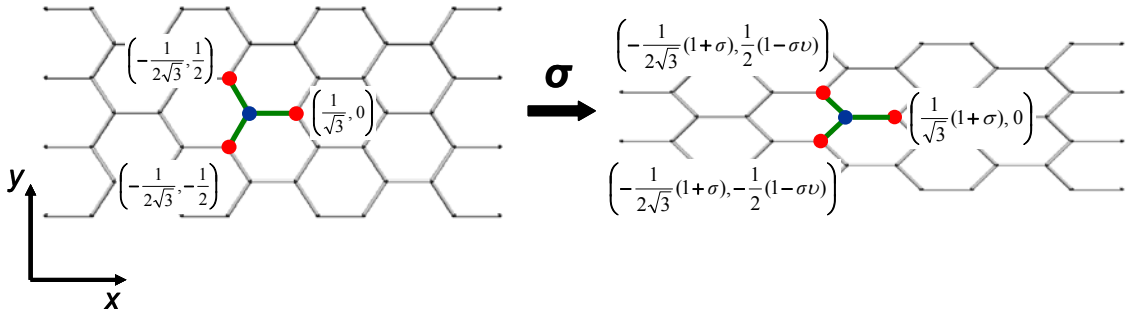


Figure I-12. Strained honeycomb lattices

we have $t_1$, $t_2$, and $t_3$=$t_2$ by breaking the symmetry along $x$-axis ($s$ remains still small, $s \approx 0$). With new coordinates for the three nearest neighbors and different transfer integrals, Equation I.9 becomes

$$\begin{aligned} -E\,b_1 + b_2\left(t_1\,\mathrm{e}^{\frac{(1+\sigma)i}{\sqrt{3}}k_x} + 2t_2\,\mathrm{e}^{-\frac{(1+\sigma)i}{2\sqrt{3}}k_x}\cos\left(\frac{1}{2}(1-\sigma\upsilon)k_y\right)\right) &= 0 \\ -E\,b_2 + b_1\left(t_1\,\mathrm{e}^{\frac{(1+\sigma)i}{\sqrt{3}}k_x} + 2t_2\,\mathrm{e}^{-\frac{(1+\sigma)i}{2\sqrt{3}}k_x}\cos\left(\frac{1}{2}(1-\sigma\upsilon)k_y\right)\right) &= 0\,. \end{aligned} \qquad \text{(I.36)}$$

Then, the modified energy dispersion for 2D graphene is given by

$$E_{2D}(k_x,k_y) = \pm\sqrt{t_1^2 + 4t_2^2\cos^2\left(\frac{1}{2}(1-\sigma\upsilon)k_y\right) + 4t_1t_2\cos\left(\frac{1}{2}(1-\sigma\upsilon)k_y\right)\cos\left(\frac{\sqrt{3}}{2}(1+\sigma)k_x\right)}\,. \qquad \text{(I.37)}$$

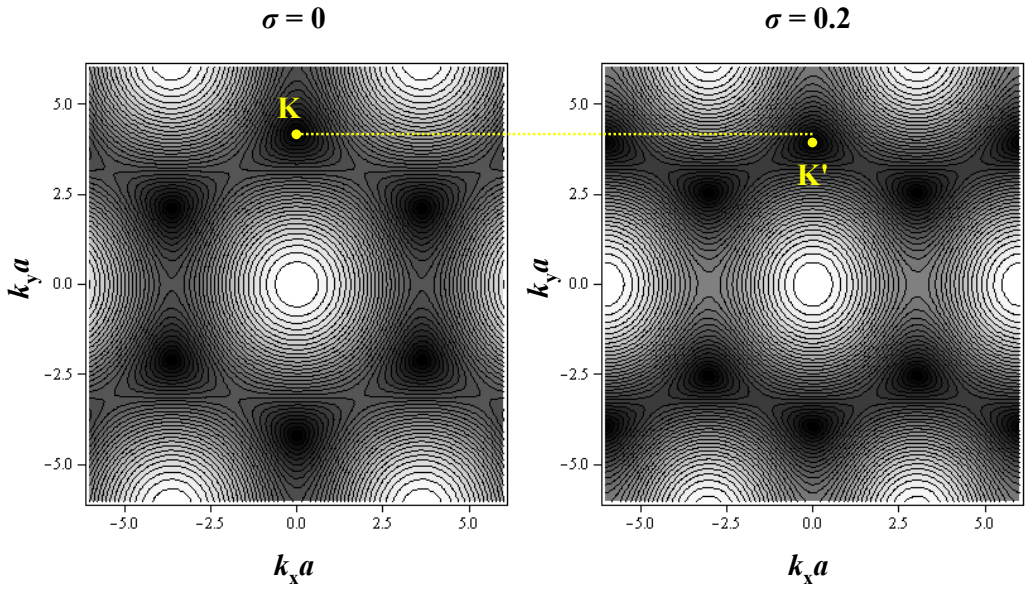


Figure I-13. Contour plots of 2D graphene energy bands for unstrained ($\sigma = 0$) and strained ($\sigma = 0.2$)

From Figure I-3, there is symmetry about the $k_x$ axis, and Equation I.37 still has the same, so the **K** points at the $k_x$=0 must move along that line. Thus we only need to consider $k_x$=0 in Equation I.37 to get the new position of **K**.

$$E_{2D}(k_x = 0,\, k_y) = \pm t_2\left(2\cos\left(\frac{1}{2}(1-\sigma\upsilon)k_y\right) + \frac{t_1}{t_2}\right) \qquad \text{(I.38)}$$

Using approximation $t_i \propto 1/\left|a_{C-C}\right|^2$, [7] where $a_{c\text{-}c}$ is the modified bond length given in Figure I-12, we have for small $\sigma$,

$$\frac{t_1}{t_2} = 1 - \frac{3}{2}(1+\upsilon)\sigma\,. \qquad \text{(I.39)}$$

At the new **K** points, Equation I.38 becomes zero. Plugging Equation I.39 into I.38, and expanding cosine around the original **K** points, $k_y = \pm\frac{4\pi}{3}$, new positions of **K** are given by

$$k_y' = \pm\frac{4\pi}{3}(1+\sigma\upsilon) \mp \sqrt{3}(1+\upsilon)\sigma . \quad \text{(I.40)}$$

For example, Figure I-13 shows unstrained ($\sigma$ = 0) and strained ($\sigma$ = 0.2) contour plots of 2D graphene energy bands. Note that **K'** is different from **K**. Up to now, we have shown that strain induced along *x*-axis changes the position of **K** points. But, although the point moves, the energy dispersion still remains gapless there.

**Modified band structure of nanotubes**

Now we want to deduce the strain-induced energy band change for nanotubes. Since we consider applying strain along the *x*-axis in graphene, which is also the tube axis for zigzag tubes, the modified band structure of zigzag tubes can be derived. For unstrained zigzag tubes, the wavevectors are quantized as in Equation I.28. But, the diameter of tubes is decreased by a factor of (1-$\sigma\upsilon$). Then, the new quantized vectors are

$$k_\perp' = \frac{2}{d'}l = \frac{2}{d(1-\sigma\upsilon)}l = \frac{2\pi}{n(1-\sigma\upsilon)}l \qquad (0 \le l \le 2n-1) \quad \text{(I.41)}$$

where *d* is tube diameter and equal to $n/\pi$. We categorize tubes by *p* value, the remainder when *n*-*m* is divided by 3 (Figure I-7).

**Case 1. *p*=0**

When unstrained, the quantized vector passes through **K** point. But for strained tubes, the closest quantized vector to **K** point is

$$k'_{\perp} = \frac{4\pi}{3(1-\sigma\upsilon)}. \quad \text{(I.42)}$$

Then, using Equation I.40 and I.42, the distance between the new **K** point and the closest quantized vector is

$$\Delta k = \sqrt{3}(1+\upsilon)\sigma. \quad \text{(I.43)}$$

The bandgap induced by Equation I.43 is calculated using Equation I.32,

$$E_g(\sigma) = 3t(1+\upsilon)\sigma \quad \text{(I.44)}$$

where $t$ is the transfer integral when unstrained. In result, axial strain opens a bandgap, $E_g$, for a zigzag metallic tube.

**Case 2. *p*=1**

The quantized vectors are given by

$$k'_{\perp} = \frac{2\pi}{n(1-\sigma\upsilon)} l. \quad \text{(I.45)}$$

The nearest vector when $l = (2n+1)/3$ is

$$k'_{\perp} = \left(\frac{4\pi}{3} + \frac{2\pi}{3n}\right)\cdot(1-\sigma\upsilon)^{-1} \approx \left(\frac{4\pi}{3} + \frac{2\pi}{3n}\right)\cdot(1+\sigma\upsilon)\,. \quad \text{(I.46)}$$

Then, the mismatch between **K** point and the quantized vector is

$$\Delta k = \frac{2}{3d} + \frac{1}{a}\sqrt{3}(1+\upsilon)\sigma\,. \quad \text{(I.47)}$$

We used $d=n/\pi$ and restore $a$. The first term corresponds to the bandgap of unstrained tubes (Equation I.34). From the plus sign of the second term, for $p$=1 tubes, strain increases the bandgap of the unstrained tube by the amount in Equation I.44.

**Case 3. $p=-1$**

We have the same quantized vector (Equation I.45) but with $l$ = (2$n$-1)/3. Then, the mismatch is

$$\Delta k = -\frac{2}{3d} + \frac{1}{a}\sqrt{3}(1+\upsilon)\sigma\,. \quad \text{(I.48)}$$

The bandgap, which is proportional to $|\Delta k|$, decreases with strain because of opposite sign.

We only derived the modified band structure for $\theta$=0º zigzag tubes. But when $\theta$=30º, axial strain moves **K** points along the allowed wavevectors, $\mathbf{k}'_{\perp}$. So the energy gap remains closed even when strained. The generalized expression for $\theta$ chiral tubes,[7]

$$\frac{dE_{gap}}{d\sigma} = \pm 3t(1+\upsilon)\cos 3\theta\,, \quad \text{where} \begin{matrix} + \text{ for } p = 0 \text{ and } 1 \\ - \text{ for } p = -1 \end{matrix}\,. \quad \text{(I.49)}$$

The above expression will be used for estimating the chiral angle of a nanotube from comparison with strain versus energy gap data later.

### I-2-7 Thomas-Fermi Screening Theory[2] and Quantum Capacitance

#### Thomas-Fermi Screening Theory

Suppose a positively charged particle is placed at a given position in the electron gas and rigidly held there. It will then attract electrons, creating a surplus of negative charge in its neighborhood, which screens its field. The potential from the positively charged particle, $\phi^{ext}$ satisfies Poisson's equation.

$$-\nabla^2\phi^{ext}(\mathbf{r}) = 4\pi\rho^{ext}(\mathbf{r}) \qquad \text{(I.50)}$$

where $\rho^{ext}$ is the particle's charge density. The total potential from both the positive and induced negative charge, $\phi$ also satisfies Poisson's equation.

$$-\nabla^2\phi(\mathbf{r}) = 4\pi\rho(\mathbf{r}) \qquad \text{(I.51)}$$

where $\rho$ is the full charge density,

$$\rho(\mathbf{r}) = \rho^{ext}(\mathbf{r}) + \rho^{ind}(\mathbf{r}) \qquad \text{(I.52)}$$

and $\rho^{ind}$ is the charge density induced from negatively charged particle. By analogy with the theory of dielectric media, $\phi$ and $\phi^{ext}$ are linearly related by an equation,

$$\phi^{ext}(\mathbf{r}) = \int d\mathbf{r}'\varepsilon(\mathbf{r}-\mathbf{r}')\phi(\mathbf{r}') \qquad \text{(I.53)}$$

where $\varepsilon(\mathbf{r})$ is dielectric constant only depending on separation. The Fourier transform of Equation I.53 gives

$$\phi(\mathbf{q}) = \frac{1}{\varepsilon(\mathbf{q})}\phi^{\text{ext}}(\mathbf{q}). \quad \text{(I.54)}$$

Similarly, when $\rho^{\text{ind}}$ and $\phi$ are linearly related, then their Fourier transforms are given by

$$\rho^{\text{ind}}(\mathbf{q}) = \chi(\mathbf{q})\phi(\mathbf{q}) \quad \text{(I.55)}$$

where $\chi(\mathbf{q})$ is related to $\varepsilon(\mathbf{q})$ by

$$\varepsilon(\mathbf{q}) = 1 - \frac{4\pi}{q^2}\chi(\mathbf{q}) = 1 - \frac{4\pi}{q^2}\frac{\rho^{\text{ind}}(\mathbf{q})}{\phi(\mathbf{q})}. \quad \text{(I.56)}$$

Here we used Fourier transform of Poisson's equations (Equation I.50 and I.51) together with Equation I.52 and I.55.

In principle, to find the charge density in the presence of the total potential, $\phi$ we must solve the one-electron Schrodinger equation,

$$-\frac{\hbar^2}{2m}\nabla^2\psi(\mathbf{r}) - e\phi(\mathbf{r})\psi(\mathbf{r}) = E\psi(\mathbf{r}) \quad \text{(I.57)}$$

and then construct the electronic density from $\rho(\mathbf{r}) = -e|\psi(\mathbf{r})|^2$. The Thomas-Fermi picture simplifies this procedure when the total potential $\phi(\mathbf{r})$ is a very slowly varying function to satisfy

$$E(\mathbf{k}) = \frac{\hbar^2 k^2}{2m} - e\phi(\mathbf{r}). \quad \text{(I.58)}$$

Thus, the energy is modified from its free electron value by the total local potential. Equation I.58 is only meaningful in terms of wave packets, which are spread in position at least of the order of Fermi wavelength. So, we must require that $\phi(\mathbf{r})$ vary slowly on the scale of a Fermi wavelength.

The induced charge density is given by

$$\rho^{\text{ind}}(\mathbf{r}) = -e\left[n(\mu + e\phi(\mathbf{r})) - n(\mu)\right] \quad \text{(I.59)}$$

where $n$ is number density, $n(\mathbf{r}) = \int \frac{d\mathbf{k}}{\mathbf{4\pi^3}} \frac{1}{\exp[(\hbar^2 k^2/2m - e\phi(\mathbf{r}) - \mu)/kT] + 1}$ and $\mu$ is chemical potential. Equation I.59 obviously vanishes when $\phi$ is zero. When $\phi$ is small enough for Equation I.59 to be expended to give in leading order

$$\rho^{\text{ind}}(\mathbf{r}) = -e^2 \frac{\partial n}{\partial \mu} \phi(\mathbf{r}). \quad \text{(I.60)}$$

Substituting this into Equation I.56,

$$\varepsilon(\mathbf{q}) = 1 + \frac{k_{TF}^2}{q^2} \quad \text{(I.61)}$$

where $k_{TF}$ is Thomas-Fermi wave vector,

$$k_{TF}^2 = 4\pi e^2 \frac{\partial n}{\partial \mu}. \quad \text{(I.62)}$$

For example, in case of point external charge, $\phi^{\text{ext}}(\mathbf{r}) \sim \frac{1}{r}$, one can show the total potential, $\phi$ is given by $\phi(\mathbf{r}) \sim \frac{1}{r} e^{-k_{TF} r}$. That means that the original Coulomb potential is effectively screened by surrounding induced negative charge on the order of $1/k_{TF}$. Then we can define Thomas-Fermi screening length, $l_F$

$$l_F = \frac{1}{k_{TF}} \quad \text{(I.63)}$$

which measures a distance where the screened potential is substantially decreased.

**Quantum Capacitance**

The quantum capacitance reflects the energy cost due to the Fermi level increase of putting an electron into electron gas system (for example, here, nanotube). The energy cost approximately accounts for the kinetic, exchange, and correlation energy of the electrons.

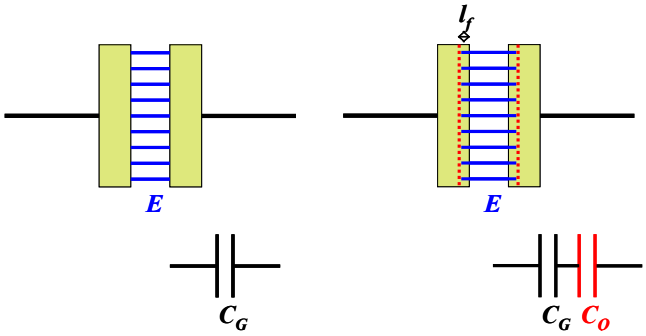


Figure I-14. Quantum correction to normal conductor

Another way of stating this is that in a normal perfect conductor, the electric field stops at its surface (Figure I-14 left), and does not penetrate into the conductor. But in reality, it actually penetrates on the order of Thomas-Fermi screening length, $l_f$ (Equation I.63) (Figure I-14 right). This adds a quantum capacitance, $C_Q$ as a quantum mechanical correction to geometrical capacitance, $C_G$ in series.

Quantitatively, it depends on how many states are available in given range of energy, that is, the density of states. Note that Equation I.60 resembles $Q=C_Q V$. In particular, for a 1D nanotube quantum capacitance is given by

$$C_Q = \frac{\mathrm{d}Q}{\mathrm{d}V} = \frac{\mathrm{d}(enL)}{\mathrm{d}(E/e)} = e^2 \frac{\mathrm{d}n}{\mathrm{d}E} L \qquad \text{(I.64)}$$

where $e$ is electric charge, $n$ is carrier density, $L$ is effective length of nanotube, and $E$ is energy. In macroscopic objects, $C_Q$ is not large enough to appreciably change the total capacitance, and thereby, we can neglect the quantum correction. But, in 1D mesoscopic materials like nanotubes, $C_Q$ can yield a large contribution. For example, in our EFM experiment below, $C_Q$ of a metallic tube changes the total capacitance by 20% even without a water meniscus. Because the quantum capacitance of nanotube is directly proportional to the density of states, at one of the van Hove singularities, we expect it to increase rapidly, and, as a result, it becomes observable as a peak in our EFM data.

## I-3 Fabrication

### I-3-1 Growing Single-Walled Carbon Nanotubes

A degenerately doped silicon wafer capped with a 1 μm oxide layer provides the substrate for single-walled carbon nanotubes (SWNTs) grown by chemical vapor deposition (CVD) [8]

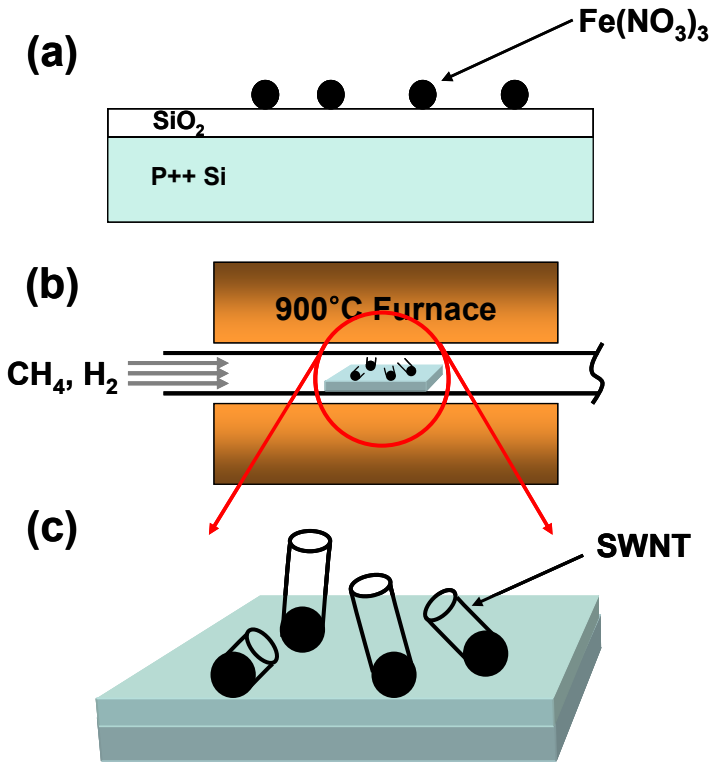


Figure I-15. Carbon nanotube growth procedure (a) Cross-section view of silicon wafer with exaggerated catalyst particles. (b) During a high temperature reaction. (c) Grown SWNTs

Briefly, a small size (~ 2×2 $mm^2$) silicon wafer chip was dipped into a solution of ferric nitrate ($Fe(NO_3)_3 \cdot 9H_2O$) dissolved in isopropyl alcohol (IPA) (typical concentration, ~1 mg/100 mL) for about 10 seconds, and the ferric nitrate catalyst was fixated in hexane for 5 seconds (Figure I-15(a)). Activated iron catalyst particles in the 900ºC furnace become the growth sites of carbon nanotubes, where the carbon feedstock gas, methane, is decomposed (Figure I-15(b)).

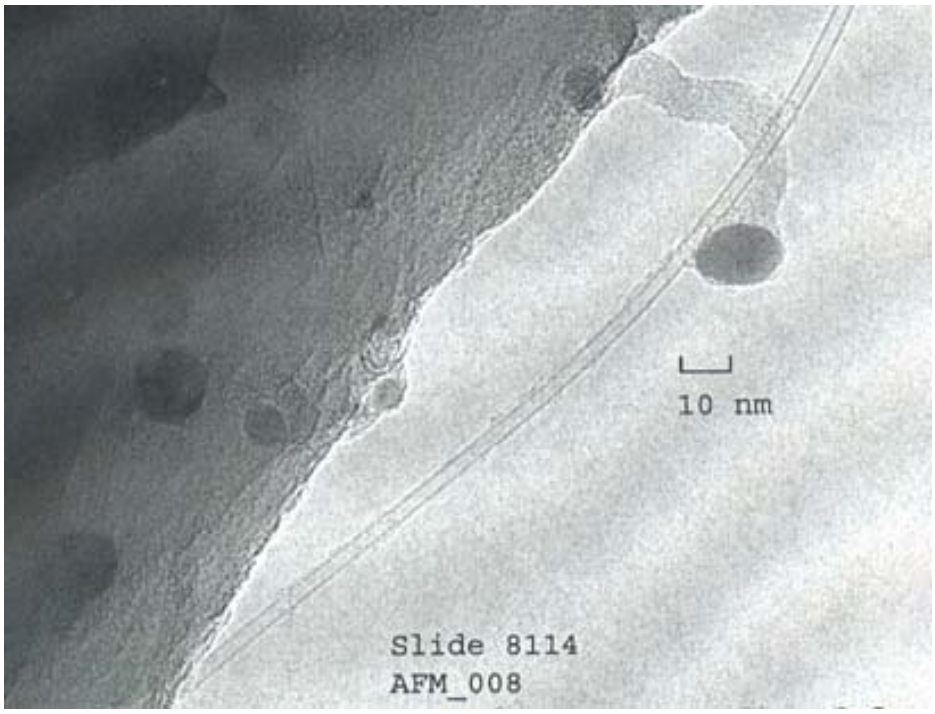


Figure I-16. Transmission Electron Microscope (TEM) image of our CVD grown single-wall carbon nanotubes

The above image is obtained from a transmission electron microscope (TEM). It shows one clean single-walled carbon nanotube from many grown nanotubes. Judging from TEM images, most of the CVD-grown tubes are single-walled.

**I-3-2 Electron Beam Lithography (EBL) by Scanning Electron Microscope (SEM)**

After growing nanotubes, first, a bi-layer of MAA(8.5)/PMMA(950) resist (Mirochem) is spun on the sample (Figure I-17(a)). MAA and PMMA are positive-radiation-sensitive resist and typically used for EBL.

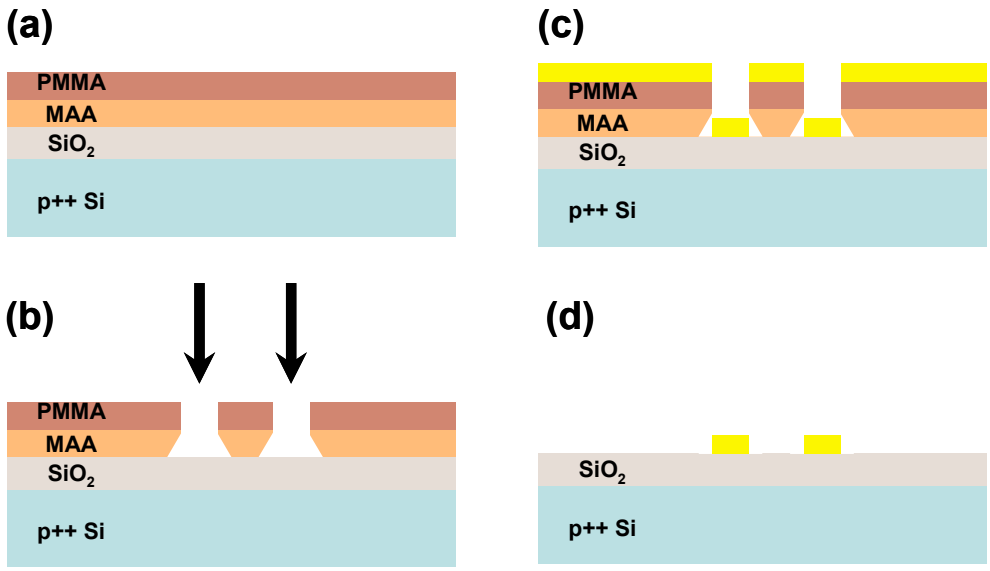


Figure I-17. Electron beam lithography (a) PMMA/MAA bi-layer of positive resist is spun on the substrate. (b) An electron beam exposes the defined area and the sample is developed to make a window. (The MAA layer has an undercut, which makes lift-off process (d) easier.) (c) Metal is evaporated onto the sample surface through the window. (d) Lift-off of the remaining resist

Secondly, the electron beam exposes the defined area (Figure I-17(b)) using the Nanometer Pattern Generation System (NPGS) integrated in our SEM (Model S-4100 Field Emission HITACHI SEM). After evaporating metal (Cr/Au, 5 nm/40 nm, the thin Cr layer gives good adhesion to the oxide surface) (Figure I-17(c)), the remaining resist is lifted off using acetone or dichloroethane (Figure I-17(d)).

### I-3-3 Imaging Nanotubes by Scanning Electron Microscope (SEM)

A fast and efficient imaging technique using SEM was developed.[9] When the electron beam scans the insulating surface, electrons are deposited, charging the surface negatively. This reduces the secondary electrons emitted from the surface. But, when it scans over carbon nanotubes, the charge can disperse over the conducting tube, so the secondary electrons from the tube escape more easily than those from the substrate, showing the surface potential difference. In other words, the difference in capacitance between the insulating silicon dioxide and nanotubes produces a surface voltage contrast that produces a bright image of the nanotubes. This imaging technique is typically at least an order of magnitude faster in time than AFM imaging.

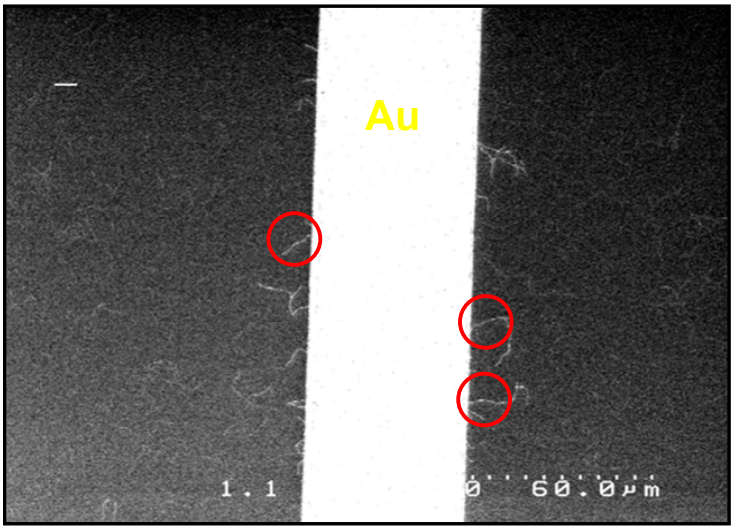


Figure I-18. SEM image of nanotubes attached to gold electrode. Center white bar is strip of gold electrode, and red circled area shows where nanotubes are attached to it.

As seen from Figure I-18, nanotubes, appearing white inside the red circled areas attached to a gold electrode (also white), are easily discerned from insulating substrate, which appears dark.

### I-4 Measuring Current Versus Gate Voltage Characteristic Curve with Atomic Force Microscope (AFM)

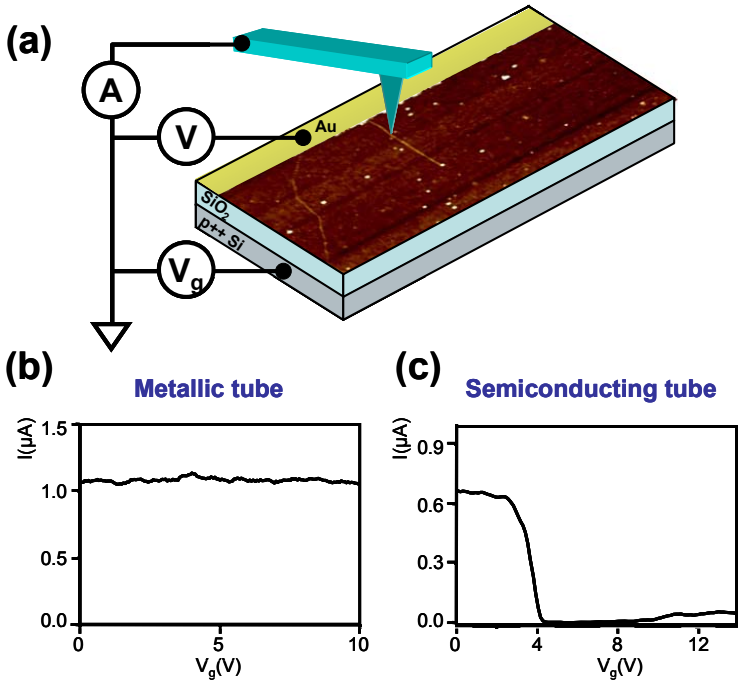


Figure I-19. Conducting AFM experiment (a) Conducting AFM setup. While a voltage, $V$, is applied to Au electrode, a grounded AFM tip was mechanically and electrically in contact with a nanotube. The back gate voltage, $V_g$, through heavily hole doped silicon ($p$ ++ Si) is swept to obtain $I$-$V_g$ characteristic curve (Figure I-6(b), (c)). (b) $I$-$V_g$ characteristic curve for a metallic tube. Current, $I$, is kept constant as $V_g$ varies. (c) $I$-$V_g$ characteristic curve for a semiconducting tube, in which $I$ is turned off as $V_g$ increases.

Once the SEM image is taken, knowing where attached tubes are, it is easy to bring an AFM tip onto a specific tube to do transport measurement. We performed conducting AFM

[10-12], which utilizes an AFM tip as another probe in addition to existing gold electrode for two terminal transport measurements.

Once a nanotube is centered in the AFM non-contact mode scan image, a nanoscript incorporated in our AFM was loaded to move the tip to the center and push down gently to make contact mechanically and electrically with the nanotube. Through heavily doped silicon back plane, a gate voltage was applied (Figure I-19(a)). A p-type semiconducting tube is turned off as gate voltage increases, whereas the metallic tube's conductance remains the same (Figure I-19(b) and (c)). This is because increasing the gate voltage capacitively changes the Fermi level of a semiconducting tube to the band gap region, suppressing the current. On the other hand, the current through the metallic one, not having a gap comparable or larger than the thermal energy $k_BT$, remains unchanged.

## I-5 Electrostatic Force Microscopy

### Overview

Briefly, in this EFM experiment, samples prepared as in Figure I-18 or I-19 are used. First, we bring an AFM tip a few nanometers from nanotubes in Si oxide. Then, by applying and varying voltage to the tip, we change the chemical potential of nanotubes through the density of states (Figure I-11) effectively. The AFM tip is capacitively coupled to nanotube with the geometrical capacitance and quantum capacitance in series (Figure I-14 and A-1). Since the quantum capacitance of a 1D nanotube is appreciable, abrupt change in quantum capacitance at van Hove singularities

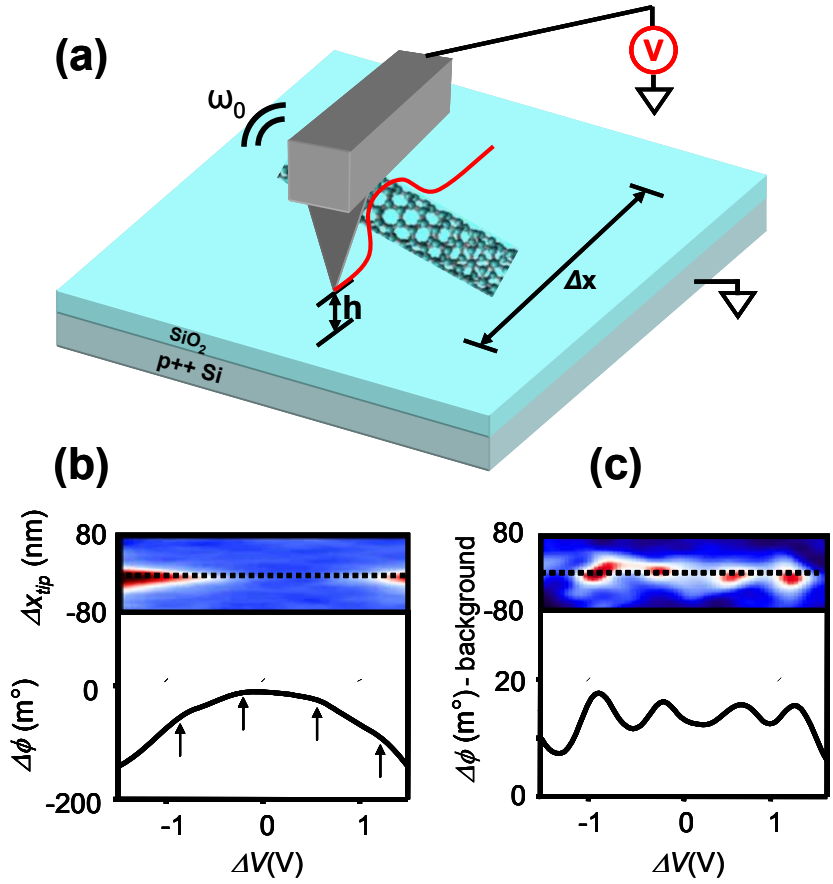


Figure I-20. Experimental geometry and cantilever response to electrostatic forces (a) A vibrating cantilever with free amplitude A is brought close to a nanotube supported by an oxidized Si wafer. In the topographic scan, feedback maintains the amplitude at a reduced value of Atap. (b) Upper panel: color plot of $\Delta\phi$ versus $\Delta x$ and voltage $\Delta V = V - V_{min}$, where $V_{min}$ (typically ~ 1V) corresponds to a maximum in $\Delta\phi$ obtained with h = 30 nm, A ~ 150 nm, $A_{tap}$ ~ 100 nm. The data are smoothed over a ~ 10 pixel radius. Dark red corresponds to -150 m° while dark blue corresponds to 0.0 m°. The dotted line indicates the nanotube position. Lower panel: $\Delta\phi$ versus $\Delta V$ when the tip is directly above the nanotube. Arrows mark kinks in $\Delta\phi$ versus $\Delta V$. (c) upper panel: color plot of $\Delta\phi$ versus $\Delta x$ and $\Delta V$ with a smooth background subtracted. Dark red corresponds to 20 m° while dark blue corresponds to 5 m°. When the tip is directly over the nanotube, the data show peaks in $\Delta\phi$ versus $\Delta V$. Lower panel: $\Delta\phi$ versus $\Delta V$ taken along the dotted line exhibiting a series of peaks. The voltages giving the peaks correspond to the voltages yielding the kinks in the data of part (b).

should be reflected in our EFM data. Therefore, the DOS of individual nanotubes are resolved. The energy scale between measured van Hove peaks with nanotube diameter tells us whether the specific tube is metallic or semiconducting (Equation I.34). Our ability to distinguish tubes is further confirmed by pre-performed 3-terminal contact measurement. Finally, the van Hove peaks of a strained tube are also measured. The modified band structure of strained tube is observed and compared to theory (Section I-2-6).

The following are details of the EFM measurement and discussion largely adopted from our paper.[1] An Si AFM tip which vibrates near its resonant frequency is used for acquiring a topographic image of a selected nanotube. A nanotube is located perpendicular to the scan axis. Once it is located, the slow scan axis is disabled so that the AFM tip traces the same nominal line (red curve in Figure I-20(a)). In the second pass of the tip over the nanotube, using the tapping mode height information from the first pass, the tip is lifted at a larger height $h$ relative to the sample. With careful adjustment of $h$, during the lowest point of oscillation the tip-sample separation distance becomes less than a few nm. A bias voltage $V$ is also applied between the tip and sample ground plane (Figure I-20(a)). (The nanotube is grounded either by its capacitance to the ground plane, or by attached electrodes[13].)

The positively or negatively charged tip experiences electrostatic force when it is over the nanotube because of induced charge in the nanotube under the tip. The resonant frequency of the tip, $\omega_0$, is changed due to additional electrostatic force term in the equation of tip motion. Then, the phase is shifted by $\Delta\phi$. Bias voltage $V$ is incremented at the end of

each scan line. As $V$ varies, different electrostatic forces acting on the cantilever's tip modulate $\Delta\phi$.

The upper panel of Figure I-20(b) shows a color scale plot of $\Delta\phi$ versus $\Delta V$ and tip position $\Delta x$ for a 0.9 nm diameter SWNT, where $\Delta V$ includes an offset to account for tip-sample work function differences. The dashed line indicates the nanotube position. The lower panel of Figure I-20(b) shows a line trace of $\Delta\phi$ versus $\Delta V$ when the tip is directly over the nanotube. The line trace approximately follows the trend $\Delta\phi \propto -\Delta V^2$, as reported and elucidated in previous studies.[13,14]

Treating our system as a harmonic oscillator, the equation of motion is given by $m\,d^2z/dt^2 + r\,dz/dt + kz = F_0\cos(\omega t)$, where $m$ is the mass, $z$ is the displacement, $r$ is the damping amplitude, $k$ is the spring constant, and $F_0$ is driving force amplitude with frequency $\omega$. Then, the solution is $z(t) \propto \sin(\omega t - \Delta\phi)$, where $\tan\Delta\phi = (\omega^2 - \omega_0{}^2)/(r\omega/m)$. For a small change of phase, $\Delta\phi \propto \Delta\omega$. On the other hand, the potential energy is $U \propto C_{TS}(V + \varphi - V_S)^2$, where $C_{TS}$ is tip-sample capacitance, $\varphi$ is the work function difference between tip and sample, and $V_S$ is the voltage within the sample. Therefore, $dF/dz \propto \Delta\phi \propto -(d^2C_{TS}/dz^2)\,\Delta V^2$.

Remarkably, the data shows kinks at the voltages indicated by the arrows in Figure I-20(b). To perform further analysis, a smooth background is subtracted, yielding Figure I-20(c), which is approximately proportional to $-d^2(\Delta\phi)/dV^2$ and enhances the contrast of these features. The upper panel in Figure I-20(c) shows the background-subtracted

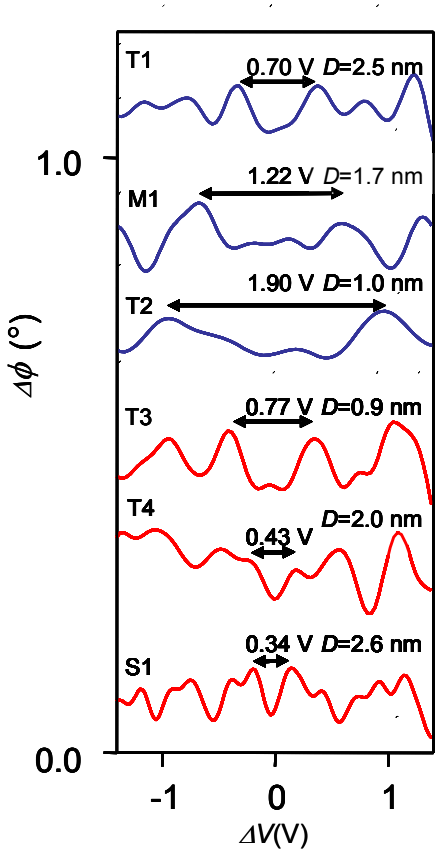


Figure I-21. Background subtracted $\Delta\phi$ versus $\Delta V$ for six nanotube samples T1−T4, S1, and M1. S1 and M1 were determined by transport measurements to be semiconducting and metallic, respectively, while no electrodes were attached to T1−T4. The peaks are offset horizontally slightly to align the minima, and offset vertically for clarity. To obtain a consistent vertical scale, the data have been scaled by a multiplicative factor for each tube. The scale factors for each sample are T1, ×10; T2, ×4; S1, ×0.5; T3, ×10; M1, ×0.6; T4, ×6. Data from T1 -T4 were taken with $\Delta h$ = ~ 30 nm, $A$ ~ 150 nm, $A_{tap}$ ~ 100 nm, while data from S1 and M1 was taken with $\Delta h$ =7 nm, $A$ ~ 30 nm, $A_{tap}$ ~ 15 nm. The combination of smaller $A$ and $\Delta h$ typically gives larger peaks in $\Delta\phi$ versus $\Delta V$, as reflected by the smaller scale factors for S1 and M1. The voltage gap $V_g$ between peaks surrounding $\Delta V$ =0 is indicated, along with the diameter D for each tube. $V_g$ depends on the nanotube diameter. For a given diameter, the data from samples with relatively small $V_g$ are shown in red, and those with a large $V_g$ are shown in blue.

$\Delta\phi$ versus $\Delta x$ and $\Delta V$ in a color scale. When the tip is directly over the nanotube, $\Delta\phi$ shows a series of peaks as $\Delta V$ varies. These peaks occur at the same voltage positions of the kinks shown in Figure I-20(b). The line trace shown in the lower panel shows peaks at $\Delta V = -0.2$ V and $\Delta V = 0.7$ V, as well as additional peaks near $\Delta V \sim \pm 1$ V.

The voltage position of the peaks is nanotube-dependent. Figure I-21 shows $\Delta\phi$ versus $\Delta V$ for six different nanotubes, labeled T1−T4, S1, and M1. Transport measurements were performed on S1 and M1 (I-3-3). S1 was determined from these measurements to be semiconducting, while M1 was determined to be metallic. For each tube, a gap region near $\Delta V$=0 is surrounded by peaks of typical width ~ 150 mV, with additional peaks at larger $|\Delta V|$. The small features that occur within the gap region in M1 and features of similar relative magnitude in the other data are likely noise, as determined by comparing their magnitude to the noise background found when the tip was away from the nanotubes. Arrows delineate the voltage gap $V_g$ and the measured nanotube diameter D is given.

To understand this behavior, we consider $\Delta\phi \propto -(d^2C_{TS}/dz^2)\,\Delta V^2$. The tip-sample capacitance $C_{TS}$ should reflect contributions both from the geometric capacitance $C$ as well as a quantum capacitance $C_Q = e^2n^2\kappa L$ in series with $C$ (Section I-2-7), where $\kappa = n^{-2}dn/d\mu$ is the electron gas compressibility, $n$ is the carrier density, $L$ is the characteristic length of the tip-sample capacitor, and $\mu$ is the chemical potential. This series addition of $C_Q$ to $C$ accounts approximately for the kinetic, exchange, and correlation energy of the electrons. From *ab* initio calculations[15] we expect $C_Q$ makes an appreciable

contribution to the $C_{TS}$ for a nanotube, regardless of $L$, originating from nanotubes' quasi -1D nature.

For the chemical potential of the nanotube such that electrons just begin to occupy each additional subband (for example, see Figure I-11), the 1-D density of states has a van Hove singularity. $C_Q$ then becomes large with rapid increase of DOS, and the induced charge on the nanotube will increase more rapidly with $\Delta V$. A quantitative calculation, however, of $\Delta\phi$ versus $\Delta V$ requires numerical computations, since the forces acting on the tip are strongly anharmonic. Nevertheless, the abrupt increase in induced charge when the Fermi level is at a 1D van Hove singularity should produce kinks in $\Delta\phi$ versus $\Delta V$, as observed. Upon subtracting a smooth background these kinks will yield peaks.

For metallic nanotubes, the energy separation between the van Hove singularities near the Fermi level is $eV_g[eV] \approx 2.16\, D^{-1}$ [nm$^{-1}$] from Equation I.34 and following discussion. Energy dispersion relation from tight-binding calculation is $E_g = |t|\, a_{C-C}/D$, where $|t|$=2.5 eV is the hopping integral, $a_{C-C} = a/\sqrt{3} = 0.83$ is the nearest-neighbor C-C distance on a graphene sheet, and $E_g = 2.08\, D^{-1}$ [nm$^{-1}$]. While small band gap nanotubes have van Hove singularities at typical energy scale $E_g$ ~ 30 meV, the small effective mass leads to reduced spectral weight of these singularities and, additionally, thermal smearing prevents their observation since $k_BT \sim E_g$. Therefore, we expect small band gap tubes to have a similar observable van Hove singularities spacing as metallic tubes.

d$\Delta V$, variation in tip voltage, is related to d$\mu$, variation in chemical potential of nanotube, by $\mathrm{d}\mu / e = C/(C + C_Q)\ \mathrm{d}\Delta V$ , with consideration of $C$ and $C_Q$ in series. So, for metallic tubes, voltage separation between successive peaks near Fermi level is given by $\Delta V = 2.16\,\mathrm{V}\,D^{-1}[\mathrm{nm}^{-1}]\,(C_Q + C)/C$ . On the other hand, for semiconducting tubes, when the chemical potential is in the gap, the electron gas is incompressible because there are not available states and then quantum capacitance becomes negligibly small compared to geometrical capacitance, $C_Q << C$ , so $\mu$/e and $\Delta V$ are related in a 1:1 ratio. The band gap $E_g$ then determines the voltage spacing between peaks, giving $V_g[\mathrm{V}] = E_g/e \approx 0.72\ D^{-1}$ [nm$^{-1}$]. The characteristic energy scale for semiconducting tubes is 3 times smaller than that for metallic ones, as explained in tight-binding calculation in introduction section.

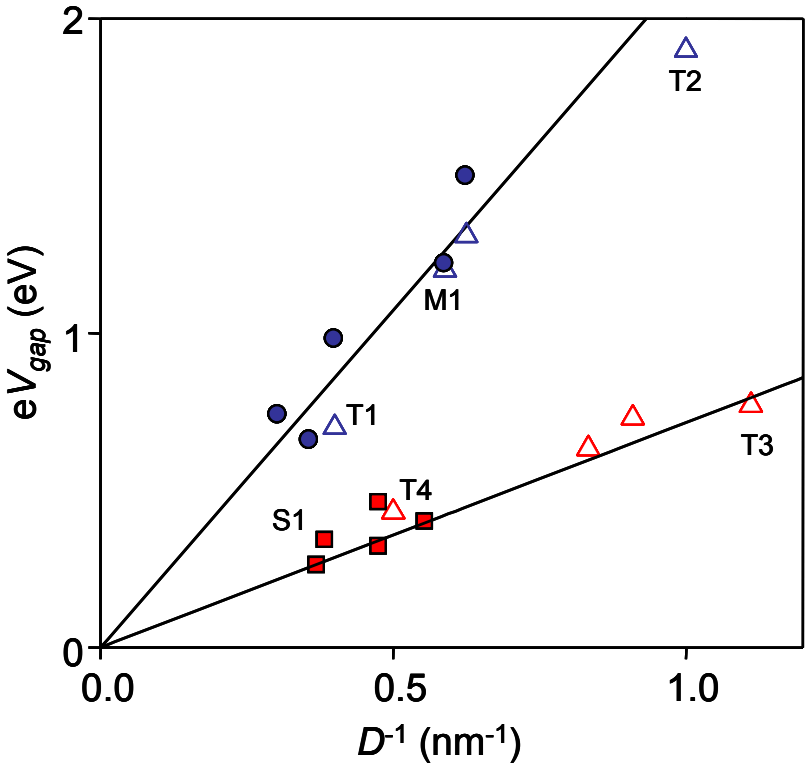


Figure I-22. Plot of e$V_g$ versus $D^{-1}$. Transport experiments were performed on some nanotubes to determine whether they were semiconducting or metallic. The squares show data from semiconducting nanotubes, falling on the lower line. The circles show data from metallic nanotubes, falling on the upper line. The upper line is a fit to the metallic tube data with a slope of 2.16 eV nm. The lower line is a line with a slope of 0.72 eV nm, plotted without free parameters. Open triangles denote e$V_{gap}$ versus $D^{-1}$ for eight samples that did not have attached electrodes.

Plotting $eV_g$ versus $D^{-1}$ in Figure I-22 shows that $eV_g$ generally increases with increasing $D^{-1}$, with most of the data falling on one of two clusters corresponding to $eV_g$, differing by a factor of 3 for a given diameter. For example, $eV_g$ for T1 is ~ 3 times larger than $eV_g$ for S1. The open triangles show data from tubes without attached electrodes. The solid squares show $eV_g$ versus $D^{-1}$ for semiconducting nanotubes (as determined from transport experiments), which fall in the lower cluster. Accordingly, all tubes with $eV_g$ falling on the

lower line are inferred to be semiconducting. The expected relation between $eV_g$ and $D^{-1}$ for semiconducting nanotubes, $eV_g[\mathrm{V}] = 0.72\ D^{-1}\ [\mathrm{nm}^{-1}]$, is plotted as the lower solid line in Figure I-22. The data indicated by squares and lower four open triangles follow this line very closely. We emphasize that *the lower line has no free parameters*.

The upper data set taken from the metallic nanotubes also follows a straight line. Fitting a line to obtain the slope gives $e\Delta V_g = 2.16\,e\mathrm{V}\,D^{-1}[\mathrm{nm}^{-1}]\,(C_Q + C)/C \approx 2.16\,e\mathrm{V}\ D^{-1}$. That implies $(C_Q + C) / C \approx 1.0$. The three remaining points marked by open triangles also fall near this upper line. Remarkably, this implies that $C << C_Q$ for metallic nanotubes, and $d\mu/e \approx d\Delta V$. We estimate $C$ as $C = 2\pi\epsilon\epsilon_0/\ln(1+2s/d)\ L$ (see Appendix A) where $\epsilon$ is the dielectric constant, $\epsilon_0$ is the permittivity of free space, $s$ is the tip-tube separation, and $d$ is the tube diameter. Taking $\epsilon$~1(free space), $s$ ~2 nm, and $d$ ~1 nm, then geometrical capacitance is less than the quantum capacitance, $C \sim 8\times10^{-17}$ F $L[\mu\mathrm{m}] < C_Q = 8e^2/hv_F \sim 4\times10^{-16}$ F $L[\mu\mathrm{m}]$ ($C_Q$ is obtained as $C_Q = e^2 \cdot 8/hv_F$ from Equation I.35). However, this estimate for geometrical capacitance neglects the presence of the water capillary that forms under ambient conditions between the tip and sample when their separation is less than a few nm, as occurs in this experiment[16-20] (Figure I-23).

Since water's dielectric constant is ~ 80, it can strongly modify $C_{ts}$ during the lowest part of the cantilever oscillation cycle when it approaches the surface and the capillary forms. With $\epsilon$ ~ 80, the previous estimate yields instead $C \sim 6\times10^{-15}$ F $L[\mu\mathrm{m}]$. Thus we expect to find features in $\Delta\phi$ versus $\Delta V$ consistent with $C >> C_Q$ and $d\mu/e \approx d\Delta V$, in agreement with the relation obtained from a fit to the data for metallic nanotubes.

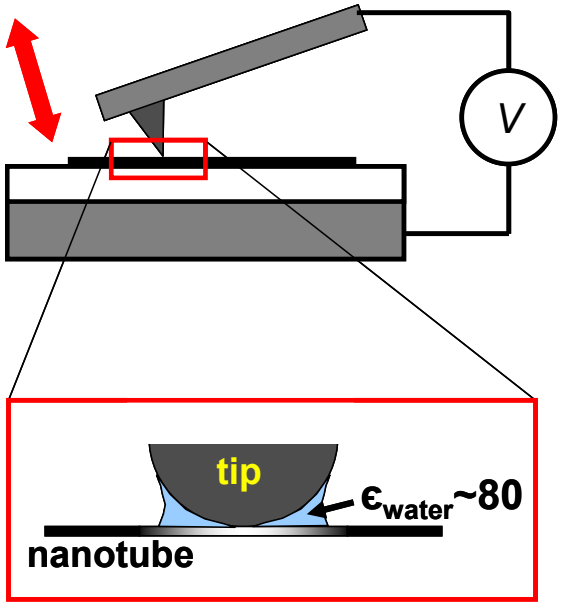


Figure I-23. Water meniscus formation between AFM tip and nanotube when its separation is less than a few nm during EFM experiment. Dielectric constant of water, $\epsilon_{water}$, is ~ 80, which makes geometric capacitance much larger than quantum capacitance, $C >> C_Q$.

This inference is further supported by periodic patterns of peak positions in $\Delta V$. For some nanotubes, particularly those with $D > \sim 2$ nm (when low-energy assumption can be applied, as in Section I-2-5), the peak arrangement in $\Delta V$ depends on whether they are metallic or semiconducting. For semiconducting tubes, the peaks cluster in groups of two, alternating between large intervals $\delta(\Delta V) \sim V_g$ and small intervals $\delta(\Delta V) \sim V_g/2$, as exemplified by S1. These intervals are plotted in Figure I-24(b) by filled squares. For metallic (or small band gap) tubes, there is one large interval of $\delta(\Delta V) = V_{gm}$ near $\Delta V = 0$, with the other intervals $\delta(\Delta V) \sim V_g/2$, as exemplified by T1. Filled squares in Figure I-24(a) denote these intervals from T1.

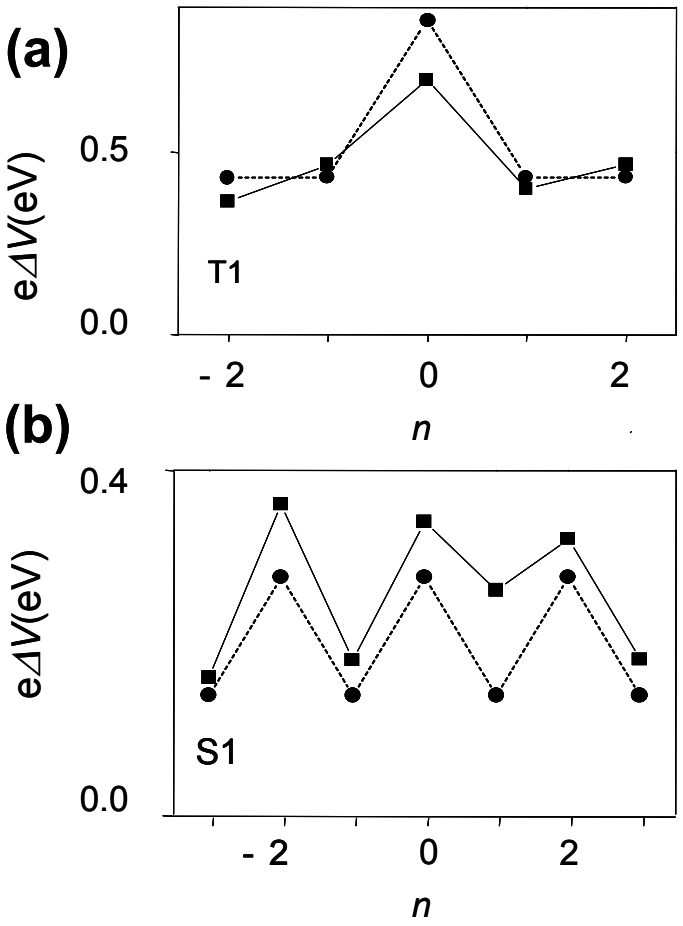


Figure I-24. Successive energy spacing in EFM data. (a) Data shows filled squares connected by solid lines denoting intervals between peaks for sample T1. The filled circles joined by dashed lines show the theoretical expectation. (b) Filled squares connected by solid lines denote intervals between peaks for sample S1. The filled circles joined by dashed lines show the theoretical expectation.

These patterns are readily accounted for by using a low-energy model (Figure I-11), which is expected to be accurate for nanotubes in the given size range.[21] In this picture, the energy spacing between successive van Hove singularities in semiconducting nanotubes is expected to alternate between $E_g$ and $E_g/2$, while metallic nanotubes are expected to have one large interval $E_{11}$, with the rest equal intervals of $E_{11}/2$, consistent with our

observations. The expected intervals, assuming $d\mu/e \approx d\Delta V$, are plotted as filled circles connected by dashed lines in Figure I-24(b) for S1 and for T1 in Figure I-24(a), using only the measured diameter of the nanotubes as the input parameter. These calculated intervals are in good agreement with the data.

This picture of meniscus formation and the resulting large geometric capacitance obtained accounts qualitatively for the peaks' presence, and quantitatively for the voltage gap $V_g$ for both metallic and semiconducting nanotubes *without free parameters*. Taken together, this demonstrates that atomic force microscopy can be used to probe the local density of states in nanotubes, yielding a spectroscopic technique in which $\mu$ is directly tuned by $V$ to yield a calibrated energy scale.

### I-6 Modulating Band Structure of Nanotubes by Strain Induced by AFM tip

To further demonstrate the capabilities of our EFM technique, we measured the local band gap of an artificially produced quantum well structure within a semiconducting nanotube. Longitudinal strain has been shown both theoretically[5-7](Section I-2-6) and experimentally[22,23] to modulate the band structure of nanotubes.

Figure I-25 shows AFM images of stretched nanotubes by an AFM tip. Nanotubes are located in the center of scan image, subsequently the tip moves according to scripts in loaded nanoscript. First, it goes to the center of scan, gently pushes the surface, and then, drags to the right. As a result, nanotubes are stretched. Figure I-25(a) and (c) show topographic images of stretched tubes, whereas (b), (d) correspond to EFM images of

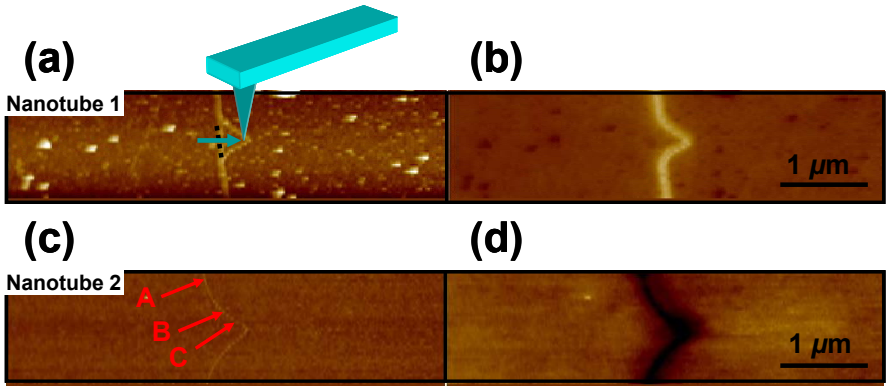


Figure I-25. Stretching nanotubes by AFM tip. Nanotubes are located in the center region of scan, and an AFM tip is moved to the center, gently pushed down into substrate and dragged to the right. Nanotubes are stretched as a result. (a), (b) correspond to nanotube 1 and (c), (d) to nanotube 2. (a) The topographic image of nanotube 1. The original position of nanotube 1 is indicated by dashed black line. Nanotube is dragged with AFM tip along blue arrow. (b) EFM image of nanotube 1, which clearly shows stretched nanotube as a result. The phase signal is inverted for better contrast to eye. (c) Another example of stretched nanotube. Three regions, marked by A, B, and C, have different local strain. Region A is unstrained. Strain on region C is larger than on region B, roughly estimating from the shape of the tube.

each nanotube. We check that the ends of nanotubes are not sliding, which could possibly cause the release of strain. Also, up to the resolution of AFM images, no broken section is observed. Previous experiment[24,25] supports that nanotubes under a few percent of strain are easily achieved without breaking it. In Figure I-25(c), three regions, A, B, and C are indicated by red arrows where region A is unstretched, while B is approximately where strain starts to be applied, and C is at maximum strain.

Figure I-26 shows that a nanotube is stretched similarly as Figure I-25, and also performed EFM. EFM data, $\Delta\phi$ versus $\Delta V$, are obtained on various locations (A, B, and C in Figure I-26(b) inset). We then probed the LDOS at those points. Point A is outside of the

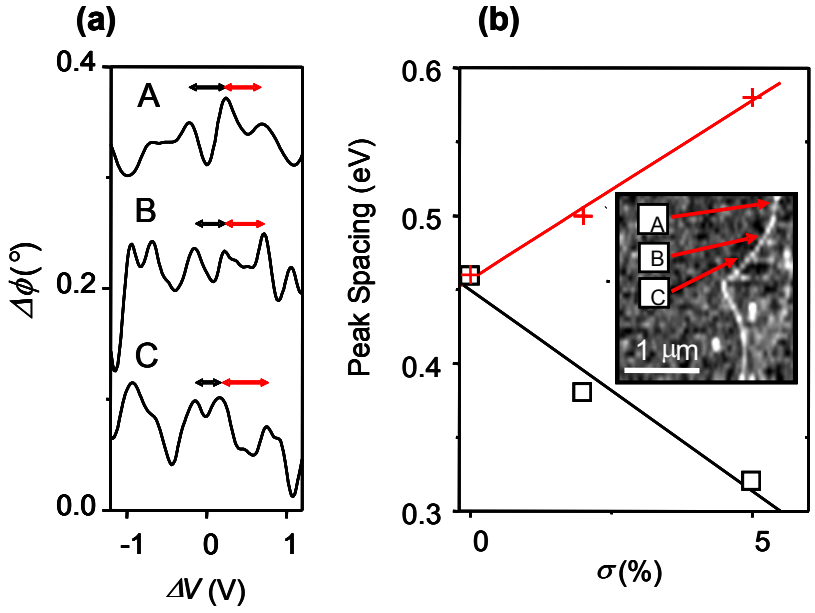


Figure I-26. Effect of nanotube strain on van Hove singularity positions. (a) Plot of $\Delta\phi$ versus $\Delta V$ for a strained nanotube taken at the positions A, B, and C indicated in the inset to part (b). Curves are offset for clarity. The arrows indicate two successive peak intervals for data taken from each location. Size of gap and measured tube diameter indicate that this tube is semiconducting. (b) Band gap (open squares) and second interval (crosses) versus estimated local strain

displaced region and yields an energy gap of 0.45 eV, corresponding to black arrow in A, Figure I-26(a). This is consistent with the expectation for the band gap of semiconducting nanotube with the measured diameter $D$ = 1.9 nm of 0.38 eV from low-energy model. From the shape of the tube, we estimate the local strain at point B and C to be ~ 2% and ~ 5%, respectively.[24] We note these estimates are only approximate, since the assumption that the strain is concentrated only in the displaced region may be oversimplified.[25]

Figure I-26(b) shows $eV_g$ versus $\sigma$ in the lower data set. We observe the shifting of van Hove singularities at chemical potentials further away from the Fermi level for a neutral tube. The upper set of data in Figure I-26(b) shows the energy gap between the first and

second van Hove singularities $eV_{g1}$. Fitting a straight line to the measured $eV_g$ versus $\sigma$ shows that the band gap diminishes by $dE_g/d\sigma \sim 24$ meV/% of strain, while $eV_{g1}$ increases by ~ 27 meV/% of strain. This is in qualitative agreement with theoretical predictions, which predict equal and opposite energy shifts for these gaps under strain (In Section I-2-6, two peaks observed here correspond to the closest and the second closest allowed vectors. Relative position of a new **K** point to two vectors should give the opposite energy shifts.) Quantitatively, $dE_g/d\sigma$ is expected to be $\approx 100\ meV \cos(3\theta)$, where $\theta$ is the chiral angle of the nanotube. $\theta = 0°$ for a zigzag nanotube, and $\theta = 30°$ for an armchair tube (Equation I.49). The chiral angle of the nanotube exhibited in Figure I-26 is then estimated as ~ 1/3 $\cos^{-1}$(24 meV/100 meV) ~ 25°.

The decrease of the band gap with strain constrains the chiral indices for a ($n$,$m$) nanotube to satisfy $n - m = 3q - 1$, where $n$, $m$, and $q$ are integers. This constraint, coupled with careful measurements of diameter and the strain-dependence of the gap, could enable the determination of the chiral indices for a given nanotube using only electrostatic forces and mechanical strain. Comparison of the present data with that of micro-Raman studies will be helpful in this regard and may help to ascertain the numerical accuracy of the theory of reference 7.

In conclusion, we have demonstrated that AFM can be used to probe the electronic density of states in carbon nanotubes and distinguish individual metallic and semiconducting nanotubes without using attached electrodes. This capability should prove useful in efforts to control nanotube synthesis or separation to yield selected electronic

properties. Finally, unlike scanning tunneling microscopy, our measurements can be readily performed on insulating substrates. Future work should enable detailed images of the local electronic structure of nanotubes or other nanomaterials to be directly compared to the results of further transport, optical, or sensing experiments.

## I-7 Appendix

### Geometrical capacitance estimation

With the relatively small diameter (~ 1−3 *nm*) of nanotubes compared to the radius of curvature of AFM tip (~ a few tens of *nm*), we can approximate an AFM tip as a plane near cylindrical nanotube (Figure I-27).

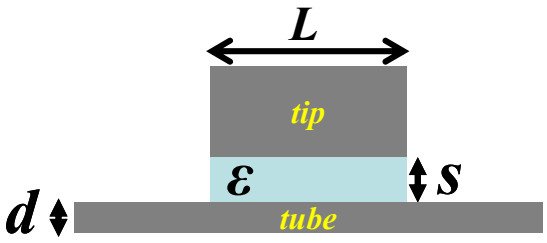


Figure I-27. Geometrical capacitance between AFM tip and nanotube

The electric field from a line of charge is given by

$$E = \frac{\lambda}{2\pi\varepsilon\varepsilon_0 r} \qquad \text{(A.1)}$$

where $\lambda$ is charge density, $\varepsilon$ is the dielectric constant for filling material between nanotube and tip surface, $\varepsilon_0$ is the dielectric constant in vacuum, and $r$ is the distance from the line. Then, the potential difference, $V$, between AFM tip plane and nanotube is

$$V = \int_d^s \frac{2\lambda}{2\pi\varepsilon\varepsilon_0 r} dr . \quad \text{(A.2)}$$

Using $Q=C_G V$, the geometrical capacitance, $C_G$ is

$$C_G = \frac{2\pi\varepsilon\varepsilon_0}{\ln(1+2s/d)} L \quad \text{(A.3)}$$

where $L$ is the effective length.

*Chapter II*

# INTERFEROMETRY BASED ON SINGLE-WALLED NANOTUBE LOOPS

## II.1 Abstract

Single-walled carbon nanotubes (SWNTs), which have micron-scale phase coherence lengths at low temperatures, are grown so that they cross over themselves, producing loops with single intertube junctions, which may act as interferometers. In order to determine the electron pathways at the junction, we performed scanned gate microscopy (SGM) using an Atomic Force Microscopy (AFM) tip as a local gate. If an SGM signal is observed when the tip is over any particular segment it indicates current flow in that segment. Surprisingly, one semiconducting tube showed that most electrons tunnel into the other segment at the junction without flowing through the loop. For other samples, however, current flow was observed in the loop. Taken together, this suggests the possibility of controlling tunneling probabilities at the junction. We used the scanned probe data to determine the junction and loop resistances, demonstrating that scanned probe techniques can be used to analyze the properties of complex nanoscale circuits. Moreover, for metallic or small bandgap nanotubes, we reproducibly observe unusual conductance oscillations with a number of periods as function of gate voltage. These oscillations persist up to temperatures ~ 50 K. We compare our results with a model[26] that accounts for the interference of counterpropagating electron waves around the loop, analogous to a Sagnac interferometer

in optics. In this model, the different velocities for right and left movers in the two carbon nanotube bands produce large energy scale interference oscillations. We find semi-quantitative agreement between our data and the theory. These results may enable phase coherence in nanotubes to be studied up to temperatures much higher than the cutoff imposed by thermal smearing.

## II-2 Growing Single-Walled Carbon Nanotube Loops

In order to obtain single-walled nanotube loops efficiently, growing ultra-long nanotubes is necessary. This in turn requires catalyst islands in order to elevate the growing nanotube away from the substrate.[27,28] Preparing catalyst islands requires one pre-growth lithographic step.

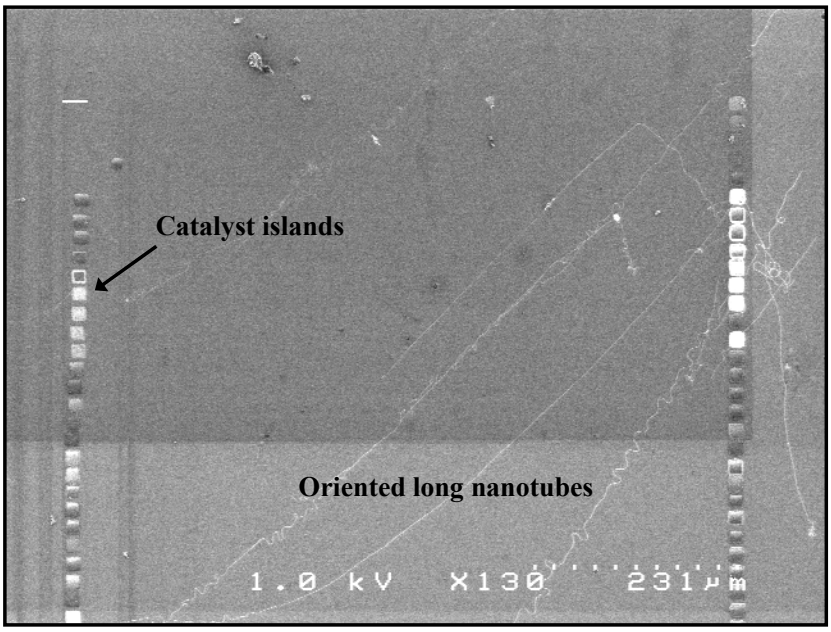


Figure II-1. Ultra-long nanotubes grown from catalyst islands.

The arrays of square catalyst islands (15×15 $\mu m^2$) shown in Figure II-1, are defined by electron beam lithography. Before the lift-off process, a few drops of catalyst solution are deposited and the sample is heated at 170ºC for 5 minutes. The catalyst solution is prepared as follows. Mixture of $Fe(NO_3)_3 \cdot 9H_2O$ (25 mg), Alumina nanopowder (25 mg) and $MoO_2(acac)_2$ (8 mg) (Aldrich) is stirred for 24 hours in 30 ml of methanol and sonicated for 1 hour before depositing. Lifting off the PMMA/MAA bi-layer leaves

catalyst particles only in designated square islands. Unlike the growth procedure discussed previously (Section I-3-1), we employ two important additional procedures, fast heating[29] and vertical sample positioning (Figure II-2). A special sample holder (quartz) is made to have samples

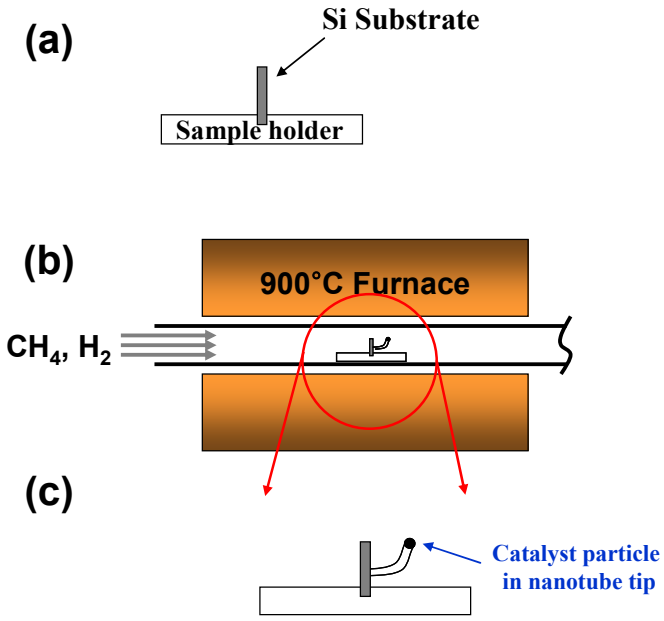


Figure II-2. Growing long tubes

in an upright position (Figure II-2(a)). The sample holder is introduced into 900ºC zone quickly in the furnace (fast heating) and a gas mixture of $H_2$ (200 sccm) and $CH_4$ (1000 sccm) is flowed (Figure II-2(b)).

The proposed 'Kite growth mechanism'[29] hypothesizes that when the sample is heated quickly, a catalyst particle in the nanotube tip with nanotube tail floats like a kite over the substrate (Figure II-2(c)) due to convection currents, and then becomes oriented by horizontal laminar flow of gas inside a quartz tube. During growth, the active ends of the

nanotubes were always floating while the sections close to the original sites where the catalyst was deposited likely adhere by van der Waals forces to the substrate. The nanotubes kept growing until they fell down onto the surface or until the deliberate termination of the carbon source. We used vertical sample positioning to increase the "floating" time. When falling down, nanotubes often formed wiggles or loops on the way (Figure II-3).

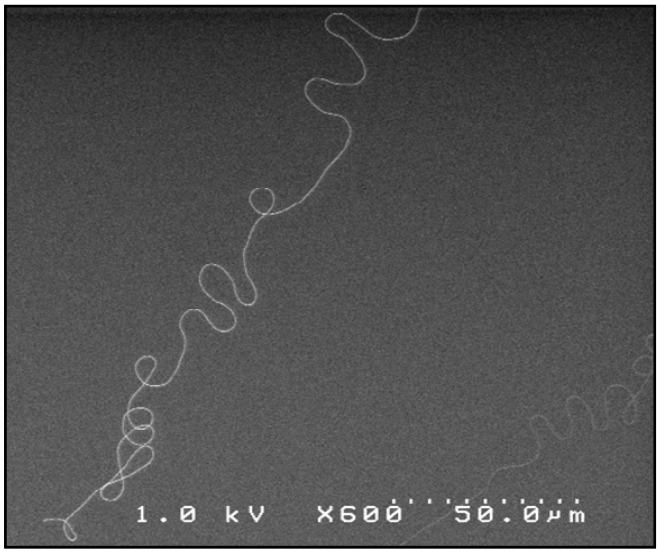


Figure II-3. Nanotube loops

**II-3 Nanotube Loop Device and Electron Pathway at the Junction**

A single-walled nanotube loop device is made after electron beam lithography, metal deposition and lift-off. Figure II-4(a) shows one of the nanotube loop devices contacted with metal on both ends. This device is ~ 50 μm long with a loop diameter of 7 μm. In Figure II-4(c), an electron can travel through the loop in continuous fashion (blue arrow), or

tunnel into the other segment at the junction (red arrow). In order to use a nanotube loop device as an interferometer, 50 percent of electron wave function splitting at the loop junction is optimal, but previous experimental study of crossed tubes[30] indicates that the transmission probability at the junction is at most 0.02 for metallic-metallic crossed tubes and smaller for semi-semi tubes. Although small, this is still larger than expected, consistent with theoretical work[31] that shows that structure deformation of tubes at the junction because of van der Waals force interaction with $SiO_2$ substrate occurs (Figure II-5(c)),

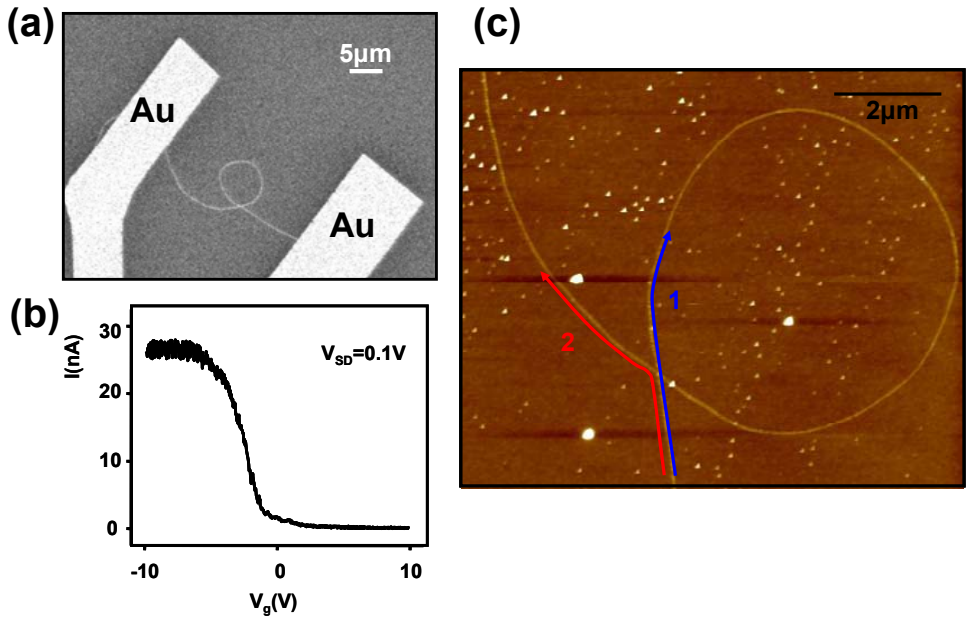


Figure II-4. Semiconducting nanotube loop device

enhancing the intertube tunneling probaility. As the intertube distance decreases, the dimensionless tunnel conductance increases up to 0.1 (for (5, 5) tube and 2.5 Å of intertube distance).

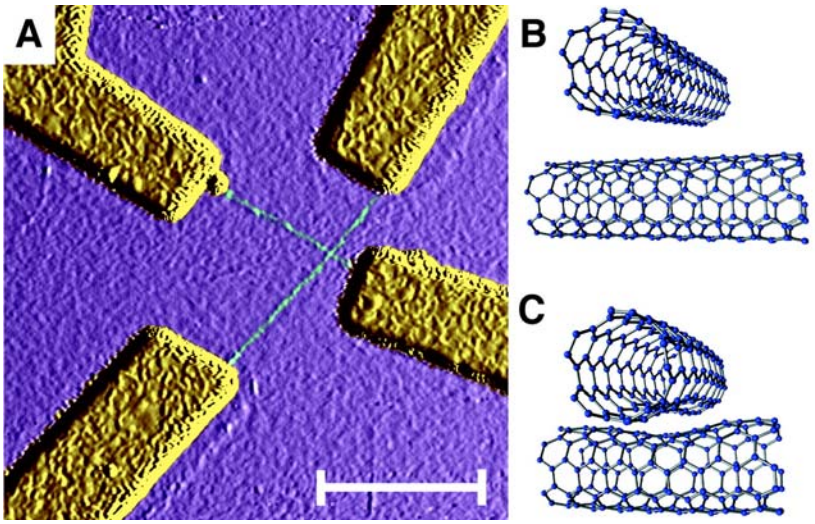


Figure II-5. Four terminal crossed tube device and structure deformation of crossed tubes at the junction (figure taken from reference [30])

In our nanotube loop device, measuring how much current flows through the loop will determine the transmission probabilities at the junction. This is realized for semiconducting loop devices utilizing Scannned Gate Microscopy (SGM).

## II-4 Scan Gate Microscopy of Semiconducting Carbon Nanotube Loops

Scan gate microscopy makes use of biased AFM tip as a local gate to change the local charge density within a sample. A material with a conductance sensitive to its charge density like a semiconducting nanotube can be locally depleted of charge, which reduces the current through it. By plotting the current through the device versus the tip position an image of how the tip perturbation affects the sample is obtained. It has been largely used to locate defects[14,32] or artificially manipulate gate sensitive regions.[33]

Figure II-6(a) shows the experimental set-up for SGM. While applying a source-drain voltage, $V$ between two electrodes on the substrate, the sample is scanned first to obtain a topographic image and second with the biased ($V_G$) AFM tip. With the height information from the topographic scan (Figure II-6(c) upper left), the biased AFM tip is lifted ~ 10-20nm from the sample and scanned with zero vibration amplitude in second path. The current through the device is recorded as function of tip location (Figure II-6(c) upper right). Knowing that this specific tube is p-type semiconducting tube based on the $I$-$V_g$ data In Figure II-4(b), by applying positive gate voltage, the local Fermi level of the nanotube is shifted to be in the band gap region (dotted line in Figure II-6(b)), which acts as a local barrier resulting in current suppression. Figure II-6(c) upper right is color scale data of current where on-current corresponding to the bright background is around ~ 0.3 μA, while the dark region corresponds to current suppression. A series of darker points (spaced by a few hundreds of nanometers) along the nanotube is observed. These points likely correspond to places where the local electron density is minimal or strong tunnel barriers exist. The microscopic origin of these scattering sites is not clear, but could correspond to localized defects in the tube or to long-range electrostatic potential fluctuations associated with localized charges or surface contaminants.[34] But, surprisingly, none of these localized sites are observable, or indeed is any current suppression on the loop segment of the tube, indicating that the current flow is almost entirely through the junction. This is quite remarkable in light of the few percent of tunneling probability in previous studies.[30,31] To further investigate this behavior, the global back gate voltage is varied.

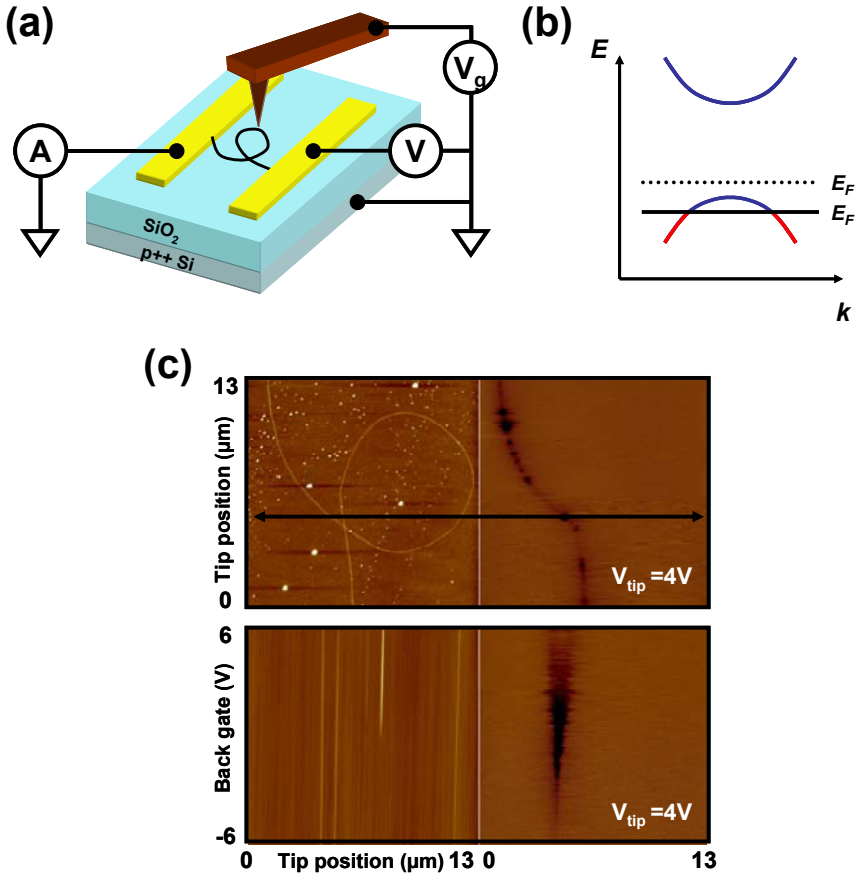


Figure II-6. Scan gate microscopy of nanotube loop device shown in Figure II-9

The Figure II-6(c) lower panel shows a slow-axis-disabled scan along the black arrow in upper panel. The back gate voltage is incremented from -6 *V* to 6 *V* after each scan along the vertical axis. The three vertical lines in the left image indicate three segments on the nanotube with two on the right-hand side corresponding to the loop. Only current suppression on the leftmost segment is observed, which implies no current flowing on the loop due to nearly 100% of tunneling at the junction. Also the current signal as a function of back gate voltage on the other segment is expected. From the bottom, at high negative back gate voltage ($\sim -6$ *V*), 4 *V* of local gate is not enough to turn off the device, so the

current signal is similar to background. But as the back gate voltage goes more to the positive side, current suppression by the local gate starts to appear and gradually increases. Last, when high positive back gate turns off the device, the effect of current suppression is diminished, giving essentially only the background signal at ~ 6 V. The origin of the dominance of tunneling at the loop junction is not known. But, further analysis will be discussed below.

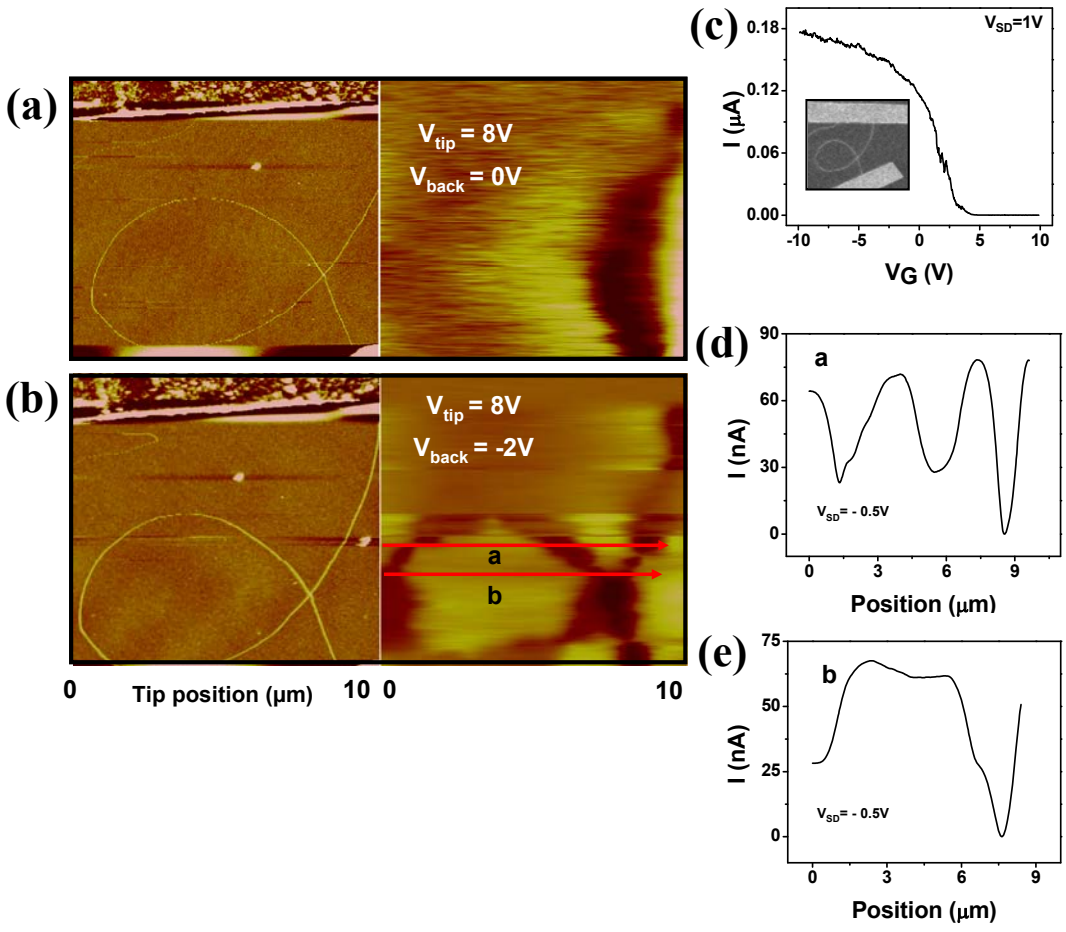


Figure II-7. Changing the current path with back gate voltage

Figure II-7(a) shows another semiconducting loop device (the assignment of semiconducting character is based on the $I$-$V_g$ data in Figure II-7(c)). SGM on this device (right image) indicates that current flow avoids the loop similarly to the device presented in Figure II-6. But, remarkably, when a moderate negative back gate voltage ($\sim -2$ $V$) is applied, current flow on the loop segment is also observed (Figure II-7(b)). Taking line traces along red arrows in Figure II-7(b), we notice that the current drop on the loop segment is around a half of the drop on the other segment (Figure II-7(c) and (d)). Assuming high local gate ($\sim 8$ $V$) completely turns off the device, the drop on each segment corresponds to local current flow, giving half of the total current flowing on the loop.

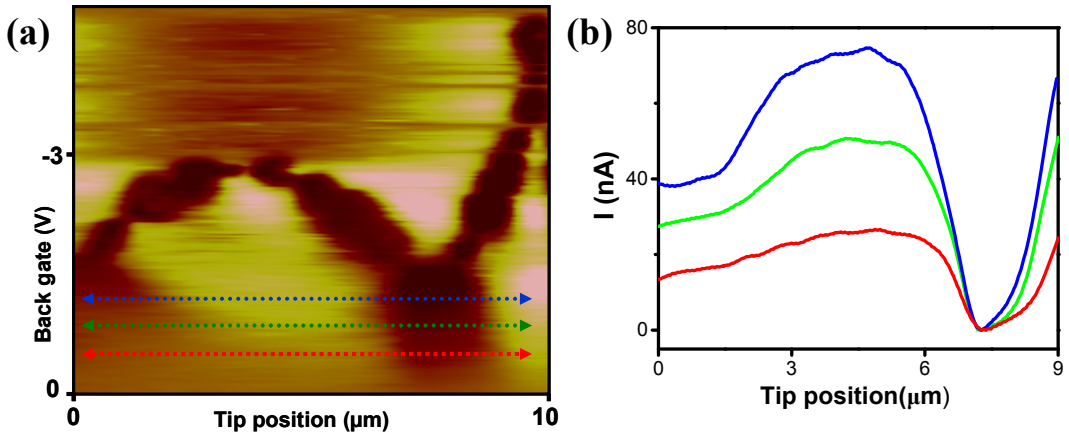


Figure II-8. Controlling current splitting with back gate voltage

This current sharing can be tuned with back gate voltage. In Figure II-8(a), SGM data is obtained as the back gate voltage is varied from 0 $V$ to -3 $V$ in vertical axis. Current is not going through the loop near 0 $V$ as no apparent image of the loop is shown (compare this

to Figure II-7(b) where a constant current signal on the loop is observed when the back gate voltage is kept the same through the scan), but it starts to appear as back gate voltage decreases, resulting in current splitting at the junction. Line traces taken along the dotted line in Figure II-8(a) are shown in Figure II-8(b). The ratio of loop current to total current is increased from the red to the green curve and from the green to the blue with the increase of global current. That is because the loop resistance drops so that more current will flow through it.

A nanotube loop device with this controllable splitting would be a potential candidate as an interferometer when the phase coherent length is comparable to device length at low temperature.

Figure II-9 shows another nanotube loop device, where we can also change current path with back gate voltage. The loop segment carries a current flow (Figure II-9(c)) or not (Figure II-9(b)), depending on back gate voltage. A negative back gate voltage, -2 *V*, causes the loop segment to carry ~ 10% of the total current, judging from the line trace of SGM data taken along the dotted line in Figure II-9(c) (Figure II-9(e)). To further analyze the device, we performed DC electrostatic force microscopy (DC EFM) (Figure II-9(d)). This measurement yields a signal showing how the local electric potential varies as a function of AFM tip position. In our case, because of the insulating substrate, a potential variation along the nanotube device would be observed. The experimental setup is similar to EFM in Section I-5 and is as follows: While applying source-drain voltage on a device, a biased AFM tip scans the sample. During the DC EFM scan, the phase shift between

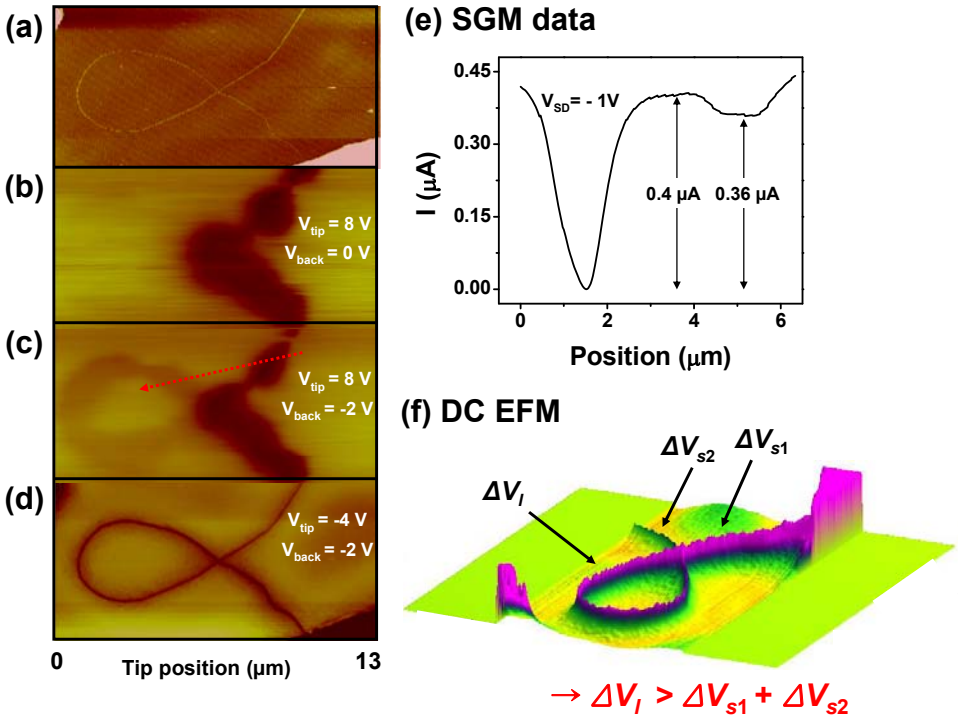


Figure II-9. SGM and DC EFM on nanotube loop device. (a) Topographic image of device. (b) SGM scan at $0V$ back gate voltage shows no current flow in the loop. (c) More negative back gate voltage gives current sharing with the loop. Faint image of loop appears. (d) DC EFM measurement shows how surface potential varies along the device. (e) Line trace taken along red dotted line in (c). Loop segment carries ~ 10% of total current. (f) 3D plot of DC EFM in (d). Electric potential drop on loop segment is larger than the sum of the others.

the mechanical drive near the tip resonant frequency and the measured tip motion with electrostatic force is recorded. As discussed in Section I-5, this phase shift is proportional to the potential difference squared, $\Delta\phi \propto dF/dz \propto -(d^2C_{TS}/dz^2)\,\Delta V^2$ , where $\Delta V = (V + \varphi - V_S)$, $V$ is tip bias voltage, $C_{TS}$ is tip-sample capacitance, $\varphi$ is the work function difference between tip and sample, and $V_S$ is the local voltage within the sample. At a constant tip-sample work function difference and tip voltage, the phase signal is proportional to the local potential squared. From the 3D DC EFM data plot in Figure II-9(f), we immediately notice that potential drop on the loop segment is larger than the sum of the

drops on the others (we apply a negative back gate voltage to operate the device in current sharing regime like Figure II-9(c)). Treating this nanotube device as a diffusive conductor, it means the loop segment is more resistive than the others. For a quantitative investigation, we model our system as in Figure II-10(b).

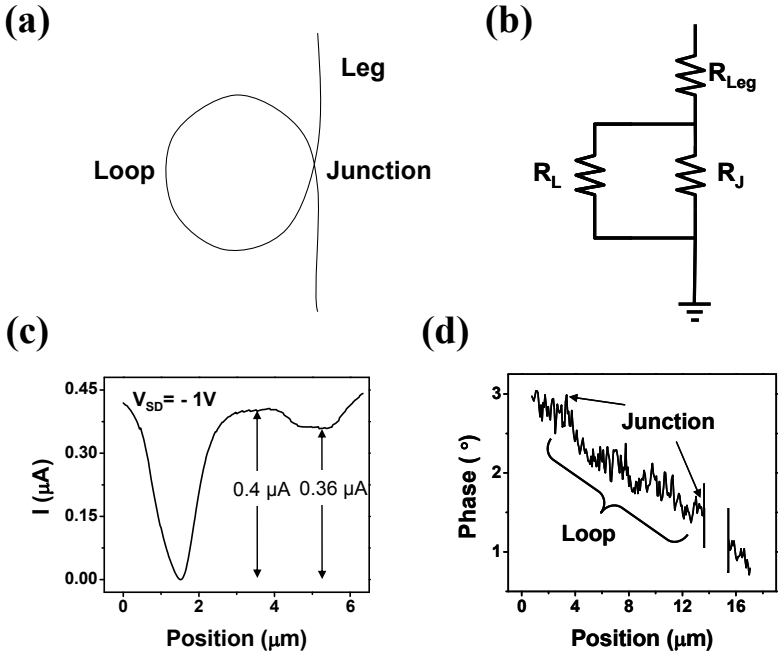


Figure II-10. Resistive circuit model. (a) Diagram of a nanotube loop device. (b) Resistive circuit model of loop device. Three segments, loop, junction, and leg, correspond to three resistors with resistance, $R_L$, $R_J$, and $R_{Leg}$, respectively. (c) Line trace of SGM data (the same as Figure II-14(e)). (d) Phase signal in DC EFM data (Figure II-9(d)) extracted along the device

From the schematic drawing of the loop device (Figure II-10(a)) with three segments, loop, junction, and leg, resistors corresponding to each segment are shown with their corresponding resistances, $R_L$, $R_J$, and $R_{Leg}$. From DC EFM data taken along the device

(Figure II-10(d)) together with SGM data (Figure II-10(c)), we can solve for the three unknown resistance values from three equations. From Ohm's law,

$$\begin{aligned} R_{Leg} + \left( \frac{1}{R_L} + \frac{1}{R_J} \right)^{-1} &= \frac{V}{I_{Leg}} \\ R_J I_J &= R_L I_L \qquad \text{(II.1)} \\ \frac{R_L I_L}{R_{Leg} I_{Leg} + R_L I_L} &= \frac{\Delta V_L}{\Delta V} \end{aligned}$$

where $V$ is source-drain bias voltage in SGM data, $I_L$ is current flowing through the loop segment $I_J$ is current flowing through the junction, $I_{Leg}$ is total current, $\Delta V$ is total potential drop along the device, and $\Delta V_L$ is potential drop along the loop. Using the measured values $V$= 1 V, $I_L$= 0.04 μA, $I_{Leg}$= 0.4 μA, $I_J$= 0.36 μA, and $\Delta V / \Delta V_L$ = 14/24, give

$$\begin{aligned} R_L &\approx 14\,\text{M}\Omega \\ R_J &\approx 1.6\,\text{M}\Omega \qquad \text{(II.2)} \\ R_{Leg} &\approx 1\,\text{M}\Omega \ . \end{aligned}$$

As expected, $R_L$ is one order of magnitude higher than the others, allowing only 10% of total current to flow through the loop segment. This difference may result from the fact that nanotube loops can act as "charge corrals" so that the loop is effectively more depleted than the linear segments.[35]

**II-5 Transport Measurement of Metallic Carbon Nanotube Loops**

Two metallic loop devices, A and B, are made from an identical ~ 100 micron long nanotube (Figure II-11(a)). The circumferential length of loops is ~ 10 microns, while

total device length is around 20 microns. The room temperature resistance from linear *I-V* was ~ 100 kΩ for both devices.

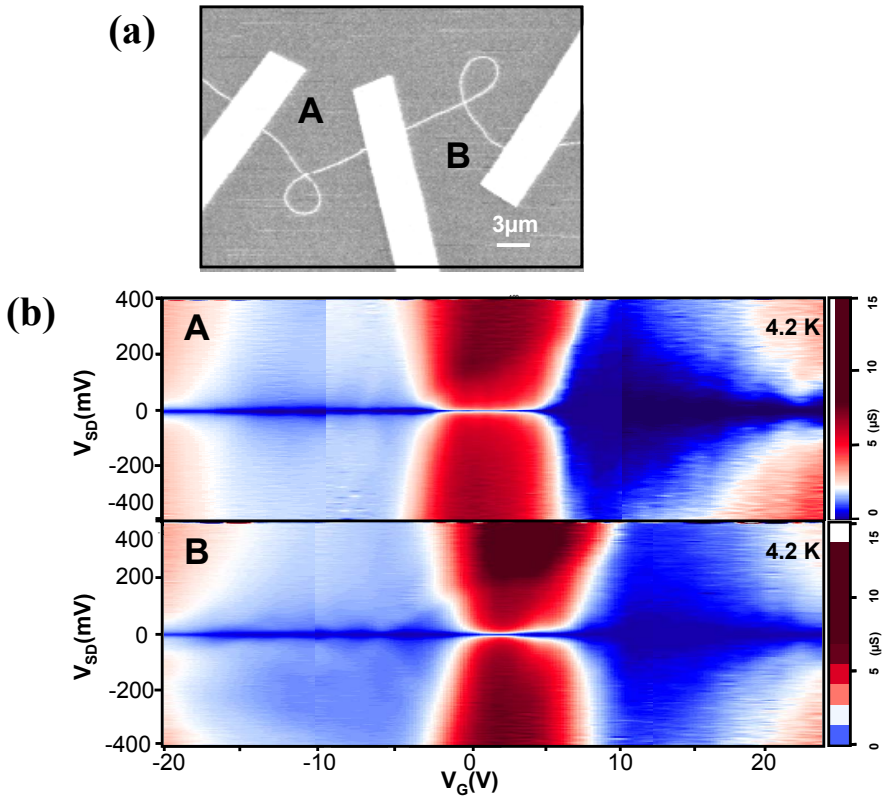


Figure II-11. Transport measurement of two metallic loop devices made from an identical ~ 100 micron long nanotube. (a) SEM image of devices, A and B. (b) Color scale plot of conductance (red means high conductance) versus source-drain bias voltage, $V_{SD}$ and back gate voltage, $V_G$

A color scale plot of differential conductance versus source-drain bias voltage, $V_{SD}$ and back gate voltage, $V_G$, taken at 4.2 K, is shown in Figure II-11(b). An unusual broad conductance peak (with its width ~ 10 V) around zero gate voltage is observed in two different samples (Note the strong similarity between the two data sets). Those broad peaks

are not reported as seen in any other nanotube devices before. In order to explore this phenomenon further, we take line traces of differential conductance at zero bias with various temperatures.

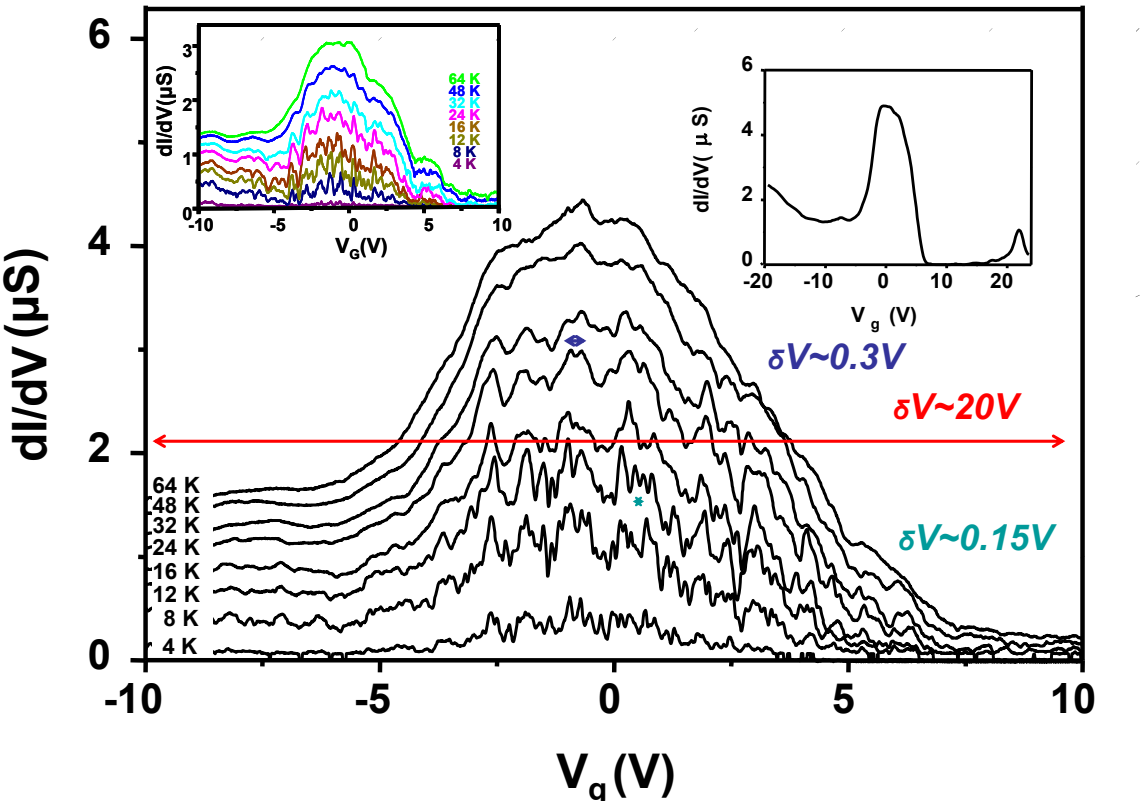


Figure II-12. Differential conductance at zero bias

Figure II-12 shows the zero-bias differential conductance versus back gate voltage taken at temperatures from 4K to 64K (from the bottom to the top) of device *A* in Figure II-11 (Device *B* also shows very similar behavior in the left inset, so from this point on we will concentrate on device *A* ). In the right inset, the differential conductance is measured over a larger gate voltage range, indicating that other peaks start to show up

beyond ± 20 V. The central peak has energy scale of 20 V in gate voltage, persisting up to 64K. Upon this large envelope, small-period wiggles start to appear as the temperature decreases. For example, ~ 0.3 V period oscillations (blue arrow) at 32K and ~ 0.15 V (light blue arrow) at 12K are observed. This whole variety of conductance oscillation patterns motivated us to start thinking about the possibility that a nanotube loop could give a realization of electronic equivalent to a Sagnac interferometer.[26]

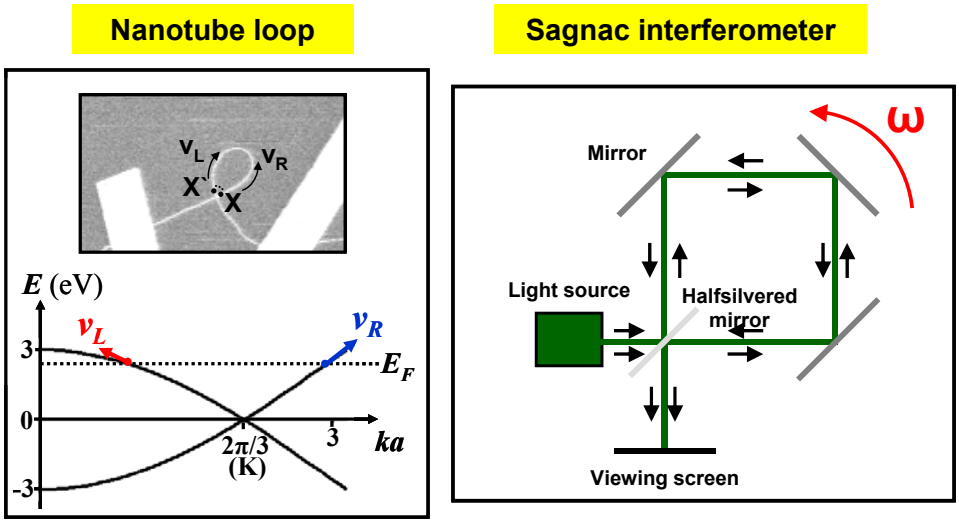


Figure II-13. Analogy of nanotube loop to Sagnac interferometer

A schematic diagram of a Sagnac interferometer is shown in the Figure II-13 right panel. Monochromatic light from source is split at a half-silvered mirror into clockwise and counterclockwise directions. Then, an interference pattern is projected onto a viewing screen. As the whole system rotates with a given angular velocity, in one direction light traverses a shortening path distance, while in the other it traverses a lengthening distance This results in a position change of interference fringes. Analogously, in our loop device, upon tunneling of electron at loop junction (X' ↔ X in Figure II-13 left), two

wavefunction components of a coherent electron moving opposite directions can interfere to give conductance oscillations (Fabry-Perot type). But because of the inherent asymmetry in the dispersion relation of the nanotube about **K** point (lower left in Figure II-13), a velocity difference between left moving and right moving electrons occurs. In other words, the role of the angular velocity for the light interferometer is replaced with a velocity difference for two counter propagating electron wavefunctions that arise from the nanotube band structure. Conductance fluctuations due to this velocity difference are expected on top of Fabry-Perot oscillations. Note that unlike Fabry-Perot interference, in which the interfering electrons traverse a different physical distance (a different number of times of the loop), interference due to a velocity difference is between two electrons traversing exactly the same distance.

Below we will estimate the relative energy scales of these interferences from tight binding theory and compare it to experimental data, although complete confirmation that the observed features result from Sagnac interference requires further experiments and analysis.

**Velocity difference**

The velocity difference occurs because the dispersion relation of metallic nanotubes deviates from the low-energy linear relation approximation. For armchair tubes, remembering the armchair energy dispersion relation from Equation I.26 and considering the lowest conduction band and highest valence band, we have

$$E_{1D,arm}(k) = \pm\, t\left|1 - 2\cos\left(\frac{ka}{2}\right)\right| \qquad \text{(II.3)}$$

where $t$ is the transfer integral and $a$ is the magnitude of the lattice vector in graphene. Expanding Equation II.3 around the **K** point ($ka$ = 2π/3) to the second order, energy dispersion becomes

$$\pm E = \hbar v_F k' + \frac{(\hbar v_F)^2}{6t} k'^2 \qquad \text{(II.4)}$$

where $k'$ is relative to **K** point and $v_F = \frac{\sqrt{3}}{2\hbar} ta$ . Then the magnitude of the velocities of the right and left movers are given by

$$v_{R,L} = \frac{1}{\hbar}\frac{\partial E}{\partial k'} = v_F \pm \frac{\hbar v_F k'}{3t} v_F . \qquad \text{(II.5)}$$

Rewriting Equation II.5 by introducing the velocity deviation, $u$, gives

$$\begin{aligned} v_R &= v_F + u \\ v_L &= v_F - u \\ \text{where } \; u &= \frac{\hbar v_F k'}{3t} v_F \approx \frac{E}{3t} v_F . \end{aligned} \qquad \text{(II.6)}$$

Note that the deviation depends on the Fermi energy relative to the Dirac point. Finally, energy dispersion near the Fermi level can be written as

$$E = \hbar v_{R,L} k_{R,L} \qquad \text{(II.7)}$$

where $k_{R,L}$ is wavevector for right and left movers.

**Relative Energy Scale**

The infinitesimal phase difference between right and left movers is given by

$$d(\Delta\phi) = L(dk_L - dk_R) = L\left(\frac{dE}{\hbar v_L} - \frac{dE}{\hbar v_R}\right) \approx \frac{L\,dE}{\hbar}\frac{2u}{v_F^2} = \frac{L}{\hbar v_F}\frac{2E}{3t}dE \qquad \text{(II.8)}$$

using Equation II.6 and II.7, where $L$ is the length of the loop. The first fringe due to the velocity-difference-induced interference (which we call Sagnac interference) appears when the accumulated phase difference between left and right movers becomes π,

$$\Delta\phi = \int_0^{E_{SAG}} \frac{L}{\hbar v_F}\frac{2E}{3t}\,dE = \frac{L}{\hbar v_F}\frac{E_{SAG}^2}{3t} = \pi \qquad \text{(II.9)}$$

where $E_{SAG}$ is the characteristic energy scale to obtain the first fringe of the interference.

On the other hand, the infinitesimal phase difference for Fabry-Perot interference for Feynman paths in which the electron travels back and forth around the loop (without considering the velocity difference), is

$$d(\Delta\phi) = 2L(dk) = \frac{2L}{\hbar v_F}dE\,. \qquad \text{(II.10)}$$

Then, the first fringe appears when

$$\Delta\phi = \int_0^{E_{FP}} \frac{2L}{\hbar v_F} dE = \frac{2L}{\hbar v_F} E_{FP} = \pi . \quad \text{(II.11)}$$

The Fermi energy of the nanotube is changed by back gate voltage multiplied by a conversion factor $\alpha$ (on the order of $10^{-2}$ in our system),

$$E = \alpha e V_G . \quad \text{(II.12)}$$

The relative energy scale (ratio of back gate voltage) is estimated using Equation II.9, II.11, and II.12,

$$\frac{E_{SAG}}{E_{FP}} = \frac{V_{G,SAG}}{V_{G,FP}} = \frac{\sqrt{3\pi t(\hbar v_F / L)}}{\pi(\hbar v_F / 2L)} . \quad \text{(II.13)}$$

Plugging in known values, $t \sim 2.5$ eV, $L \sim 10$ μm, and $v_F \sim 8\times10^5$ m/s,

$$\frac{V_{G,SAG}}{V_{G,FP}} \sim 400 . \quad \text{(II.14)}$$

**Comparing with experimental data and predictions from theory**

Assuming that slow ($\delta V \sim 20$ V) and fast ($\delta V \sim 0.5$ V) oscillations observed in our experimental data (Figure II-12) correspond to Sagnac and Febry-Perot interference,

$$\left(\frac{V_{G,SAG}}{V_{G,FP}}\right)_{\text{EXP}} \sim 130 , \quad \text{(II.15)}$$

which agrees with the estimation up to a factor of 3. A small velocity difference causes a large energy scale of Sagnac interference pattern, which is expected to survive above 60K. The theory also implies that the $n$-th fringe appears at $V_G \propto \sqrt{n}$ , because interference fringes repeat when $\Delta\phi = 2\pi n$ and $u \propto V_G$ from Equation II.6 and II.12. That is, fringes become denser in gate voltage as the Fermi level of the nanotube moves away from **K** point. Referring to our paper[26], conductance oscillations in source-drain voltage, $V_{SD}$ are also predicted, with their period depending on the velocities of the non-equilibrium hydrodynamic modes. Further experimental work is required to validate these theoretical predictions.

### II-6 Future Work

In addition to a Sagnac interferometer, we can think of loop device as an Aharonov-Bohm interferometer.[36]

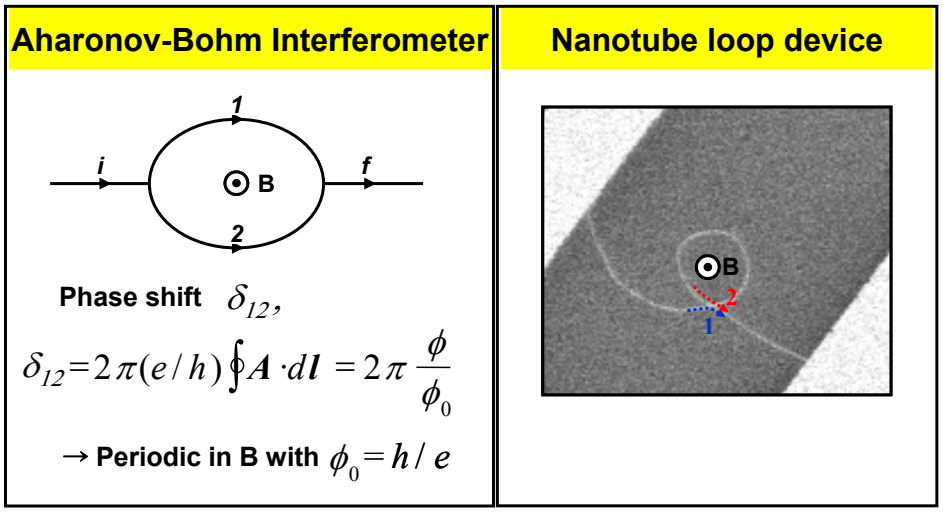


Figure II-14. Nanotube loop device as Aharonov-Bohm interferometer

In Figure II-14 left, the incoming electron wavefunction is split into two arms (1 and 2) and the two split wavefunctions interfere each other at the outgoing point. When a magnetic vector potential is present within the area enclosed by the two arms, the phase shift between two wavefunctions is given by $\delta_{12}$. The phase shift is proportional to the line integral of the magnetic vector potential around the enclosed loop, which is proportional to the magnetic flux through the loop. An Aharonov-Bohm interferometer may be realized with our loop device. On the right image, upon tunneling of an electron at the loop junction, for example, the tunneled electron (blue arrow) and loop-traveled electron (red arrow) would interfere with phase shift induced by applied magnetic field perpendicular to our device. The first fringe caused by Aharonov-Bohm interference is expected to appear at 2 Gauss for 10 $\mu m^2$ of loop area, which is very feasible in an experiment, provided the electronic path can be equalized between the junction and loop.

**II-7 Summary**

Using catalyst islands, which immobilize catalyst particles in certain areas on an otherwise clean substrate, enables us to specify where tubes are grown from. Long single-walled carbon nanotubes are grown to form loops. To facilitate loop formation, we employ two additional procedures, fast heating and vertical sample positioning, which help to grow long tubes according to the proposed kite mechanism. The loop size varies from ~ 3 $\mu m^2$ to ~ 100 $\mu m^2$. Placing contacting electrodes on individual nanotube loops and measuring $I$-$V_g$ curves yield both semiconducting and metallic loop devices. To utilize nanotube loop devices as interferometers, current paths are determined at the

crossing junction using SGM, where an AFM tip acts as a local gate to change the local charge density of semiconducting nanotube loop devices. In contrast to previous experiments we can tune the current splitting between the junction and the loop by changing the back gate voltage. With SGM and DC EFM, which gives information of how the potential changes along the loop device, we could estimate resistance of loop, junction and leg segment of device in the diffusive transport regime.

In addition, two relatively low resistance (~ 100 kΩ) metallic loop devices were made from a 100 μm long nantoube and both showed an unusual conductance peak around 0 V of back gate voltage. Various temperature scans of zero-bias differential conductance are performed to show a large scale peak having the width of ~ 20 V in gate voltage, which persists up to 64K. At lower temperatures, fast oscillations (~ 0.3 V and ~ 0.15 V) are observed. As a hypothesis, the proposed Sagnac interference model for nanotube loop devices is applied, from which velocity difference between left and right moving electrons are calculated and therefore the characteristic energy scale of the velocity-difference-induced interference. The estimated ratio of the energy scale of Sagnac interference to that of Fabry-Perot interference agrees with the experimental data to within a factor of 3. Predictions from the Sagnac interference model and the intriguing potential observability of Aharonov-Bohm interference stimulate further experimental investigation.

*Chapter III*

# SYNTHESIS OF COBALT-FILLED MULTI-WALLED CARBON NANOTUBES AND THEIR MAGNETORESISTANCE

## III-1 Abstract

Cobalt-filled multi-walled nanotubes are synthesized by chemical vapor deposition.[37] Cobalt nanoclusters larger than 100 nm are found in most closed nanotube tips and discontinuous cobalt nanowires (a few hundreds of nanometers long) are filled inside multi-walled nanotubes. X-ray diffraction spectroscopy of as-prepared material, following treatment of HCl, reveals encapsulated cobalt (face-centered cubic) nanowires in multi-walled carbon nanotubes, which is further verified by energy dispersive X-ray spectra analysis incorporated in scanning electron microscopy. A growth mechanism is proposed based on TEM images of individual cobalt-filled nanotubes. Co-filled nanotubes are metal-contacted to perform transport measurements. Current driven annealing usually gives less than 100 kΩ of two-terminal resistance at room temperature and one sample showed 2% of magnetoresistance switching around ±0.7 T at 1.4K. Directions for future work will be discussed.

## III-2 Motivation

Electrons have an intrinsic spin, and in solids the spin can be controlled and directed by applied electric or magnetic fields. Spin-electronics (spintronics) is a continuing area of exploration[38] motivated in large part by a search for an alternative to charge-based electronic devices to yield devices with novel functionality and properties. Carbon nanotubes are a promising material for nanoscale electronics that have dimensions < 10 nm. They also have an exceptionally long spin coherence length that may be exploited for spintronics[39-42]. However, optimal device operation would require that the nanotube itself be spin polarized. Such spin polarization has been predicted to occur in carbon nanotubes filled with ferromagnetic materials such as transition metals[43,44], however, these predictions have not yet been tested experimentally. This motivated us to synthesize cobalt-filled nanotubes and study their magnetoresistance, with the goal of eventually studying filled nanotubes in a crossbar geometry to engineer nanometer scale spin valves.

## III-3 Growth of Cobalt-Filled Multi-Walled Carbon Nanotubes

A previously reported recipe[37] to produce cobalt-filled multi-walled carbon nanotubes is used. A 2 mL stainless sample vessel (Swagelok) (Figure III-1(a)) containing 400 mg of magnesium powder and 700 mg of $Co(CO)_3NO$ is prepared. Because $Co(CO)_3NO$ is air-sensitive material, the sample vessel is immediately closed tightly after the introduction of the reagent. Heating the vessel inside a furnace at 900ºC produces black soot-like material. The product possibly contains remaining Mg and Co, so it is treated with 100 ml 8M HCL at 70ºC for 1 hour and then left overnight at room temperature.

After washing with DI water and filtering, the final product is obtained (Figure III-1(b)). The powder is characterized by X-ray diffraction spectroscopy (Figure III-2) and also ultrasonically dispersed in dichloroethane to deposit on silicon wafers and TEM grids for imaging and further analysis of individual Co-filled nanotubes. During the dispersion of powder

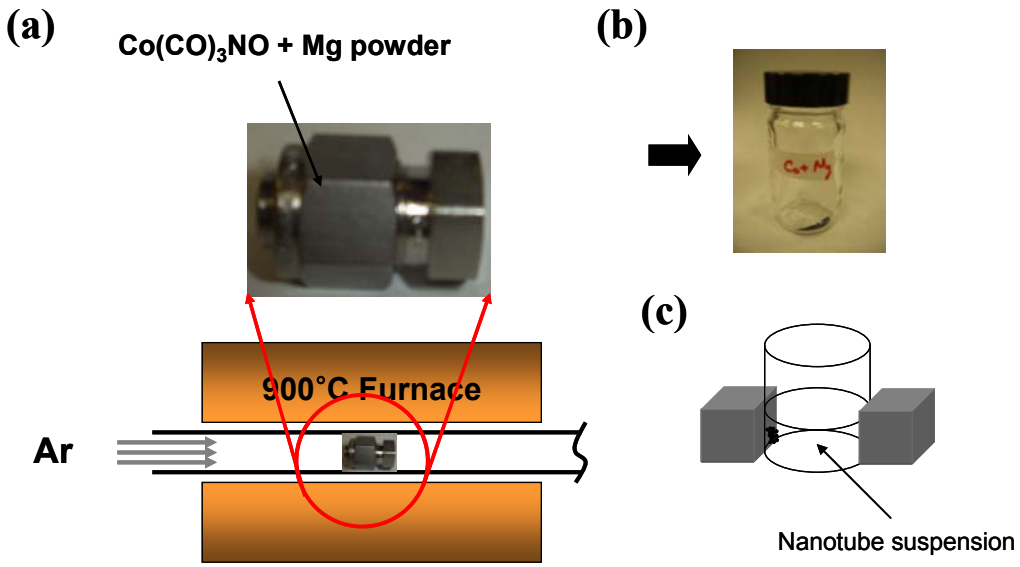


Figure III-1. Synthesis of Co-filled nanotubes

in dichloroethane, strong magnets are attached outside a beaker (Figure III-1(c)) in order to collect Co-filled nanotubes. The collected darker solution is diluted again and sonicated for a few hours before deposition.

Figure III-2 shows X-ray diffraction spectroscopy of various powder samples. In (a), spectroscopy data from background (green), and single-walled nanotube powder

(CoMoCat$^{TM}$ purified single-walled nanotubes) (black and red) is obtained for reference. The peak near 45 degrees from the single-walled nanotube powder (black and red) likely arises from residual catalyst particles in the nanotube soot. Blue and cyan data corresponding to different preparation techniques for Co-filled nanotubes show several peaks at the same positions, indicating similar products made from the two different recipes. Recipe 1 (blue) is explained earlier in this section as the pyrolysis of $Co(CO)_3NO$ in the presence of Mg powder. In recipe 2 (light blue), instead of Mg, single-walled carbon nanotube powder is used together with $Co(CO)_3NO$. Peak positions from our data are identified by graphite (*) and face-centered cubic (f.c.c) structure of Co (♦) by comparison to previous experimental data[45] (Figure III-2(b)). Note that our data shows the presence of face-centered cubic structure of Co, not hexagonal close-packed (h.c.p) structure (the relative ratio of peak height is also similar to that of **B** in (b)).

The X-ray diffraction spectroscopy reveals that multi-walled carbon nanotubes with encapsulated Co (face-centered cubic) nanowires are synthesized because the sample contains a small amount of Co, even after long-time treatment with HCl. Also, interestingly, even though γ-Co (h.c.p) phase is the thermodynamically most stable at room temperature, only the high temperature α-Co (f.c.c) phase (> 450ºC) is detected. The transition temperature is about 338ºC. A possible explanation[46] is that after α-Co (f.c.c) is formed at 900ºC, in subsequent rapid cooling processes the tight graphitic envelope surrounding α-Co (f.c.c) prohibits structural change to γ-Co (h.c.p) due to spatial constraints. As a result, the α-Co (f.c.c) can remain stable at room temperature. The formation of Co-filled multi-walled carbon nanotubes is further verified by TEM images shown in Figure III-3 and III-4.

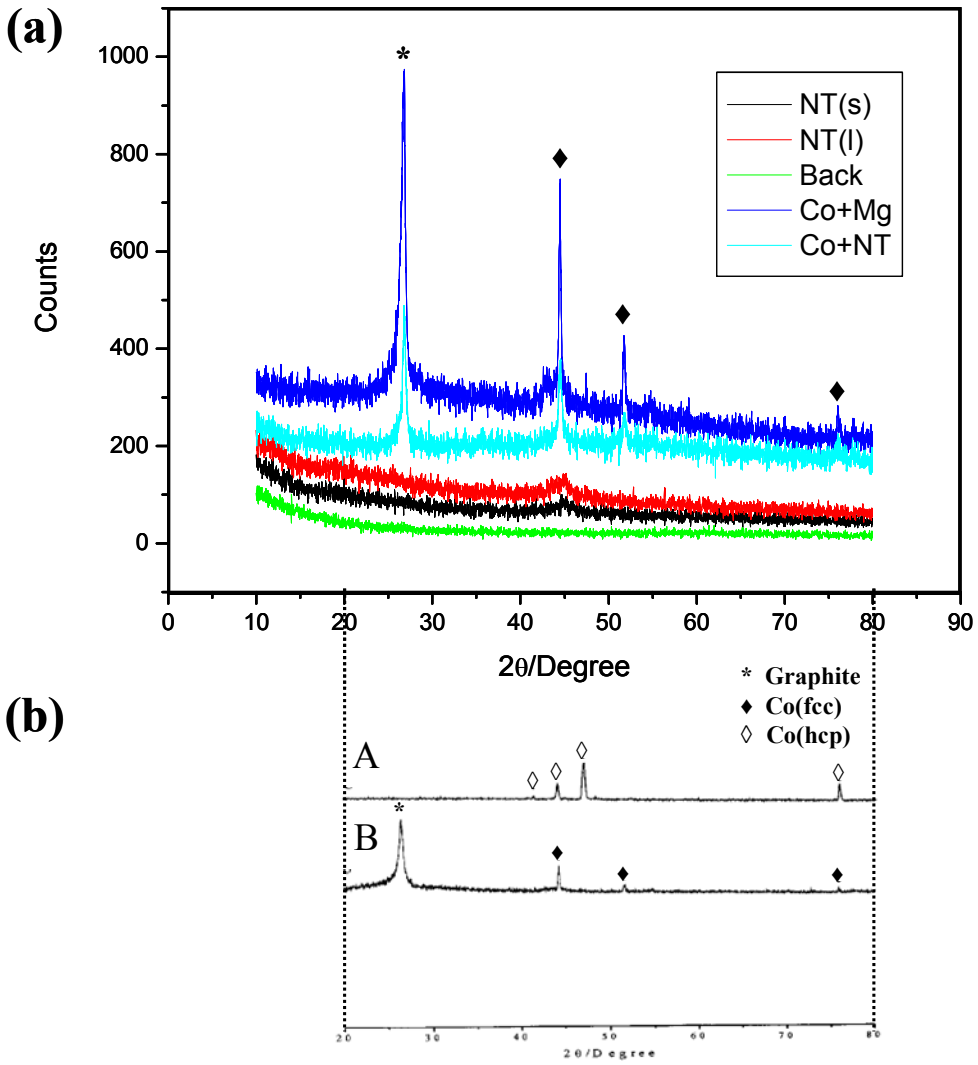


Figure III-2. X-Ray diffraction spectroscopy of nanotube powder samples. (a) From the bottom, the green curve comes from background, the black and the red from single-walled nanotube powder (CoMoCat™ purified single-walled nanotubes), cyan from the recipe with $Co(CO)_3NO$ and single-walled nanotube powder, and blue from $Co(CO)_3NO$ and Mg powder. Peaks from data are identified with graphite (*) and face-centered cubic structure of Co (♦). (b) Data from the reference[45] is put on the same horizontal scale as (a). **A** (upper) corresponds to hexagonal close-packed structure of Co (◊). And **B** (lower) is obtained from Co-filled multi-walled carbon nanotubes.

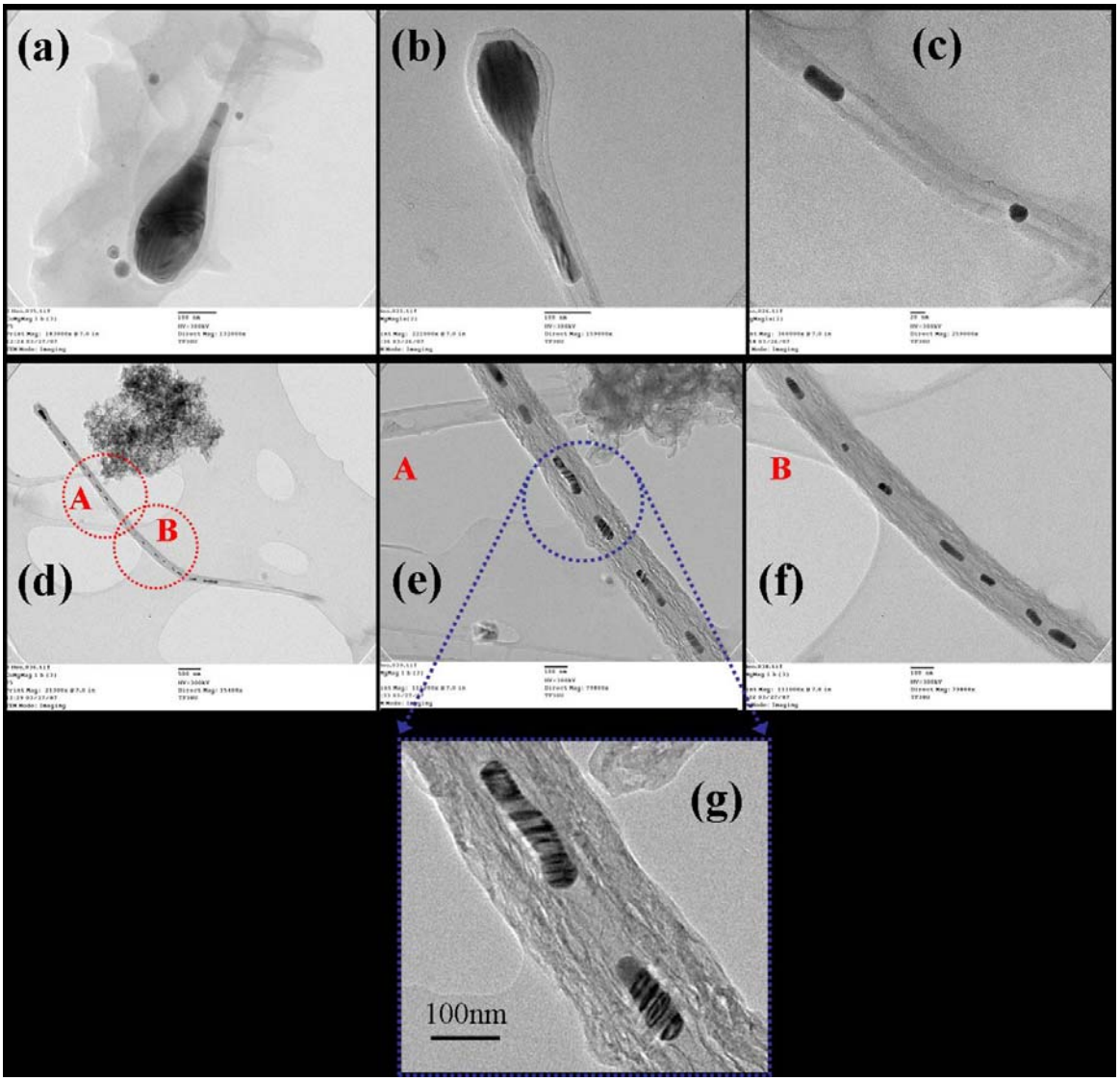


Figure III-3. TEM images of Co-filled multi-walled carbon nanotubes. (a) and (b) Large cluster of Co in nanotube tips. (c) and (d) Discontinuous Co nanowires inside nanotubes. (e) and (f) Zoomed-in images from dotted circles in (d). (g) Boundaries and stacking faults inside Co nanowires are shown. Scale bars in (a), (b), (e), (f), and (g) are 100nm, and 20nm in (c) and 500nm in (d).

A possible growth mechanism[45,46] is as follows: First, at 900ºC, $Co(CO)_3NO$ is decomposed into Co, CO, and NO. Subsequently, CO reacts with Mg to yield MgO and carbon,

$$Co(CO)_3NO(g) \rightarrow Co(s) + 3CO(g) + NO(g) \quad \text{(III.1)}$$

$$CO(g) + Mg(s) \rightarrow MgO(s) + C(s) \quad \text{(III.2)}$$

Decomposed Co from Equation III.1 acts as catalyst to create nanotubes, and at the same time, the Co catalyst is encapsulated inside nanotubes. In other words, the catalysts not only provide the nucleation centers for carbon nanotube growth, but also are the active sites for the decomposition of carbon-containing precursor.

After Co clusters are formed as in Equation III.1, carbon atoms from Equation III.2 dissolve and diffuse into the surface of the clusters to form a metal-carbon solid solution. Nanotubes are grown when supersaturation takes place to lead carbon precipitation into a crystalline tubular form. The growth continues as more carbon is produced. TEM images in Figure III-3(a), (b), and (d) support this idea because Co clusters in closed nanotube tips are found. Discontinuous filling of Co nanowires is also observed in Figure III-3(c) to (g). It is well known that the melting temperature of nanocrystalline particles depends strongly upon the grain size.[47] Theoretical calculations indicate that the melting temperature of single crystals encapsulated in carbon nanotubes is strongly suppressed.[48] It suggests that Co catalyst particle may be in a liquid or quasi-liquid state at the growth temperature. Then, the discontinuous pieces of Co nanowires could be the part of the Co cluster in closed nanotube tips. In other words, when the Co cluster is molded into elongated form as nanotube grows, it may be cut into several pieces along the nanotube. Another possibility is that molten Co could be drawn into the nanotube by capillary

force.[49,50] Molten Co nanoparticles are intermittently pulled into the nanotube as the growth continues to form a discontinuously filled nanotube.

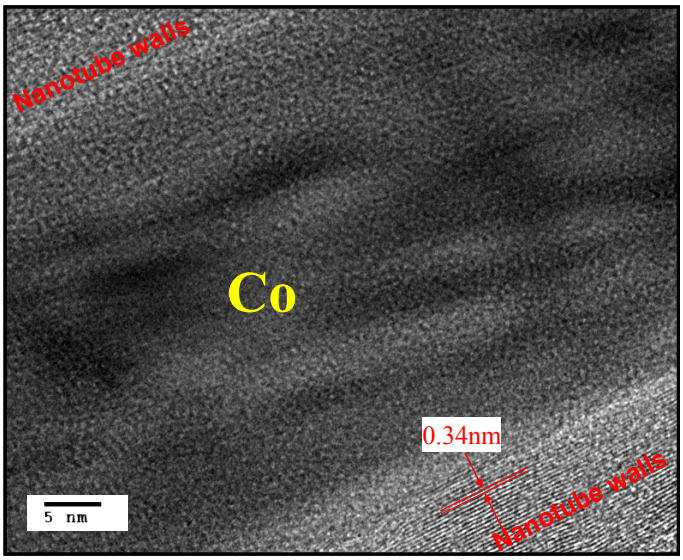


Figure III-4. TEM image of Co-filled multi-walled carbon nanotube. Nanotube walls encapsulating Co nanowire are clearly seen. Distance between walls is 0.34 nm.

From TEM images of filled Co nanowires, we frequently find boundaries or stacking faults (for example, see Figure III-3(g)). These defects have been known to frequently occur in f.c.c structures. During rapid cooling after growth, elastic strains at the interface between Co nanoparticle and nanotube walls may be responsible for the observed distortions.[46] Figure III-4 shows that graphitic basal planes are stacked parallel to metallic core with a 0.34 nm interplanar spacing. The absence of an observed gap or other phase between Co and the nanotube walls suggests that the first layer of the nanotubes is directly formed on the surface of Co, which supports the proposed growth mechanism.

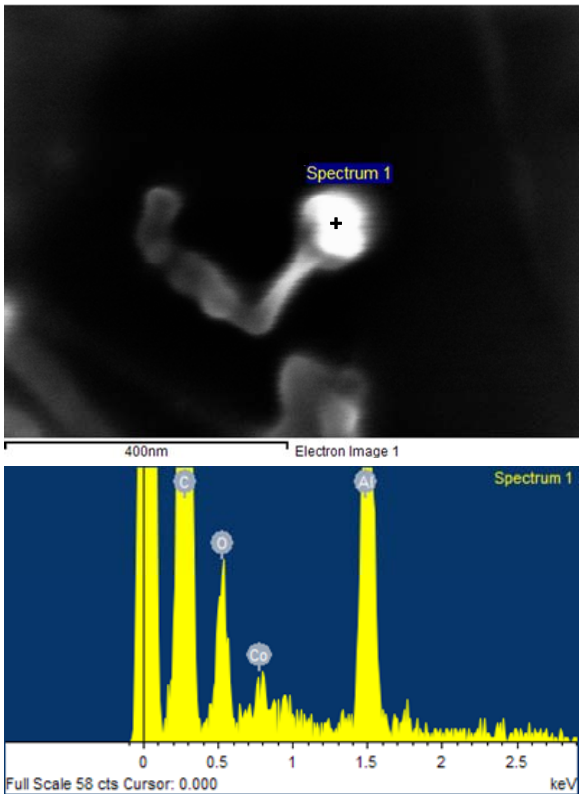


Figure III-5. Energy dispersive X-ray spectroscopy (EDS) of Co-filled multi-walled carbon nanotubes. SEM image of a Co-filled nanotube (upper) and EDS data (lower) on center of bright region are shown.

An SEM image of a Co-filled multi-walled carbon nanotube is shown in the upper part of Figure III-5. As seen from the TEM image, a large “head” containing a Co cluster also appears and it is brighter than its tail. To analyze which elements are contained in the SEM image, we can use the energy dispersive X-ray spectrometer incorporated in our SEM. Energy dispersive X-ray spectroscopy (EDS) is a technique for elemental analysis, where the radiated X-ray beam emitted from a specific material is collected after the incident electron beam is focused on it. Since each element of the periodic table has a

unique atomic structure, the characteristic X-rays from each element can be uniquely distinguished from others. Generally, the incident beam excites an electron in the inner shell of an element leaving a hole in the shell, which is followed by the hole filling with an electron from outer shell. The difference in energy between the electronic orbitals is released in the form of an X-ray photon. The X-rays emitted by the sample are then detected and analyzed by the energy dispersive spectrometer.

The lower part of Figure III-5 shows EDS data taken at about the center of bright region in SEM image with 3 keV electron energy in the incident beam. It distinctly reveals that Co is contained in the nanotube tip. Also carbon from graphitic walls is detected, as well as oxygen and aluminum from the substrate. Since the section of nanotube encapsulating Co appears especially bright in the image, defining electrodes on bright segments of nanotubes most likely gives Co-filled nanotube devices.

## III-4 Magnetoresistance of Co-filled multi-walled carbon nanotubes

### Current driven annealing

Figure III-6 shows *I-V* characteristics of a Co-filled nanotube. An SEM image of the device is inserted as well. Note that the tip of nanotube and also the region between contacts have similar brightness. Different curves in the *I-V* plot correspond to different sweeps of source-drain voltage. Each data is recorded by increasing bias voltage slowly, and the voltage is reset to zero when a current jump occurs.

From TEM images of produced Co-filled multi-walled nanotubes in Figure III-3, graphitization of carbon, which would produce parallel fringes in the TEM image, did not seem perfect during growth. But, in previous experiments, flowing a large current through defective multi-walled nanotube leads to further graphitization of amorphous carbon due to Joule heating and an electromigration effect, resulting in a large improvement of conductance.[51] This current driven annealing of multi-walled carbon nanotubes is also

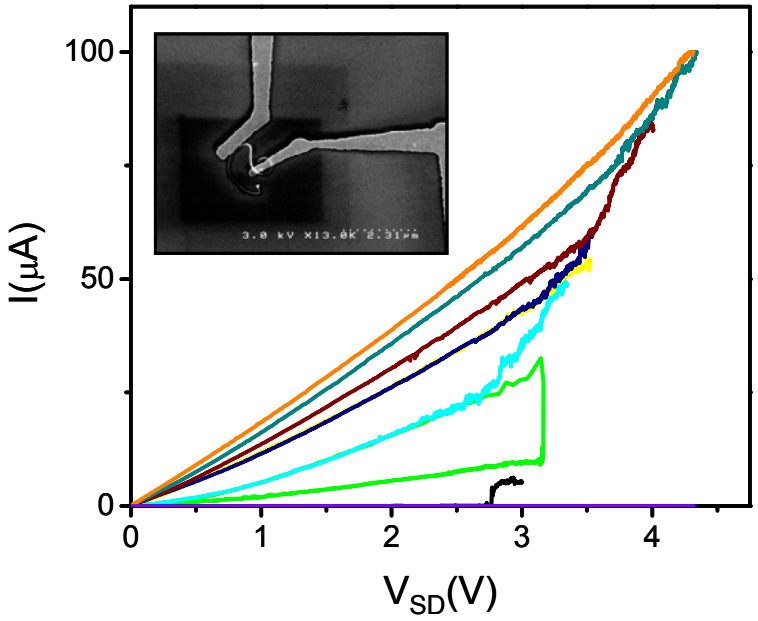


Figure III-6. Current-driven annealing of a Co-filled multi-walled carbon nanotube device

observed as improved conductance after each large voltage sweep in our device. For a typical device, a few MΩ of two-terminal resistance becomes less than 100 kΩ. Applying larger current causes breakdown (Figure III-7) or thinning-down (Figure III-8) of multi-

walled nanotubes. Figure III-7(a) shows failure of a device at about 4.4 V of bias voltage with SEM picture of broken nanotube device around the center. More broken nanotubes are shown in the right side of (b). Thinning-down of multi-walled carbon nanotube is probably caused by a similar mechanism to that observed previously in controlled wall by wall breakdown experiments.[52,53]

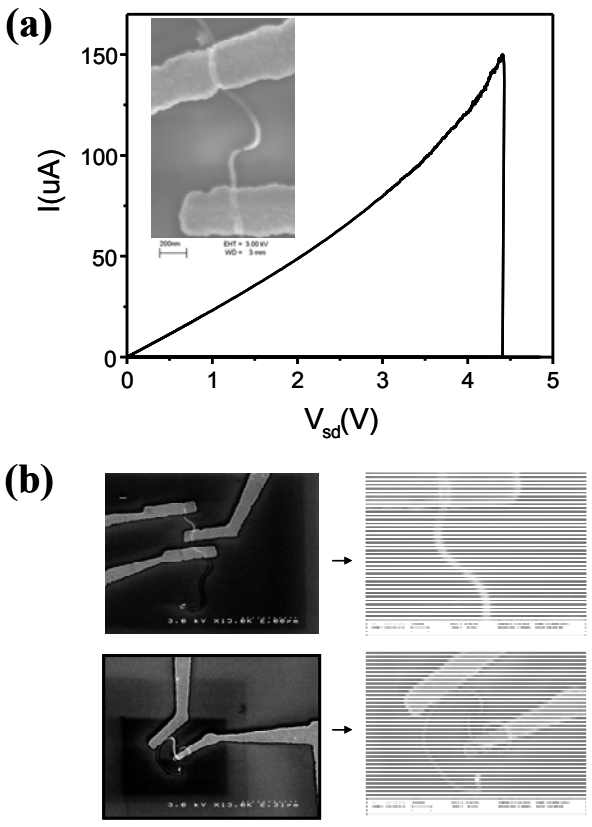


Figure III-7. Breakdown of Co-filled multi-walled nanotubes

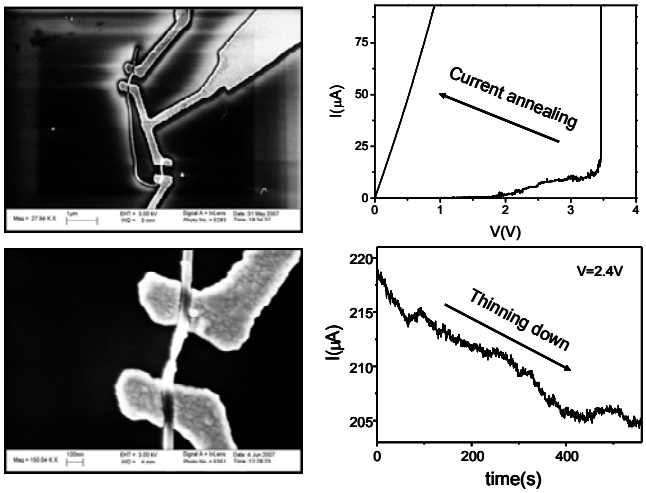


Figure III-8. Thinning-down of Co-filled multi-walled nanotubes

**Magnetoresistance of Co-filled multi-walled carbon nanotubes**

A magnetic field parallel or perpendicular to the Co-filled multi-walled carbon nanotube devices is swept to study its magnetoresistance at 1.4K.

Figure III-9 shows magnetic-field-induced switching of a Co-filled nanotube device. When a magnetic field parallel to the nanotube axis is applied and varied (Figure III-9(a)), current through the device is recorded (Figure III-9(b)). Abrupt jump or drop in current is observed at around ±0.7 T. This switching behavior was reproducible and occurred at the same field. ~ 2% of magnetoresistance switching is reported in an individual Co-filled nanotube device for the first time. Switching also occurs at the same field over the range of bias voltages studied (Figure III-9(c) and (d)). Though longitudinal magnetic switching of Co (h.c.p) nanowires is reported previously[54,55] due to the aligned orientation of

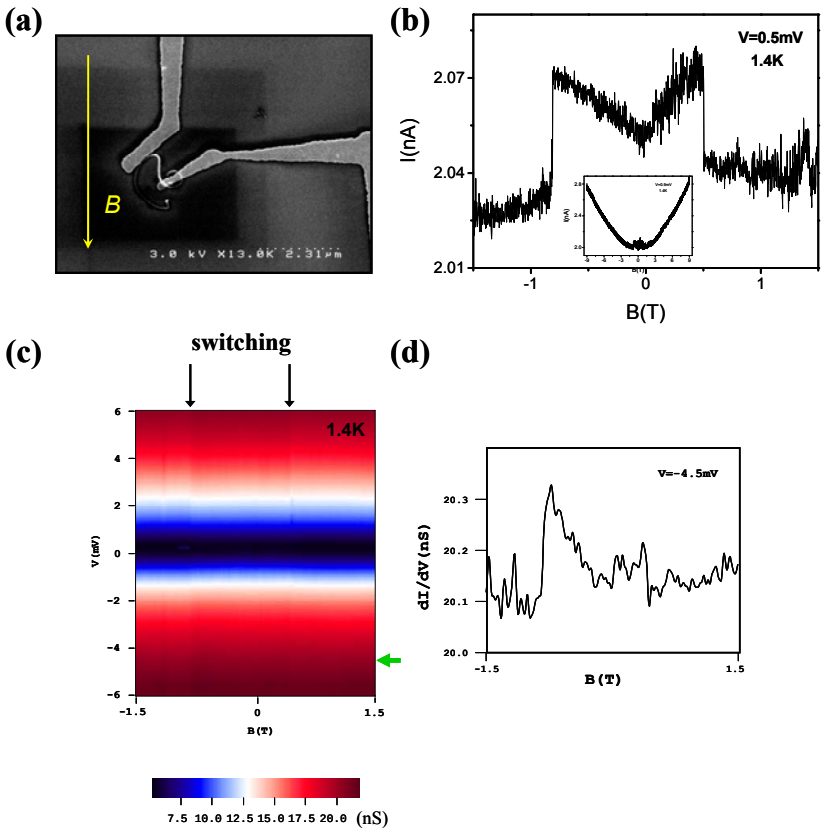


Figure III-9. Magnetoresistance switching of a Co-filled multi-walled carbon nanotube device. (a) SEM image of the device and direction of the approximately parallel magnetic field direction is drawn. (b) Current versus magnetic field plot showing switching behavior at about ±0.7 T (measured at 1.4 K). Larger range sweep of magnetic field (-9 to 9 T) is shown in the inset. (c) Color plot of current versus bias voltage (vertical axis) and magnetic field (horizontal axis). The switching is observed at the same field throughout the bias voltage sweep. (d) Line trace of current versus magnetic field at -4.5 mV of bias voltage (green arrow in (c)). The switching is clearly seen.

magnetization along magnetic field direction, the origin of the switching of Co-filled nanotube is not clear. A detailed analysis would include the effect of the magnetization of a single magnetic domain (for f.c.c Co nanowire) on the electron transport of the

nanotube. In addition, the Co nanowire could be split into multiple segments and also include boundaries and faults as seen in TEM images.

**III-5 Future work**

Even though Co-filled multi-walled carbon nanotubes were successfully synthesized, the filling factor of Co nanowire inside nanotube needs to be increased. Moreover, less defective, better graphitized nanotube walls are required for future device applications. Ideally, single-walled nanotubes encapsulating ferromagnetic metals would be produced. Also, it would be interesting to study not only the magnetoresistance of the single Co-filled multi-walled nanotubes presented here, but also that of crossed Co-filled nanotubes. Specifically, the crossed Co-filled nanotube geometry gives spin-valve devices where it should be possible to study intertube conductance in two different magnetization orientations. Note that we expect to have two magnetization orientations because of the difference in coercive fields between two mesoscopic Co nanowires and to select crossed tubes which have crossing angle substantially less than 90º so that two situations do not have equal conductance by symmetry. For these devices, we can also test the dependence on spin polarization as the number of nanotube shells in the nanotubes are varied by using the shell-by-shell breakdown technique[52] to successively reduce the number of shells in each nanotube one-by-one. A thorough study of this should enable theories to be tested to explore the potential of filled carbon nanotubes as nanoscale spintronic devices.

## III-6 Summary

Co-filled multi-walled carbon nanotubes are produced via pyrolysis of a mixture of $Co(CO)_3NO$ and Mg powder. X-ray diffraction spectroscopy on post-growth HCl treated material reveals a face-centered cubic structure of Co encapsulated inside multi-walled carbon nanotubes. Based on TEM images of individual Co-filled nanotubes, a growth mechanism is proposed. At 900ºC, the decomposition of $Co(CO)_3NO$ gives Co catalyst and also CO which is subsequently reduced to C by Mg. Co nanoclusters act as a catalyst to create nanotubes, and at the same time, the nanoclusters are encapsulated inside nanotubes. The observed discontinuous filling of Co nanowires along nanotubes is possibly resulted by re-molding of elongated Co nanocluster catalyst or subsequent drawing in of molten Co nanoparticles by capillary forces into nanotubes. The high contrast region of Co-filled nanotubes in SEM images is confirmed to be concentrated in Co by energy dispersive X-ray spectroscopy, and subsequent metal-contacting on those regions gives Co-filled nanotube devices. Conductance through defective Co-filled nanotube devices is improved by current-driven annealing, and applying larger current breaks nanotubes or thins them down. A ~ 2% of magnetoresistance switching at about ±0.7 T of magnetic field is observed in a Co-fill nanotube device, and a thorough analysis including the interaction between electron transport in the nanotubes and magnetic domains of Co nanowires is required to explain the behavior. For future work, more controlled growth of Co-filled nanotubes having fewer structural defects on nanotube walls and the large filling factor of Co nanowire is desirable, and a magneto-conductance study on crossed Co-filled nanotubes is highly desirable for device applications.

*Chapter IV*

# TRANSVERSE ELECTRIC AND MAGNETIC FIELD EFFECT ON THE ELECTRON TRANSPORT OF MULTI-WALLED CARBON NANOTUBES

## IV-1 Abstract

A transverse electric field was applied on multi-walled carbon nanotube devices (~ 700 nm long) between two side gates with the separation of ~ 150 nm. The opposite electric potentials on two side gates were tuned to be symmetric in order not to perturb the charge density of the nanotube. As the transverse electric field swept (typically up to ± 25 V/150 nm), conductance fluctuations of the nanotube device were observed. The characteristic conductance peak spacing showed sample-specific variations, but was typically on the order of a few volts in side gate voltage. A possible explanation presented is based on the modification of the band structure of nanotube when the transverse electric field is comparable to the subband spacing of the nanotube.[56,57] Multi-walled carbon nanotube devices are further characterized by applying a transverse magnetic field to show weak localization (WL) and universal conductance fluctuations (UCF). These behaviors were compared to the previous theories to estimate the phase coherence length.

## IV-2 Introduction

### IV-2-1 Band Structure Modulation of Nanotubes in a Transverse Electric Field

Studies on the modification of the band structure of carbon nanotubes by external fields are of interest for basic research as well as for future device applications. For example, the linear band structure (see section I-2-5), which is the characteristic signature of metallic nanotubes, can be suppressed by a parallel magnetic field to open a minigap at the band crossing point.[58] When an applied transverse electric field is comparable to the subband spacing of nanotubes, the original band structure is modified due to subband mixing. In this section, I will summarize important results from reference 57, which later will have a few implications in the analysis of our experimental results.

The energy difference, $E_s$, between the two nearest subband of nanotube is approximated in low-energy model as

$$E_s = \frac{3}{2} E_g = \frac{\hbar v_F}{R} \qquad \text{(IV.1)}$$

using Equation I.34, and where $R$ is the tube radius. Then, the critical electric field, $E_c$, is defined when its energy is equal to subband spacing,

$$\begin{aligned} eE_c R &= \frac{\hbar v_F}{R} \\ E_c &= \frac{\hbar v_F}{eR^2} \quad . \end{aligned} \qquad \text{(IV.2)}$$

Evaluating these expressions for $v_F \approx 8.0\times10^5$ m/s, $e \approx 1.6\times10^{-19}$ C, and $\hbar \approx 1.1\times10^{-34}$ J/s, we get

$$E_c[\mathrm{MV/cm}] = 5.3 / R^2[\mathrm{nm}^2]. \quad \text{(IV.3)}$$

For 150 nm of the separation between two side gates, the critical voltage $V_c$,

$$V_c = \frac{80\mathrm{V}}{(R[\mathrm{nm}])^2}. \quad \text{(IV.4)}$$

But, the nanotube itself is polarized responding to the external electric field to screen the field partially. The dielectric function, $\varepsilon$ is defined as the ratio of the external electric field, $E_{ex}$ to the total electric field, $E_{tot}$,

$$\varepsilon = E_{ex} / E_{tot}. \quad \text{(IV.5)}$$

When the Fermi level, $E_F$ is at the charge neutrality point, the dielectric function is independent of tube radius and $\varepsilon \approx 5$ for both semiconducting and metallic tubes. If the Fermi level shifts away from the charge neutrality point, the polarizability depends on the occupation or depletion of new states. The dielectric function for metallic tube of radius $R$, $\varepsilon^{met}$ can be written as

$$\varepsilon^{met}(E_F, R) \approx \varepsilon^{met}(0) + 6.9\left(\frac{E_F R}{\hbar v_F}\right)^2 \quad \text{(IV.6)}$$

in cgs units. According to Equation IV.6, the dielectric screening increases with the radius of the tube and also with the Fermi level. Assuming the Fermi level is at the charge neutrality point, then $\varepsilon \approx 5$, the critical potential in Equation IV.4 is given by

$$V_c = \frac{400\text{V}}{(R[\text{nm}])^2}. \qquad \text{(IV.7)}$$

For $R$ = 10 nm tube, $V_c$ = 4 V.

Figure IV-1 shows the band structure modulation of (10, 10) armchair tube. At $E_{trans}$ = 0.1V/ Å, the two lowest subbands are flattened near the Fermi points. At the same

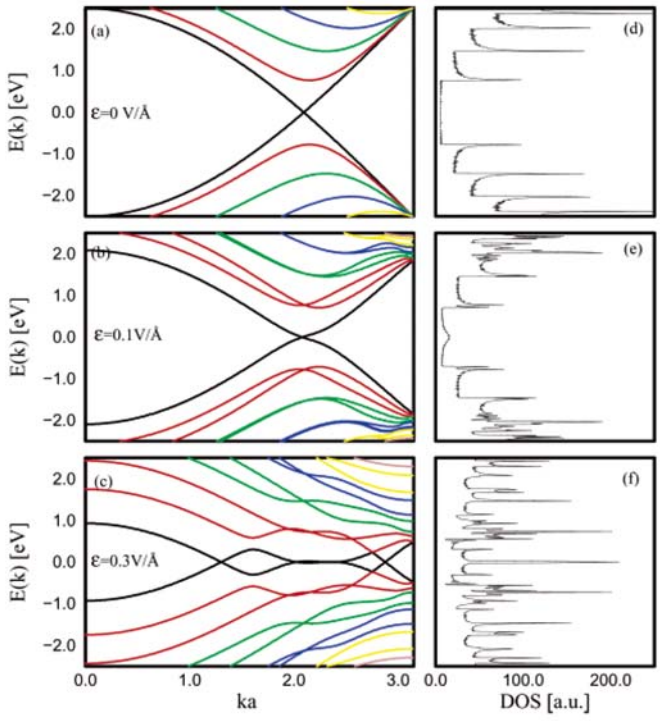


Figure IV-1. Band structure ((a), (b), and (c)) and the density of states ((d), (e), and (f)) of a (10, 10) armchair tube at various transverse electric fields: $E_{trans}$ = 0, 0.1 and 0.3 V/Å. Higher bands ($E$ > 2.5 eV) are not displayed.

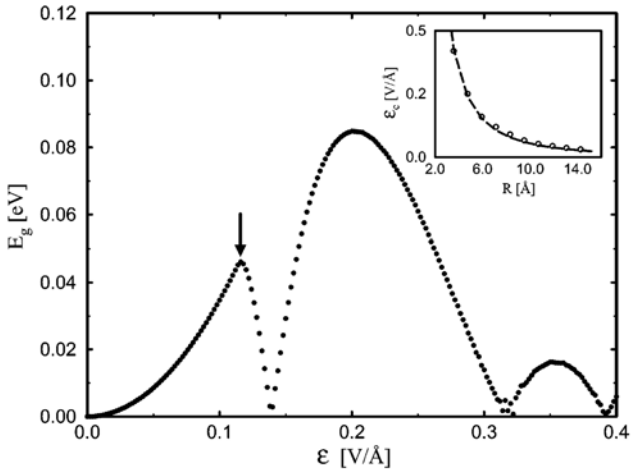


Figure IV-2. Band gap variation of a (18, 0) tube with increasing field strength. The arrow indicates the critical field.

time, all degenerate subbands are split. The splitting becomes more obvious for the lowest subbands. As the field strength increases, subbands show oscillatory bends, forming multiple valleys. But, the zero-gap structure of armchair tubes are always preserved. In terms of the density of states (DOS) in Figure IV-1 (d), (e), and (f), as the field is applied, the low-energy plateau displays a bump which increases with field. The enhanced DOS near $E$=0 is due to the flattening and bending of the two lowest subbands. On the other hand, the single van Hove peaks are split into multiple ones.

For zigzag metallic tubes, band gap opens and closes as the field increases ((18, 0) zigzag tube is shown in Figure IV-2). The critical band gap at the critical field (arrow in Figure IV-2 for (18, 0) tube) is approximately

$$E_{gc} = \frac{\hbar^2 v_F^2}{6tR} \qquad \text{(IV.8)}$$

where $t$ = 2.5 eV. For $R$ = 10 nm zigzag tube, $E_{gc}$ = 0.18 meV ~ $k_BT$ at 1.4K which is the base temperature of our cryostat.

## IV-3 Transverse Electric Field Effect on Differential Conductance of Multi-Walled Carbon Nanotube Devices

Multi-walled carbon nanotubes (diameter of ~ 10−20 nm) are deposited on the silicon substrate. For applying a transverse electric field, two close side gates are defined beside two contact electrodes (Figure IV-3(a)). The typical separation of two side gates is 150 nm, while the distance between two contacts is 400 nm. First, voltages $\pm V_{SG}$ are applied to the side gates (relative to the sample ground). These voltages usually shift the Fermi level of the nanotube and thereby the charge density because of the unintentional experimental asymmetries between the two side gates (non-equal distance or different shape and hence different capacitance). It can be seen as the shifts of peaks on back gate voltage as $|V_{SD}|$ increases. This asymmetry is corrected by applying appropriate voltages $+V_{SG}$, $-V'_{SG}$ on each side gate. Then, the Fermi level of the nanotube is independently controlled by the back gate voltage only.

Figure IV-3(b) shows the color scale plot of differential conductance versus side gate voltage, $V_{SG} = |V_{SG}| + |V'_{SG}|$ (vertical axis) and back gate voltage, $V_g$ (horizontal axis) taken at 1.4K. Remarkably, the conductance fluctuations on the side gate voltage as well as the back gate voltage are seen as a cross stripe pattern (every device measured shows a similar pattern). Back gate voltage trace at $V_{SG}$=0 is shown in Figure IV-3(c) with the peak spacing of 0.34 V. In Figure IV-3(d), differential conductance as a function of side

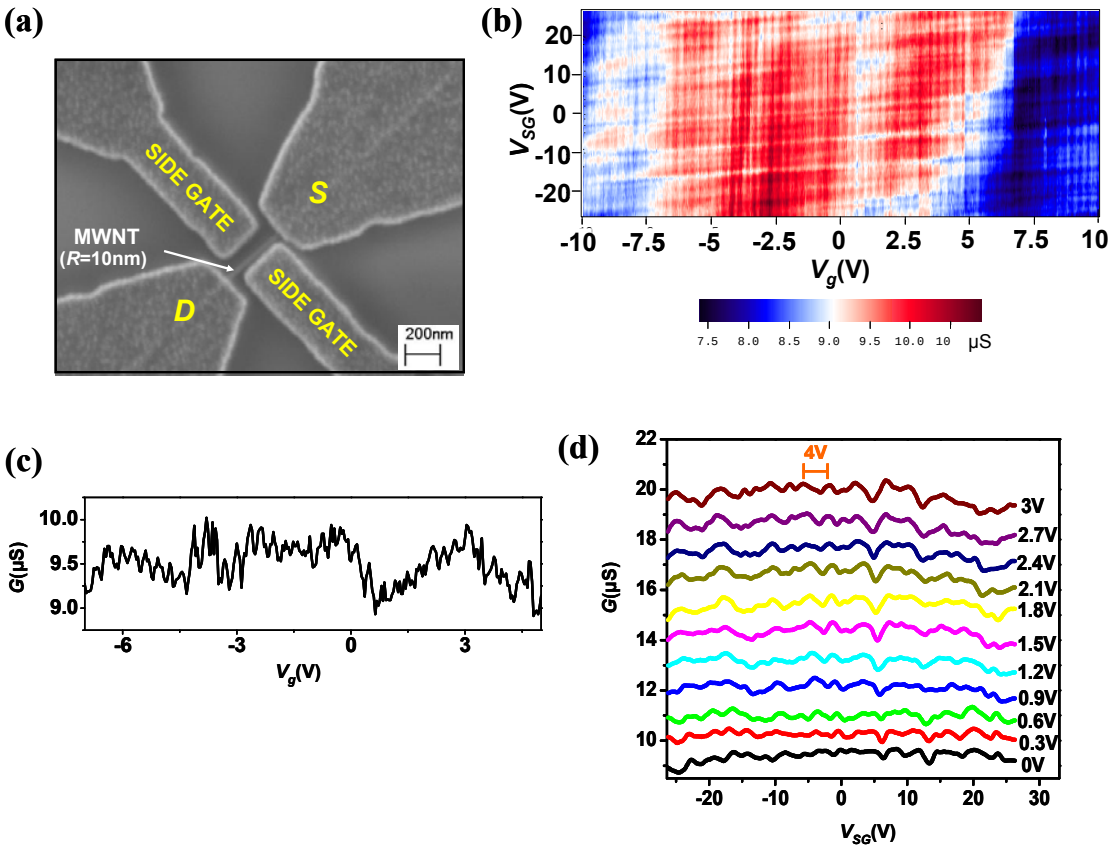


Figure IV-3. Transverse electric field effect on differential conductance of a multi-walled carbon nanotube device. (a) SEM image of MWNT device. MWNT, source (S) and drain (D) and two side gate electrodes are indicated. $+V_{SG}$, $-V'_{SG}$ of side gate voltages produces a transverse electric field. (b) Color scale plot of differential conductance versus back gate voltage (horizontal axis) and side gate voltage (vertical axis) where red means more conductive. Cross stripes are clearly seen. (c) Line trace of differential conductance taken at $V_{SG}$ = 0 V. (d) Line traces of differential conductance taken from $V_g$ = 0 V to $V_g$ = 3 V with 0.3 V of step size. Each curve is offset by $V_g$ (V)/0.3 (μS). Conductance peaks and dips are nearly independent of back gate voltage. Orange bar on the top indicates the theoretical estimation of critical voltage (Equation IV.7) for this $R$=10 nm tube.

gate voltage is plotted and each curve is taken at different back gate voltages ($V_g$) from 0 to 3 V, vertically offset by $V_g$ (V)/0.3 (μS). Nearly $V_g$-independent conductance oscillations are observed with the period of a few volts. The orange bar on the top indicates 4 V of the critical voltage from Equation IV.7 for $R$ = 10 nm tube. The observed

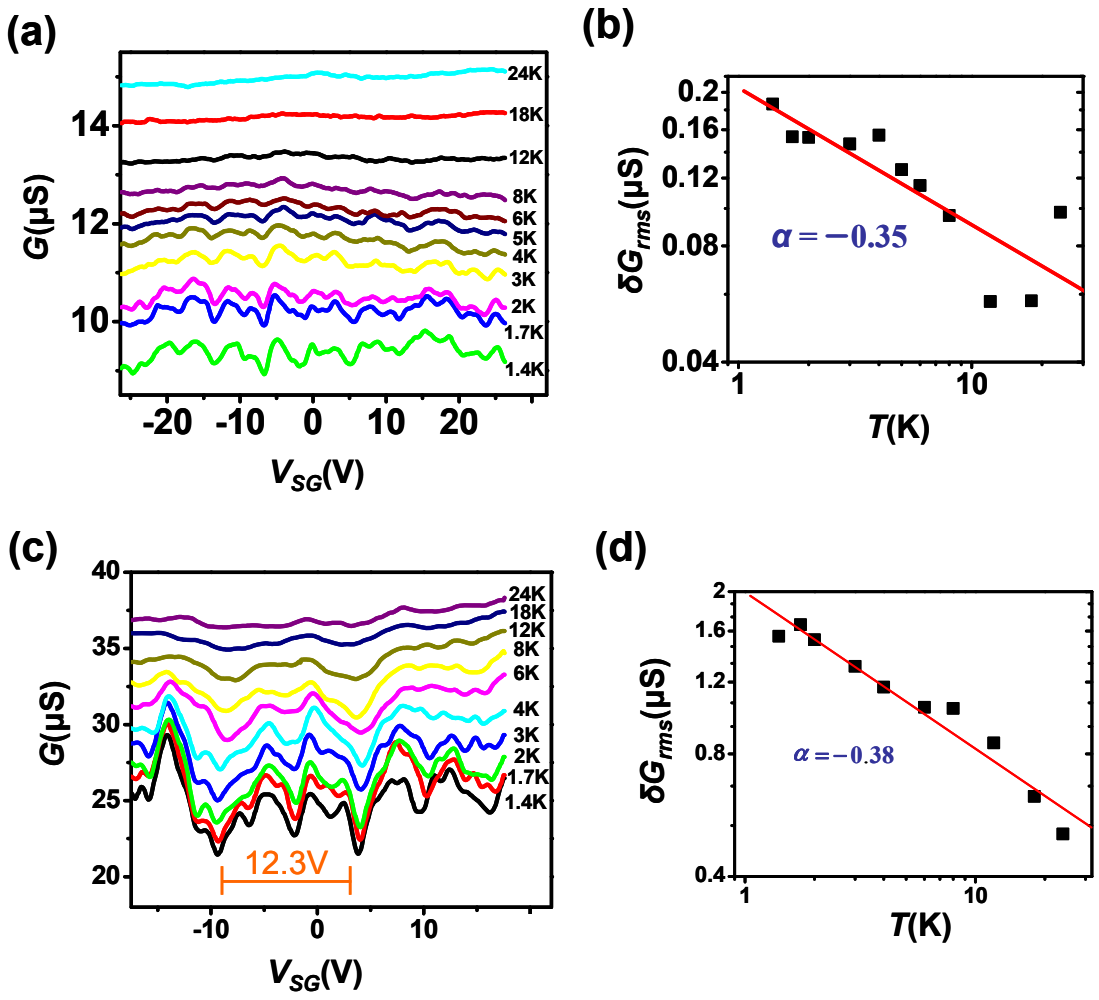


Figure IV-4. Temperature dependence of transverse electric field effect. (a) Conductance variations with side gate voltage at different temperatures (from 1.4K to 24K). (b) Root mean square (RMS) of conductance oscillations versus temperature in log scale. Black squares represent the data and red line shows fit to the data with $\delta G_{rms} \propto T^{\alpha}$, $\alpha$=-0.35 (c) Conductance variation for another device with tube radius, $R$=5.7 nm. The critical voltage is indicated by orange bar, 12.3 V. (d) RMS of conductance oscillations with the fit, $\alpha$=-0.38.

period of a few volts and the calculated 4 V critical voltage are on the same order of magnitude, possibly implying experimental observation of modulated band structure due to subband mixing by transverse electric field.

Our experimental setup, using large diameter multi-walled tubes where only the outermost shell contributes to the electronic conductance and close side gates, enables reaching a few times the expected critical voltage for opening and closing a bandgap, which likely modifies the band structure of the nanotube. The origin of periodic conductance oscillations as a function of side gate voltage is not yet known conclusively. But, as the field strength increases, the theory (Section IV-1) predicts that subbands show oscillatory bends, forming multiple valleys, and also that bandgap oscillates with the order of critical field for zigzag tubes, which qualitatively explains our data.

The temperature dependence of conductance variation with side gate voltages is plotted in Figure IV-4. (a)–(b) is the same device as Figure IV-3 and (c)–(d) show another device with tube radius, $R$ = 5.7 nm. The root mean square of conductance oscillations is plotted as squares in (b) and (d). As temperature increases, the conductance level rises with thermal smearing of fluctuation features. Fit with $\delta G_{rms} \propto T^{\alpha}$ gives $\alpha$ = -0.35 and -0.38. For other devices (not shown), $\alpha$ = -0.60 and -0.69.

## IV-4 Transverse Magnetic Field Effect on Differential Conductance of Multi-Walled Carbon Nanotube Devices

A perpendicular magnetic field is applied on a multi-walled nanotube device shown in Figure IV-5(a). The differential conductance versus magnetic field (horizontal axis) and back gate voltage (vertical axis) is plotted in (b) with color scale, where red indicates larger conductance.

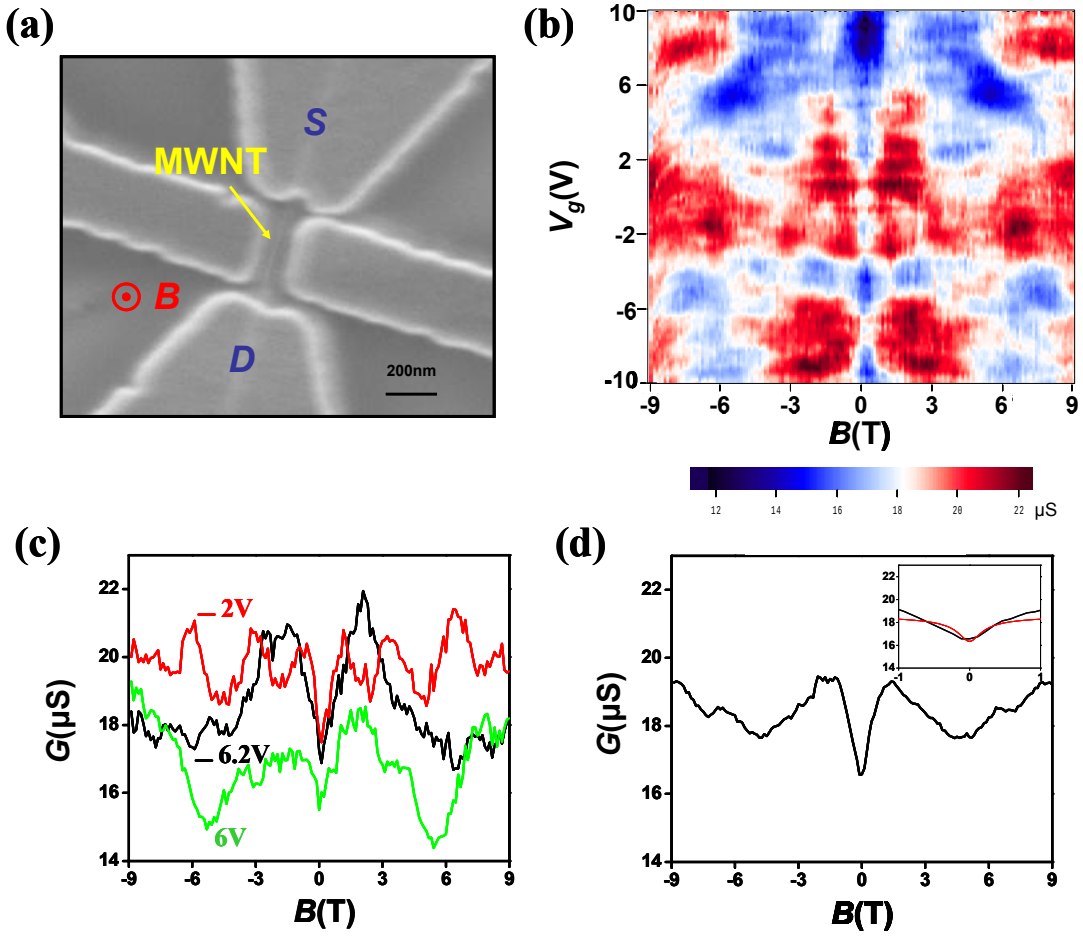


Figure IV-5. Magnetoconductance of a multi-walled carbon nanotube device. (a) SEM image of MWNT device. MWNT, source (S) and drain (D) electrodes are indicated when magnetic field (B) is perpendicular to the device. (b) Color scale plot of differential conductance versus magnetic field (horizontal axis) and back gate voltage (vertical axis) where red indictaes larger conductance. (c) Line traces taken at $V_g$= −6.2,−2 and 6 V. The signature of WL (positive magnetoconductance within $B$ = ±1T) is seen independent of gate voltage whereas aperiodic UCF ($B$ > ±1T) varies. (d) Ensemble average of magnetoconductance over the whole range of gate voltage (-10 to 10 V). Inset shows the data (black) within $B$=±1T and fitting curve (red) using Equation IV.9.

A symmetric feature about $B$ = 0 T is observed with the local minima at 0 T. Detailed features of conductance fluctuations with magnetic field vary with back gate voltage like in Figure IV-5(c), for example. The observed positive magnetoconductance around 0 T

can be attributed to weak localization (WL) in the diffusive transport regime (Appendix IV-6-1). Enhanced quantum-mechanical backscattering at $B$ = 0 T is suppressed as magnetic field breaks time reversal symmetry, leading to the increase in conductance. The characteristic field for positive magnetoconductance is ~ ± 1 T for all curves. Aperiodic conductance fluctuations at higher fields are also seen in Figure IV-5(c). Those fluctuations can be well explained in terms of universal conductance oscillations (UCF) (Appendix IV-6-2). The UCF amplitude at 1.4K is comparable to the zero field WL feature. An explanation of why UCF features vary with the back gate voltage is as follows: Each value of the back gate voltage, and hence of the Fermi level, $E_F$ of the nanotube, corresponds to a different Fermi wavelength and thus, a change of the phase shifts between different scatters. If the change in back gate voltage, and hence in $E_F$, is sufficiently large, a complete scrambling of the interference pattern can be achieved. The ensemble average over the entire range of back gate voltage (-10 V to 10 V) is plotted in Figure IV-5(d). The UCF amplitude is decreased, whereas WL feature still remains pronounced. Magnetoconductance in WL regime ($|B| < 1T$) is fit using Equation IV.9 with $l_\phi$ as a free parameter (inset in Figure IV-5(d)). We found $l_\phi$ = 38 nm, which is comparable to nanotube circumference ~ 50 nm.

Finally, for a nanotube with the diameter of 15 nm, the transverse electric field effect with perpendicular magnetic field is investigated (Figure IV-6). Figure IV-6(a) and (c) correspond to 0 T data, whereas (b) and (d) to 9 T. Typical cross stripe patterns for both data sets are observed, but with a difference in detailed features (this sample also exhibits positive magnetoconductance, back gate dependent aperiodic fluctuations like

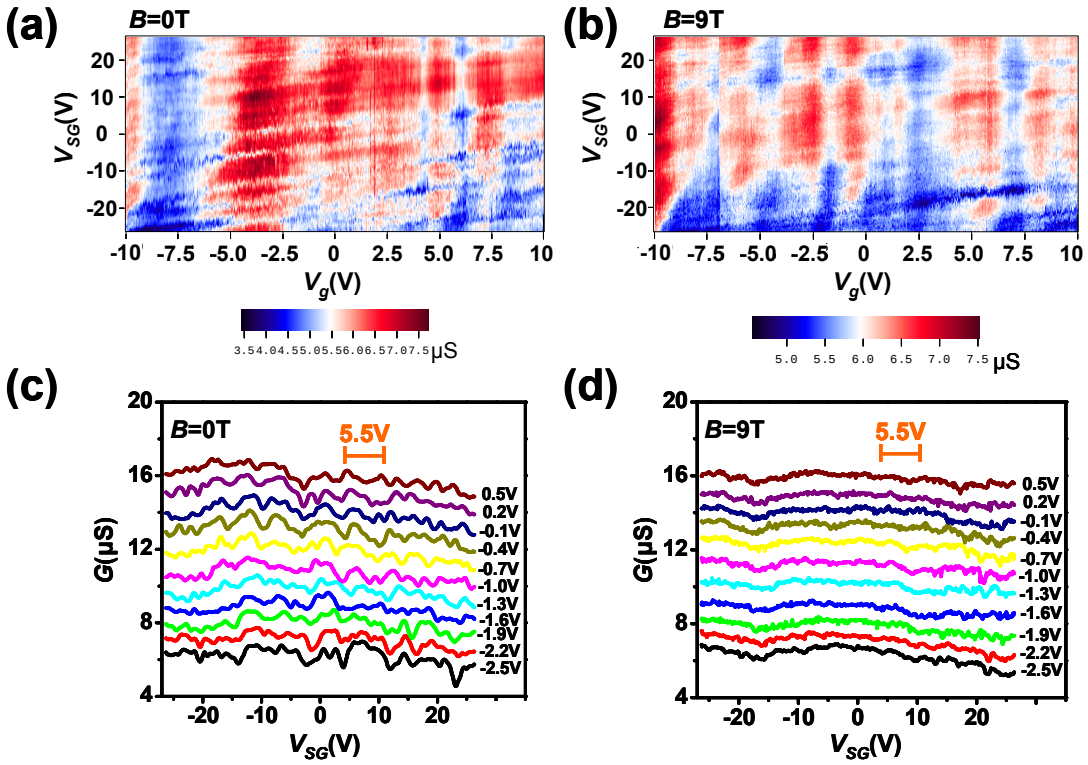


Figure IV-6. Transverse electric field effect with perpendicular magnetic field. (a) Color scale plot of differential conductance versus side gate voltage, $V_{SG}$ and back gate voltage, $V_g$ at $B$=0 T. (b) Color scale plot of differential conductance at 9 T. Usual cross stripe pattern is seen like 9(a), but detailed features are different from (a). (c) Differential conductance as a function of side gate voltage at 0 T is plotted at different back gate voltages (from -2.5 to 0.5). Each curve is offset by ($V_g$(V)+2.5)/0.3 (μS). The critical voltage is indicated by the orange bar, 5.5 V. (d) Similar data as (c) but at 9 T. The amplitude of conductance fluctuations are decreased.

Figure IV-5(b)). Interestingly, a high magnetic field (9 T) suppresses the conductance fluctuations induced by the transverse electric field as observed in Figure IV-6(d). Further analysis is necessary to explain the magnetic field suppression of transverse electric field effect.

## IV-5 Summary

A transverse electric field is applied symmetrically to a multi-walled carbon nanotube. Without changing the Fermi level of the nanotube, a transverse field induces backgate-independent conductance fluctuations with a period of roughly order of the field expected for strong subband mixing by the transverse field. This is expected to produce bandgap oscillation and band-bending, hence forming multiple valleys in the dispersion relations and enhanced DOS, which possibly explains our observation, although, the observed back gate independence of the effect is somewhat surprising in this picture. The transverse electric field-induced conductance fluctuations gradually diminish at higher temperatures. The RMS of these fluctuations have power law dependence with the exponent, $\alpha = -0.35 - -0.69$. Also, by applying a transverse magnetic field, WL effect with positive magnetoconductance at low field and UCFs at higher field are observed. Fitting with 1D WL theory gives 30−40 nm of phase coherence length in our multi-walled nanotube devices. Lastly, the magnetic field effect on electric field-induced conductance fluctuations is investigated, showing the suppressed fluctuations at high magnetic field. Further analysis is required to explain the data.

## IV-6 Appendix

### IV-6-1 Weak Localization in Multi-Walled Carbon Nanotubes

Weak localization (WL) is a quantum mechanical effect in a disordered electron system where electron motion is diffusive rather than ballistic. WL originates from the

quantum mechanical treatment of backscattering, which contains interference terms adding up constructively. In other words, quantum interference between self-crossing paths in which an electron can propagate in the clock-wise and counter-clockwise direction around a loop adds up constructively. The quantum phases cancel each other exactly due to the identical length of the two paths along a loop. Another way of describing this is that time reversal symmetry (TRS) enhances quantum mechanical backscattering, thereby leading to a resistance larger than the classical Drude resistance. But, TRS can be broken by applying an external magnetic field which causes a phase shift between two paths. The phase shift is proportional to the magnetic flux penetrating through the closed loop made from two paths. Then the interference terms cancel in a magnetic field of sufficient strength, resulting in negative magnetoresistance (or positive magnetoconductance)[59-61].

When the phase coherence length is comparable to the tube circumference and much shorter than device length, one-dimensional WL theory can be used. One-dimensional WL theory, which adequately takes dephasing by quasi-elastic scattering into account, predicts the correction to the conductance $\Delta G$ for a nanotube of diameter $D$ is given by[59,62]

$$\Delta G = -0.62\frac{e^2}{\hbar L}\left(\frac{1}{l_\phi^2}+\frac{D^2}{12l_m^4}\right)^{-1/2} \qquad \text{(IV.9)}$$

where $L$ is channel length, $l_\phi$ is phase coherent length, and $l_m(B)$ is the magnetic length, $l_m^2 = \hbar / eB$ .

### IV-6-2 Universal Conductance Fluctuations

Universal conductance fluctuations (UCF) are interesting phenomena in the field of quantum transport in disordered metals. Theory developed by B. L. Al'tshuler[63] and P. A. Lee et al.[64] predicts aperiodic conductance fluctuations as a function of magnetic field with RMS amplitude of order $e^2/\hbar$. Its origin is the quantum interference of electrons on different trajectories, which gives a non-zero average within a few elastic collisions. As the magnetic field increases, phase shifts of electrons occur, which result in a different interference pattern. The aperiodic magnetoresistance fluctuations due to UCF are observed in multi-walled carbon nanotubes.[59,61]

For multi-walled carbon nanotube samples, where the phase coherent length is less than the tube circumference, $L_\phi < \pi D < L$ , the device can be divided into $L/L_\phi$ conductors in series and $n\pi D/L_\phi$ conductors in parallel, each of them producing conductance fluctuations of the order of $e^2/\hbar$. The statistical self-averaging of the UCF results in fluctuations with RMS amplitude, [61,65]

$$\delta G_{rms} = 0.61\frac{e^2}{h}\left(\frac{n\pi D}{L_\phi}\right)^{1/2}\left(\frac{L_\phi}{L}\right)^{3/2}. \qquad \text{(IV.10)}$$

# CONCLUSION

Carbon nanotubes are a versatile material and have interesting electronic properties. Conceptually, nanotubes are described as rolled up 2D graphene sheets with chiral indices, $n$, $m$. The band structure of nanotubes is deduced from that of 2D graphene by imposing a periodic boundary condition around the circumference direction. Depending on whether an allowed wavevector takes Dirac points where conduction and valence bands meet, nanotubes can be metallic or semiconducting. These fundamental electronic properties of nantobues are investigated by EFM technique in Chapter I. By coupling AFM tip's motion with nanotubes' quantum capacitances, local DOS of nanotubes were resolved with non-scale spatial resolution under ambient conditions. This technique with measured nanotube diameter enables distinguishing individual semiconducting or metallic nanotubes, and it can be further utilized to trace the modified band structure of strained tubes, this enables an estimate of the chiral angle of a nanotube. Future work should enable detailed images of the local electronic structure of other nanomaterials to be directly compared to the results of further transport, optical, or sensing experiments.

Not only is electron transport interesting in single nanotubes, but also in crossed tubes. Nanotube loops, where nanotubes cross themselves to form loops during growth, as candidates for a single-walled nanotube interferometers are made and studied in Chapter II. SGM on semiconducting nanotube loop devices probed how current is split into two arms at the cross junction. Remarkably, the current through the loop segment can be controlled by back gate from 0% up to 50% of the total current. By applying a resistive circuit model, the resistance on each segment was estimated from DC EFM data together

with SGM data. As expected, the loop segment is more resistive than the other parts by an order of magnitude. For metallic loop devices, two different periodic conductance oscillations as a function of gate voltage are observed at low temperature. As a speculation, the slow mode is assigned to Sagnac-type interference in which the velocity difference between right and left movers is taken into account, whereas the fast one is attributed to Fabry-Perot interference. The energy ratios of these two modes from theory and experiment agreed within a factor of 3. The possibility of the realization of an AB interferometer remains for future work.

In order to achieve ultra-high-density electronic devices, spin-electronic transport using electronic spin as additional information has been an active research topic. Carbon nanotubes encapsulating ferromagnetic metal are a promising material to realize nanoscale spintronic devices. In Chapter III, Co-filled multi-walled carbon nanotubes were synthesized and their structure confirmed by XRD spectroscopy, EDS, and TEM images. As a catalyst, Co nanoclusters are also active sites for growing nanotubes. The elongation of the original Co catalyst or the insertion of Co nanoclusters during growth by capillary forces give a discontinuous filling of Co along the nanotube. For a Co-filled nanotube device, ~ 2% of the magnetoresistance switching upon a parallel magnetic field was reproducibly observed. Although a Co-filled nanotube device with switching behavior was demonstrated, the synthesis of better quality and smaller diameter tubes (well graphitized) with increased filling factor is needed for future device applications.

In Chapter IV, a transverse electric-field-induced conductance fluctuations in nanotubes, which were possibly explained by the modulation of the band structure of nanotubes due to subband mixing by the strong electric field. To reach such a high

electric field, we take advantage of large diameter multi-walled tubes beside close side gates. The period of conductance oscillations is of the same order of magnitude as the predicted period, but strong dependence on tube diameter is not found. Also, Fermi-level independence of the fluctuations still needs to be addressed. A perpendicular magnetic field produces positive magneto conductance at low fields and aperiodic fluctuations at higher fields, which are well described in terms of WL and UCF, respectively. Phase coherence lengths deduced from the fit with 1D WL theory are 30−40 nm comparable to the tube circumference. A high magnetic field was found to suppress transverse electric-field-induced conductance fluctuations, but the origin of this behavior is not yet known.

# REFERENCES


1. Heo, J. & Bockrath, M. Local Electronic Structure of Single-Walled Carbon Nanotubes from Electrostatic Force Microscopy. *Nano Lett.* **5**, 853-857 (2005).

2. Ashcroft, N.W. & Mermin, N.D. *Solid State Physics*. (Harcourt College, 1976).

3. Saito, R., Dresselhaus, G. & Dresselhaus, M.S. *Physical Properties of Carbon Nanotubes*. (Imperial College Press, 1998).

4. Minot, E.D. *Tuning The Band Structure of Carbon Nanotubes.* Cornell University (2004).

5. Heyd, R., Charlier, A. & McRae, E. Uniaxial-stress effects on the electronic properties of carbon nanotubes. *Physical Review B* **55**, 6820 (1997).

6. Yang, L., Anantram, M.P., Han, J. & Lu, J.P. Band-gap change of carbon nanotubes: Effect of small uniaxial and torsional strain. *Physical Review B* **60**, 13874 (1999).

7. Yang, L. & Han, J. Electronic Structure of Deformed Carbon Nanotubes. *Physical Review Letters* **85**, 154 (2000).

8. Kong, J., Soh, H.T., Cassell, A.M., Quate, C.F. & Dai, H. Synthesis of individual single-walled carbon nanotubes on patterned silicon wafers. *Nature* **395**, 878-881 (1998).

9. Brintlinger, T., et al. Rapid imaging of nanotubes on insulating substrates. *Applied Physics Letters* **81**, 2454-2456 (2002).

10. de Pablo, P.J., et al. Nonlinear Resistance versus Length in Single-Walled Carbon Nanotubes. *Physical Review Letters* **88**, 036804 (2002).

11. Yaish, Y., et al. Electrical Nanoprobing of Semiconducting Carbon Nanotubes Using an Atomic Force Microscope. *Physical Review Letters* **92**, 046401 (2004).

12. Baldacchini, C. & Cannistraro, S. Conductive atomic force microscopy investigation of transverse current across metallic and semiconducting single-walled carbon nanotubes. *Applied Physics Letters* **91**, 122103 (2007).

13. Bockrath, M., et al. Scanned Conductance Microscopy of Carbon Nanotubes and Lambda-DNA. *Nano Lett.* **2**, 187-190 (2002).

14. Bachtold, A., et al. Scanned Probe Microscopy of Electronic Transport in Carbon Nanotubes. *Physical Review Letters* **84**, 6082 (2000).

15. Pomorski, P., Pastewka, L., Roland, C., Guo, H. & Wang, J. Capacitance, induced charges, and bound states of biased carbon nanotube systems. *Physical Review B* **69**, 115418 (2004).

16. Piner, R.D., Zhu, J., Xu, F., Hong, S. & Mirkin, C.A. "Dip-Pen" Nanolithography. *Science* **283**, 661-663 (1999).

17. Xu, L., Lio, A., Hu, J., Ogletree, D.F. & Salmeron, M. Wetting and Capillary Phenomena of Water on Mica. *J. Phys. Chem. B* **102**, 540-548 (1998).

18. Zitzler, L., Herminghaus, S. & Mugele, F. Capillary forces in tapping mode atomic force microscopy. *Physical Review B* **66**, 155436 (2002).

19. Colchero, J., Storch, A., Luna, M., GomezHerrero, J. & Baro, A.M. Observation of Liquid Neck Formation with Scanning Force Microscopy Techniques. *Langmuir* **14**, 2230-2234 (1998).

20. Beaglehole, D. & Christenson, H.K. Vapor adsorption on mica and silicon: entropy effects, layering, and surface forces. *J. Phys. Chem.* **96**, 3395-3403 (1992).

21. Kane, C.L. & Mele, E.J. Size, Shape, and Low Energy Electronic Structure of Carbon Nanotubes. *Physical Review Letters* **78**, 1932 (1997).

22. Minot, E.D., et al. Tuning Carbon Nanotube Band Gaps with Strain. *Physical Review Letters* **90**, 156401 (2003).

23. Cao, J., Wang, Q. & Dai, H. Electromechanical Properties of Metallic, Quasimetallic, and Semiconducting Carbon Nanotubes under Stretching. *Physical Review Letters* **90**, 157601 (2003).

24. Bozovic, D., et al. Plastic deformations in mechanically strained single-walled carbon nanotubes. *Physical Review B* **67**, 033407 (2003).

25. Cronin, S.B., et al. Measuring the Uniaxial Strain of Individual Single-Wall Carbon Nanotubes: Resonance Raman Spectra of Atomic-Force-Microscope Modified Single-Wall Nanotubes. *Physical Review Letters* **93**, 167401 (2004).

26. Refael, G., Heo, J. & Bockrath, M. Sagnac Interference in Carbon Nanotube Loops. *Physical Review Letters* **98**, 246803 (2007).

27. Kim, W., et al. Synthesis of Ultralong and High Percentage of Semiconducting Single-walled Carbon Nanotubes. *Nano Lett.* **2**, 703-708 (2002).

28. Li, S., Yu, Z., Rutherglen, C. & Burke, P.J. Electrical Properties of 0.4 cm Long Single-Walled Carbon Nanotubes. *Nano Lett.* **4**, 2003-2007 (2004).

29. Huang, S., Woodson, M., Smalley, R. & Liu, J. Growth Mechanism of Oriented Long Single Walled Carbon Nanotubes Using "Fast-Heating" Chemical Vapor Deposition Process. *Nano Lett.* **4**, 1025-1028 (2004).

30. Fuhrer, M.S., et al. Crossed nanotube junctions. *Science* **288**, 494-497 (2000).

31. Yoon, Y.-G., Mazzoni, M.S.C., Choi, H.J., Ihm, J. & Louie, S.G. Structural Deformation and Intertube Conductance of Crossed Carbon Nanotube Junctions. *Physical Review Letters* **86**, 688 (2001).

32. Bockrath, M., et al. Resonant electron scattering by defects in single-walled carbon nanotubes. *Science* **291**, 283-285 (2001).

33. Goldsmith, B.R., et al. Conductance-Controlled Point Functionalization of Single-Walled Carbon Nanotubes. *Science* **315**, 77-81 (2007).

34. Kong, J., et al. Nanotube molecular wires as chemical sensors. *Science* **287**, 622-625 (2000).

35. Jespersen, T.S. & Nygard, J. Charge Trapping in Carbon Nanotube Loops Demonstrated by Electrostatic Force Microscopy. *Nano Lett.* **5**, 1838-1841 (2005).

36. Aharonov, Y. & Bohm, D. Significance of Electromagnetic Potentials in the Quantum Theory. *Physical Review* **115**, 485 (1959).

37. Liu, S. & Zhu, J. Carbon nanotubes filled with long continuous cobalt nanowires. *Applied Physics A: Materials Science & Processing* **70**, 673-675 (2000).

38. Wolf, S.A., et al. Spintronics: A spin-based electronics vision for the future. *Science* **294**, 1488-1495 (2001).

39. Thamankar, R., et al. Spin-polarized transport in magnetically assembled carbon nanotube spin valves. *Appl. Phys. Lett.* **89**, 033119 (2006).

40. Zutic, I. & Fuhrer, M. Spintronics-A path to spin logic. *Nature Physics* **1**, 85 (2005).

41. Sahoo, S., et al. Electric field control of spin transport. *Nature Physics* **1**, 99 (2005).

42. Tsukagoshi, K., Alphenaar, B.W. & Ago, H. Coherent transport of electron spin in a ferromagnetically contacted carbon nanotube. *Nature* **401**, 572-574 (1999).

43. Kang, Y.J., Choi, J., Moon, C.Y. & Chang, K.J. Electronic and magnetic properties of single-wall carbon nanotubes filled with iron atoms. *Phys. Rev. B* **71**, 115441 (2005).

44. Yang, C.K., Zhao, J. & Lu, J.P. Magnetism of transition-metal/carbon-nanotube hybrid structures. *Phys. Rev. Lett* **90**, 257203 (2003).

45. Liu, S., Zhu, J., Mastai, Y., Felner, I. & Gedanken, A. Preparation and Characteristics of Carbon Nanotubes Filled with Cobalt. *Chem. Mater.* **12**, 2205-2211 (2000).

46. Ma, Y.C., Li X., Lun N., Wen, S. Growth and Characterization of Cobalt-filled Carbon Nanotubes Prepared by a Simple Catalytic Method. *Mat. Res. Soc. Sypm. Proc.* **776**, Q8.17.1 (2003).

47. Buffat, P. & Borel, J.P. Size effect on the melting temperature of gold particles. *Physical Review A* **13**, 2287 (1976).

48. Jiang, Q., Aya, N. & Shi, F.G. Nanotube size-dependent melting of single crystals in carbon nanotubes. *Applied Physics A: Materials Science & Processing* **64**, 627-629 (1997).

49. Ebbesen, T.W. Carbon Nanotubes. *Annual Review of Materials Science* **24**, 235-264 (1994).

50. Bilaniuk, M. & Howe, J.M. Wetting, Bonding and Interfacial Energy of Nanocrystalline Metal Particles on Crystalline DCH Polymer and Amorphous Carbon Substrates. *Interface Science* **6**, 319-345 (1998).

51. M. S. Wang, J.Y.W., Q. Chen, L.-M. Peng Fabrication and Electrical and Mechanical Properties of Carbon Nanotube Interconnections. *Advanced Functional Materials* **15**, 1825-1831 (2005).

52. Collins, P.G., Arnold, M.S. & Avouris, P. Engineering carbon nanotubes and nanotube circuits using electrical breakdown. *Science* **292**, 706-709 (2001).

53. Chiu, H.Y., et al. Ballistic Phonon Thermal Transport in Multiwalled Carbon Nanotubes. *Phys. Rev. Lett* **95**, 226101 (2005).

54. Leven, B. & Dumpich, G. Resistance behavior and magnetization reversal analysis of individual Co nanowires. *Physical Review B (Condensed Matter and Materials Physics)* **71**, 064411 (2005).

55. Dumpich, G., Krome, T.P. & Hausmanns, B. Magnetoresistance of single Co nanowires. *Journal of Magnetism and Magnetic Materials* **248**, 241-247 (2002).

56. Novikov, D.S. & Levitov, L.S. Electron properties of Carbon nanotubes in the field effect regime. *cond-mat/0204499v1* (2002).

57. Li, Y., Rotkin, S.V. & Ravaioli, U. Electronic Response and Bandstructure Modulation of Carbon Nanotubes in a Transverse Electrical Field. *Nano Lett.* **3**, 183-187 (2003).

58. Ajiki, H. & Ando, T. Electronic states of carbon nanotubes. *Journal of the Physical Society of Japan* **62**, 1255-1266 (1993).

59. Schönenberger, C., Bachtold, A., Strunk, C., Salvetat, J.P. & Forró, L. Interference and Interaction in multi-wall carbon nanotubes. *Applied Physics A: Materials Science & Processing* **69**, 283-295 (1999).

60. Bachtold, A., et al. Aharonov-Bohm oscillations in carbon nanotubes. *Nature* **397**, 673-675 (1999).

61. Langer, L., et al. Quantum transport in a multiwalled carbon nanotube. *Phys. Rev. Lett.* **76**, 479-482 (1996).

62. Altshuler, B.L., Aronov, A.G. & Khmelnitsky, D.E. Effects of electron-electron collisions with small energy transfers on quantum localisation. *Journal of Physics C: Solid State Physics* **15**, 7367-7386 (1982).

63. Al'tshuler, B.L. *Pis'ma Zh. Eksp. Teor. Fiz* **41**, 530 (1985).

64. Stone, A.D. & Lee, P.A. Effect of Inelastic Processes on Resonant Tunneling in One Dimension. *Physical Review Letters* **54**, 1196 (1985).

65. Beenakker, C.W.J. & van Houten, H. Flux-cancellation effect on narrow-channel magnetoresistance fluctuations. *Physical Review B* **37**, 6544 (1988).